Scholars' Mine

Fall 2019

Development and demonstration of sampling techniques for a Chirped Pulse Fourier Transform Microwave Spectrometer

Frank Edward Marshall

Recommended Citation

DEVELOPMENT AND DEMONSTRATION OF SAMPLING TECHNIQUES FOR A

CHIRPED PULSE FOURIER TRANSFORM MICROWAVE SPECTROMETER

by

FRANK EDWARD MARSHALL

A DISSERTATION

Presented to the Faculty of the Graduate School of the

MISSOURI UNIVERSITY OF SCIENCE AND TECHNOLOGY

In Partial Fulfillment of the Requirements for the Degree

DOCTOR OF PHILOSOPHY

in

CHEMISTRY

2019

Approved by:

Garry S. Grubbs II, Advisor
Richard Dawes
Phillip Whitefield
Jeffrey Winiarz
Kristen Donnell

PUBLICATION DISSERTATION OPTION

This dissertation consists of the following six articles, formatted in the style used by the Missouri University of Science and Technology:

Paper I: Pages 39-60 have been published by Molecular Physics.

Paper II: Pages 61-90 have been published by the Journal of Molecular Spectroscopy.

Paper III: Pages 91-104 have been published by the Journal of Molecular Spectroscopy.

Paper IV: Pages 105-118 are still in progress and are intended for submission

Paper V: Pages 119-139 have been published by the Journal of Molecular Spectroscopy.

Paper VI: Pages 140-156 have been published by the Journal of Molecular Spectroscopy.

ABSTRACT

With the introduction of the Chirped Pulse-Fourier Transform Microwave Spectrometer in the past decade, it has become possible to rapidly study the rotational spectra of molecules in the gas phase. It is possible to study molecules that are not normally in the gas phase through the use of various sourcing techniques. The development of both the heated nozzle and the laser ablation sourcing techniques allow for the study of liquids and solids, respectively. The design and performance of these sources will be presented in detail and discussed. Additionally, the development of a Multi-Antennae detection scheme, useful in improving overall sensitivity of the spectrometer, will be presented and discussed

ACKNOWLEDGMENTS

TABLE OF CONTENTS

LIST OF ILLUSTRATIONS

PAPER VI

LIST OF TABLES

1. INTRODUCTION

1.1. INTRODUCTION TO MICROWAVE SPECTROSCOPY

Rotational spectroscopy is a well-established gas-phase spectroscopic technique that is useful for structural determination of molecules. It involves the transition from one rotational quanta to another through the interaction of an electromagnetic wave with the permanent electric dipole moment of a molecule. This technique is powerful in that it allows for the determination of molecular structure, such as bond angles and bond lengths, as well as electronic state information, Stark and Zeeman effects, and hyperfine structure all through a single experiment.

The first Rotational Spectroscopy experiment was carried out by Cleeton and Williams[1] in 1934 when they measured the absorption of electromagnetic radiation from by Ammonia gas. This experiment required the development of new technology – magnetron oscillators – to produce the necessary light in the 1-4 cm wavelength (about 7.5-30 GHz) range. Because of the technological barrier to experimentation, this remained the only experiment of this type until 1946 when microwave technology developed for World War II became commonly available.

Because the frequency of light required to excite a rotational transition typically falls in the microwave regime of the electromagnetic spectrum, this type of spectroscopy is typically called "Microwave spectroscopy". The microwave regime is typically defined as the region of the electromagnetic spectrum between 1-300 GHz, however these are not well defined limits. Typical microwave experiments occur somewhere around 2-30 GHz.

Microwave spectroscopy requires that molecules be in the gas phase. This, by default, biases the technique towards lighter molecules. Lighter molecules tend to be a gas at room temperature. Larger molecules, which are typically liquids or solids, are possible to study if special care is taken. In order to study a liquid, it is possible to use vapor from a liquid to perform a microwave experiment, which typically requires an interfacing of a carrier gas and a liquid. Sometimes a heater is required to increase a molecules vapor pressure, which increases a liquids vapor yield. Solids are more difficult yet to study, but it is still possible. Studying a solid requires some form of ionization source or laser source that will transform the sample from a liquid or solid. Various techniques for achieving this will be discussed later in this document.

A typical microwave spectroscopy experiment involves a vacuum chamber, a nozzle, a light source, and a detector. Gas phase molecules are typically injected into the vacuum chamber via a nozzle and allowed to expand. Light is then passed through the gas cloud where rotational states are excited. When the light is turned off, the molecules decay from their excited rotational state through a process called the Free Induction Decay (FID). The FID is then detected by a detector and analyzed. Again, this process will be explored in greater detail later in this document.

1.2. INTRODUCTORY THEORY

It is useful when deriving the theory behind rotational spectroscopy to start with a simple assumption: the rotating body is rigid. This is called the rigid rotator. By assuming the body is rigid, it will assume that the bonds between atoms have no distortion in length or angle.

$$\vec{L} = I\vec{w} \tag{1}$$

Where $\vec{L}$ is the angular momentum vector, $\mathbf{I}$ is the moment of inertia, and $\vec{w}$ is the

angular velocity vector. In three dimensions it is possible to represent equation (1) in

tensor form.

$$\begin{pmatrix} L_x \\ L_y \\ L_z \end{pmatrix} = \begin{pmatrix} I_{xx} & I_{xy} & I_{xz} \\ I_{yx} & I_{yy} & I_{yz} \\ I_{zx} & I_{zy} & I_{zz} \end{pmatrix} \begin{pmatrix} w_x \\ w_y \\ w_z \end{pmatrix} \tag{2}$$

Where I is now a 3x3 matrix called the moment of inertia tensor. This matrix is a

mathematical description for the distribution of mass throughout an object, which in the

case of microwave spectroscopy would be the distribution of mass throughout a

molecule. The individual components of this tensor, which are the moments of inertia for

each axis and the cross terms between axes, can be defined as follows.

$$I_{xx} = \sum_\alpha m_a(y_a^2 + z_a^2) = \sum_\alpha m_a r_x^2 \tag{3}$$

$$I_{yy} = \sum_\alpha m_a(x_a^2 + z_a^2) = \sum_\alpha m_a r_y^2$$

$$I_{zz} = \sum_\alpha m_a(x_a^2 + y_a^2) = \sum_\alpha m_a r_z^2$$

$$I_{xy} = I_{yx} = -\sum_\alpha m_a x_a y_a$$

$$I_{xz} = I_{zx} - \sum_\alpha m_a x_a z_a$$

$$I_{yz} = I_{zy} = -\sum_\alpha m_a y_a z_a$$

Where r_i defines the radial distance from the center of mass, C, which can be defined as

$$C = \sum_a m_a r_a \tag{4}$$

The previous equations mathematically describe how a body will rotate. The moment of inertia mathematically represents the body, while the angular velocity describes how fast and what direction the body will rotate about its center of mass.

It is possible to simplify these expressions by recognizing that the moment of inertia tensor, found in equation (3), is a symmetric matrix. This means it is possible to apply a coordinate transformation matrix, **X**, and it it's inverse matrix, **X⁻¹**, to achieve a new matrix **I'** where the off diagonal components (I_{xy}, I_{xz}, etc..) vanish. This is represented in equation (5).

$$\mathbf{IX = XI} \tag{5}$$

$$\mathbf{X^{-1}IX = I'} = \begin{pmatrix} I_{x'x'} & 0 & 0 \\ 0 & I_{y'y'} & 0 \\ 0 & 0 & I_{z'z'} \end{pmatrix}$$

Applying this coordinate transformation requires that a specific coordinate system is applied. This new system, called the principal axis system (PAS), will be assumed from this point forward. The PAS orients the axis system so that the new X axis will maximize $I_{z'z'}$. The Y axis is chosen to make $I_{y'y'}$ the 2nd largest moment of inertia, and the Z axis so that $I_{x'x'}$ is the smallest moment. Additionally, it is useful to rename the axes so that the X axis is now the c axis, the Y axis the b axis, and the Z axis as the a axis. The reason for this convention will become more apparent in later sections. The new form of **I'** obtained in equation (5) can be seen below in equation (6).

$$\mathbf{I'} = \begin{pmatrix} I_a & 0 & 0 \\ 0 & I_b & 0 \\ 0 & 0 & I_c \end{pmatrix} \tag{6}$$

Rewriting equation (2) using equation (6) and the PAS yields

$$\begin{pmatrix} L_a \\ L_b \\ L_c \end{pmatrix} = \begin{pmatrix} I_a & 0 & 0 \\ 0 & I_b & 0 \\ 0 & 0 & I_c \end{pmatrix} \begin{pmatrix} w_a \\ w_b \\ w_c \end{pmatrix} \tag{7}$$

From here, it is possible to obtain the following equations for angular momentum

$$L_a = I_a w_a \tag{8}$$

$$L_b = I_b w_b$$

$$L_c = I_c w_c$$

The kinetic energy, E_k, of a rigid rotor is classically defined as

$$E_k = \frac{1}{2}\mathbf{I}\mathbf{w}^2 \tag{9}$$

Manipulating equation (9) makes it possible to define E_k in terms of angular momentum

$$E_k = \frac{1}{2}\mathbf{I}\mathbf{w}^2 = \frac{1}{2}\mathbf{w}^t\mathbf{I}\mathbf{w} \tag{10}$$

$$= \frac{1}{2}(w_a w_b w_c) \begin{pmatrix} I_a w_a \\ I_b w_b \\ I_c w_c \end{pmatrix}$$

$$= \frac{1}{2}I_a w_a^2 + \frac{1}{2}I_b w_b^2 + \frac{1}{2}I_c w_c^2$$

$$= \frac{L_a^2}{2I_a} + \frac{L_b^2}{2I_b} + \frac{L_c^2}{2I_c} \text{ as } L_i^2 = I_i^2 w_i^2$$

From here it is useful to replace L, the symbol for angular momentum, with J, the symbol for total angular momentum.

$$E_k = \frac{J_a^2}{2I_a} + \frac{J_b^2}{2I_b} + \frac{J_c^2}{2I_c} = \frac{\vec{J}^2}{2I} \tag{11}$$

The result of equation (11) is the Hamiltonian operator for the free space rigid rotor linear molecule. If this is used in the Schrödinger equation this will yield the equation for the energy levels of a linear rigid rotor in free space.

$$\hat{H}\Psi = E\Psi \tag{12}$$

$$\frac{\hat{J}^2}{2I}\Psi = E\Psi$$

$$\frac{\hat{J}^2}{2I}\Psi = \frac{J(J+1)\hbar^2}{2I}\Psi = BJ(J+1)\Psi$$

Thus, the energy eigenvalue that describes the energy levels of a rigid rotator can be described as *F(J)* and the spectroscopic rotational constant as B.

$$F(J) = BJ(J+1), B = \frac{\hbar^2}{2I} = \frac{h^2}{8\pi^2 I} \tag{13}$$

In the above equation, B is expressed in units of Joules, however it is more useful to express this constant in terms of Hz. This yields equation (14) below

$$F(J) = hBJ(J+1), B = \frac{h}{8\pi^2 I} \tag{14}$$

Later the B rotational constant will be expressed as $B = \frac{h}{8\pi^2 I_b}$. This is useful for when more than just the B moments of inertia are considered.

1.3. SELECTION RULES

Equation (14) begins to calculate the rotational energy levels, but it cannot predict which rotational quanta will be excited from a given rotational state. From [2], the transitions will occur from rotational state *J'* to state *J''* according to

$$v_{J' \leftarrow J''} = F(J') - F(J'') \tag{15}$$

$$= BJ'(J' + 1) - BJ''(J'' + 1)$$

According to [3], this equation must yield the same results as a previously derived

equation $v = \frac{Jh}{4\pi^2 I}$, which can only be true when J' = J'' + 1. Substitution this into

equation (15)

$$v_{J' \leftarrow J''} = B(J'' + 1)(J'' + 2) - BJ''(J'' + 1) = 2BJ''(J'' + 1) \tag{16}$$

This yields two results. The first result is that the selection rules for a rotational

transition are $\Delta J = \pm 1$. The second result is that the rotational transitions are separated by

2B. It is possible to observe rotational transitions with $\Delta J = \pm 2, \pm 3$, etc… which are

called dipole forbidden transitions. These transitions, which are typically significantly

weaker in intensity, are made possible due to a molecules electric quadrupole moment.

1.4. SYMMETRIC TOPS

Previously, to derive equation (14), it was assumed that the molecule be a linear

rigid rotor. To obtain the energy levels for a non-linear molecule, which is often the case,

it is necessary to expand the approach to include symmetry. There are generally two

types of symmetry for molecules: symmetric tops and asymmetric tops. Symmetric tops

include prolate molecules, which are defined as $I_a < I_b = I_c$, and oblate molecules, which

are defined as $I_a = I_b < I_c$. Starting with the prolate symmetric top case and inserting this

into equation (11)

$$E_k = \frac{J_a^2}{2I_a} + \frac{J_b^2}{2I_b} + \frac{J_c^2}{2I_c} = \frac{J_a^2}{2I_a} + \frac{1}{2I_b}(J_b^2 + J_c^2) \text{ as } I_b = I_c \tag{17}$$

Similarly, for an oblate top

$$E_k = \frac{J_a^2}{2I_a} + \frac{J_b^2}{2I_b} + \frac{J_c^2}{2I_c} = \frac{1}{2I_b}(J_a^2 + J_b^2) + \frac{J_c^2}{2I_c} \text{ as } I_a = I_b \tag{18}$$

Using the relation $J^2 = J_a^2 + J_b^2 + J_c^2$ and rewriting it as $J^2 - J_a^2 = J_b^2 + J_c^2$ changes the form of equation (17) to

$$E_k = \frac{J_a^2}{2I_a} + \frac{1}{2I_b}(J_b^2 + J_c^2) = \frac{J_a^2}{2I_a} + \frac{1}{2I_b}(J^2 - J_a^2) = \frac{J_a^2}{2I_a} + \frac{J^2}{2I_b} - \frac{J_a^2}{2I_b} \tag{19}$$

$$E_k = \frac{J^2}{2I_b} + \left(\frac{1}{2I_a} - \frac{1}{2I_b}\right)J_a^2$$

The Hamiltonian for this case can be written as

$$\hat{H} = \frac{\hat{J}^2}{2I_b} + \left(\frac{1}{2I_a} - \frac{1}{2I_b}\right)\hat{J}_a^2 \tag{20}$$

A similar approach can be used for the case of the oblate symmetric top and equation (18).

In order to solve the Schrödinger equation (12) to derive the energy levels for a prolate symmetric top, it is necessary to introduce some helpful mathematics. It is first useful to describe the molecule in two reference frames: the molecular frame and the laboratory frame. The Laboratory frame is standard Cartesian coordinates – x, y, z – while the molecular frame uses coordinates x, y, z. Rotation of the molecule, and therefore the P.A.S., relative to the laboratory frame can be described using the Euler angles shown in Figure 1.1.

Using Figure 1.1 it is possible to derive a transformation matrix, S, such that

$$\begin{pmatrix} x \\ y \\ z \end{pmatrix} = S \begin{pmatrix} X \\ Y \\ Z \end{pmatrix} = \begin{pmatrix} \phi_{xX} & \phi_{xY} & \phi_{xZ} \\ \phi_{yX} & \phi_{yY} & \phi_{yZ} \\ \phi_{zX} & \phi_{zY} & \phi_{zZ} \end{pmatrix} \begin{pmatrix} X \\ Y \\ Z \end{pmatrix} \tag{21}$$

S is derived by rotating X and Y by angle ϕ about Z into X' and Y', then rotating X' and Z by angle θ about Y' into X" and z, and finally rotating X" and Y' by angle χ about z into x and y. In mathematical terms this involves 3 separate rotation matrices multiplied together, as seen below.
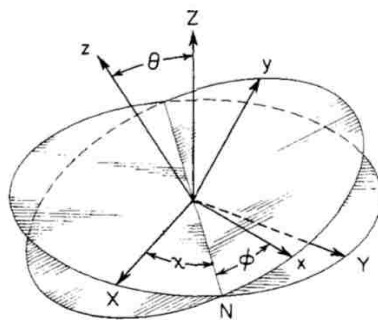
Figure 1.1. The Euler angles θ, ϕ, χ that relate the Laboratory Frame (X, Y, Z) with the P.A.S. (a, b, c).[4]

$$S = \begin{pmatrix} \cos\chi & \sin\chi & 0 \\ -\sin\chi & \cos\chi & 0 \\ 0 & 0 & 1 \end{pmatrix} \begin{pmatrix} \cos\theta & 0 & -\sin\theta \\ 0 & 1 & 0 \\ \sin\theta & 0 & \cos\theta \end{pmatrix} \begin{pmatrix} \cos\phi & \sin\phi & 0 \\ -\sin\phi & \cos\phi & 0 \\ 0 & 0 & 1 \end{pmatrix} \tag{22}$$

$$S = \begin{pmatrix} \cos\theta\cos\phi\cos\chi - \sin\phi\sin\chi & \cos\theta\sin\phi\cos\chi - \cos\phi\sin\chi & -\sin\theta\cos\chi \\ -\cos\theta\cos\phi\sin\chi - \sin\phi\cos\chi & -\cos\theta\sin\phi\sin\chi - \cos\phi\cos\chi & \sin\theta\sin\chi \\ \sin\theta\cos\phi & \sin\theta\sin\phi & \cos\theta \end{pmatrix}$$

The angular momenta of the system can be measured either in the laboratory frame $(\hat{J}_X, \hat{J}_Y, \hat{J}_Z)$ or in the molecular frame $(\hat{J}_x, \hat{J}_y, \hat{J}_z)$. The relation can be expressed through the form of equation (21).

$$\begin{pmatrix} \hat{J}_x \\ \hat{J}_y \\ \hat{J}_z \end{pmatrix} = \begin{pmatrix} \phi_{xX} & \phi_{xY} & \phi_{xZ} \\ \phi_{yX} & \phi_{yY} & \phi_{yZ} \\ \phi_{zX} & \phi_{zY} & \phi_{zZ} \end{pmatrix} \begin{pmatrix} \hat{J}_X \\ \hat{J}_Y \\ \hat{J}_Z \end{pmatrix} \tag{23}$$

After relating the components of ϕ_{ij} to the matrix S and deconvoluting the equations for $\hat{J}_i$

yields equations (24)

$$\hat{J}_x = -i\hbar\left(-\frac{\cos\chi}{\sin\theta}\frac{d}{d\phi} + \frac{\cos\phi}{\sin\theta}\frac{d}{d\chi} - \sin\phi\frac{d}{d\theta}\right) \tag{24}$$

$$\hat{J}_y = -i\hbar\left(\frac{\sin\chi}{\sin\theta}\frac{d}{d\phi} + \frac{\sin\chi\cos\theta}{\sin\theta}\frac{d}{d\chi} + \cos\chi\frac{d}{d\theta}\right)$$

$$\hat{J}_z = -i\hbar\frac{d}{d\chi}$$

$$\hat{J}_Z = -i\hbar\frac{d}{d\phi}$$

It should be noted that the individual components the angular momentum do not

commute. For example, $\left[\hat{J}_x,\hat{J}_y\right] = -i\hbar\hat{J}_z \neq 0$, which means these values cannot be

observed simultaneously and the order of measurement matters. Conversely $\left[\hat{J}^2,\hat{J}_z\right] =$

$\left[\hat{J}^2,\hat{J}_Z\right] = 0$, meaning these values commute are eigenvalues for each operator may be

simultaneously collected. For this reason it will be primarily these operators that decide

which eigenvalues are obtained from a rotational spectra.

Rewriting the Schrödinger equation in a more useful form yields

$$\hat{H}|JKM\rangle = E|JKM\rangle \tag{25}$$

Additionally, the eigenvalues for $\hat{J}^2,\hat{J}_z$, and $\hat{J}_Z$ take the form

$$\hat{J}^2|JKM\rangle = J(J+1)\hbar^2|JKM\rangle \tag{26}$$

$$\hat{J}_Z|JKM\rangle = M_j\hbar|JKM\rangle$$

$$\hat{J}_z|JKM\rangle = K\hbar|JKM\rangle$$

where J is the total angular momentum quantum number, K is the quantum number

defined as the projection of $\hat{J}$ along the molecular z-axis, and M_j is the magnetic quantum

number

Inserting the Hamiltonian for the prolate symmetric top into equation (25) gives

the form

$$\hat{H}|JKM\rangle = \left(\frac{\hat{J}^2}{2I_B} + \left(\frac{1}{2I_A} - \frac{1}{2I_B}\right)\hat{J}_a^2\right)|JKM\rangle = \frac{\hat{J}^2}{2I_B}|JKM\rangle + \left(\frac{1}{2I_A} - \frac{1}{2I_B}\right)\hat{J}_a^2|JKM\rangle \quad (27)$$

$$\hat{H}|JKM\rangle = \frac{\hbar^2}{2I_B}J(J+1)|JKM\rangle + \left(\frac{1}{2I_A} - \frac{1}{2I_B}\right)K^2\hbar^2|JKM\rangle, \hat{J}_a = \hat{J}_z$$

$$\hat{H}|JKM\rangle = \left(\frac{\hbar^2}{2I_B}J(J+1) + \left(\frac{1}{2I_A} - \frac{1}{2I_B}\right)K^2\hbar^2\right)|JKM\rangle$$

Using the results from equation (27) and equation (25), the energy for a prolate

symmetric top can be given by

$$E_{JK_a} = BJ(J+1) + (A-B)K_a^2 \quad (28)$$

For an oblate top the same process can be followed to derive the energy levels given by

equation (29)

$$E_{JK_c} = BJ(J+1) + (C-B)K_c^2 \quad (29)$$

Similar to the case of the linear rigid rotor molecule, the rotational constants A, B,

and C can be defined as follows

$$A = \frac{h^2}{8\pi^2 I_A}, B = \frac{h^2}{8\pi^2 I_B}, C = \frac{h^2}{8\pi^2 I_C} \quad (30)$$

To determine the selection rules, a similar process is followed to that in section

1.3. The results, according to [1], are that $\Delta J = \pm 1, \Delta M = 0, \pm 1$, and $\Delta K = 0$.

An asymmetric to, which is defined such that $I_A \leq I_B \leq I_C$, has no analytical

solution and must be solved numerically under the Schrödinger equation. There are

approximations that can be made based on how asymmetric a molecule is, however. The

energy levels of an asymmetric top will tend towards those of the prolate top if the

asymmetric molecule is shaped roughly like a prolate top, or vice versa for an oblate top.

To measure the degree of asymmetry of a molecule, it is useful to employ Ray's

asymmetry parameter, k, which is defined as follows

$$k = \frac{2B - A - C}{A - C} \tag{31}$$

With Ray's asymmetry parameter, as $B \to C$, as is the case for a prolate top, then

$k = \frac{C - A}{A - C} = -1$ while as $B \to A$ for an oblate top then $k = 1$. The closer k is to -1, the

closer the molecule is to being a prolate top. Conversely, the closer k is to 1, the closer

the molecule is to being an oblate top.

It is possible to obtain the energy levels of an asymmetric top for certain values of

J. Returning to equation (11) yields the Hamiltonian for a rigid rotor, seen in equation

(32) below

$$\hat{H} = \frac{\hat{J}_a^2}{2I_a} + \frac{\hat{J}_b^2}{2I_b} + \frac{\hat{J}_c^2}{2I_c} \tag{32}$$

Multiplying (32) by $\hbar^2$ yields the following

$$\hbar^2 \hat{H} = \hbar^2 \frac{\hat{J}_a^2}{2I_a} + \hbar^2 \frac{\hat{J}_b^2}{2I_b} + \hbar^2 \frac{\hat{J}_c^2}{2I_c} = A\hat{J}_a^2 + B\hat{J}_b^2 + C\hat{J}_c^2 \tag{33}$$

$$= \frac{A + B}{2}\left(\hat{J}_a^2 + \hat{J}_b^2\right) + C\hat{J}_c^2 + \frac{A - B}{2}\left(\hat{J}_a^2 - \hat{J}_b^2\right)$$

$$= \frac{A + B}{2}\hat{J}^2 + \left(C - \frac{A + B}{2}\right)\hat{J}_c^2 + \frac{A - B}{4}\left(\left(\hat{J}^+\right)^2 + \left(\hat{J}^-\right)^2\right)$$

where $\hat{J}^+$ and $\hat{J}^-$ are defined as the raising and lowering operators. These operators have

the eigenvalues of

$$\langle JK|\hat{J}^2|JK\rangle = \hbar^2 J(J + 1) \tag{34}$$

$$\langle JK|\hat{J}_C^2|JK\rangle = \hbar^2 K^2$$

$$\langle JK+2|\left(\hat{J}^-\right)^2|JK\rangle = \hbar^2\big((J-K)(J+K+1)(J-K-1)(J+K+2)\big)^{\frac{1}{2}}$$

$$\langle JK-2|\left(\hat{J}^+\right)^2|JK\rangle = \hbar^2\big((J+K)(J-K+1)(J+K-1)(J-K+2)\big)^{\frac{1}{2}}$$

For J=1 the values of K=-1, 0, and 1. Applying the Hamiltonian in (33) to states |1,-1>, |1,0>, |1,1> yields the following matrix

$$
\begin{array}{cccc}
 & |1,1\rangle & |1,-1\rangle & |1,0\rangle \\
\begin{array}{c}\langle 1,1| \\ \langle 1,-1| \\ \langle 1,0|\end{array} &
\left(\begin{array}{ccc}
C+\frac{A+B}{2} & \frac{A-B}{2} & 0 \\
\frac{A-B}{2} & C+\frac{A+B}{2} & 0 \\
0 & 0 & A+B
\end{array}\right)
\end{array}
\tag{35}
$$

One of the eigenvalues for this matrix is already determined, which is $A+B$. To find the other values it is necessary to find the determinant of the 2x2 block in the top left corner of the matrix.

$$\begin{vmatrix} C+\frac{A+B}{2}-\lambda & \frac{A-B}{2} \\ \frac{A-B}{2} & C+\frac{A+B}{2}-\lambda \end{vmatrix} = \left(C+\frac{A+B}{2}-\lambda\right)^2 - \left(\frac{A-B}{2}\right)^2 = 0 \tag{36}$$

$$\lambda = C+A, C+B$$

This solution gives 3 eigenvalues total: A+B, C+A, C+B. From equations (28) and (29) it can be shown that the energy levels of the prolate top are higher than the oblate top as $(A-B)>0$ while $(C-B)<0$ by definition as $A \geq B \geq C$. This means that for each J, the energy levels of K_a increase in energy as K_a increases for a prolate top, while for an oblate top the K_c energy levels decrease in energy as K_c increases in value. For an asymmetric top it is useful to introduce the quantum number $J_{K_a K_c}$ to label the energy levels to describe the prolate-oblate distortion correlation. This allows for labeling the energy levels, $E(J_{K_a K_c})$, of the $J=1$ state calculated above to be written as $E(1_{10}) = A+B$,

$E(1_{11}) = A+C$, $E(1_{01}) = B+C$. This same process may be repeated for values of J = 2, 3, etc… however the matrix size rapidly grows to the point of being extremely difficult to analytically determine.

With the introduction of $J_{K_aK_c}$ it is now possible to consider rotational transitions about a specific dipole moment. As asymmetric tops are, by definition, different between each axis, then it follows that each axis will have its own dipole moment. These corresponding dipoles may be written as μ_a, μ_b, μ_c. If $\mu_a \neq 0$ then it is possible to observe an a-type transition when $\Delta K_a = 0, \pm 2, \pm 4, ...$ and $\Delta K_c = \pm 1, \pm 3, \pm 5, ...$, or when K_c changes in parity and K_a does not. Conversely, if $\mu_c \neq 0$ then a c-type transition will occur when K_a changes parity and K_c does not. The final transition type, the b-type transition, occurs if $\mu_b \neq 0$ and both K_a and K_c change parity.

The selection rules for an asymmetric top are difficult to calculate as they require taking into account the three unique dipole moments. According to [1], the selection rules are given as $\Delta J = 0, \pm 1$ and $\Delta M = 0, \pm 1$.

1.5. CENTRIFUGAL DISTORTION

So far the rigid rotor approximation has yielded equations for the energy levels and frequencies for linear, symmetric, and asymmetric molecules. Molecules, however, are not strictly rigid. When the molecule rotates it will experience a force due to the rotation. This force, known as a centrifugal force, is known as a "pseudo-force" as it only exists within the rotating reference frame of the molecule. This force manifests itself on the individual atoms by trying to pull the atoms outward from the center of mass of the molecule, causing the bonds to stretch. This stretching can be modeled as if it were a

spring through the use of Hooke's law. Starting from a linear diatomic molecule and building to an asymmetric topThe equations for the centrifugal force, F_c, and hooks law, F_r, according to [2] can be found below

$$F_c = \frac{J^2}{\mu r^3}, F_r = k(r_e - r_c) \tag{37}$$

where μ is the reduced mass defined such that $= \frac{m_1 m_2}{m_1 + m_2}$, r_e is the internuclear distance at equilibrium, and r_c is the internuclear distance under the influence of the centrifugal force. Balancing the force equation so that they must equal each other will ultimately yield the following equation for the energy levels.

$$F(J) = BJ(J+1) - D_j\big(J(J+1)\big)^2 \tag{38}$$

where D_j is the centrifugal distortion constant defined as $D = \frac{4B_e^3}{w_e^2}$ where w_e^2 is the equilibrium vibrational frequency and B_e is the effective rotational constant B, defined as $B_e = B - D_j J(J+1)$. This is necessary as the distortion of the bonds often causes elongation of the bonds which will alter the rotational constants.

For symmetric tops it is possible to write a similar equation to (38) for the energy levels accounting for centrifugal distortion. This equation can be found below

$$F(J,K) = BJ(J+1) - D_j\big(J(J+1)\big)^2 + (A-B)K^2 - D_k K^4 - D_{jk}J(J+1)K^2 \tag{39}$$

where D_j, D_{jk}, and D_k are all first order centrifugal distortion constants.

1.6. STRUCTURE DETERMINATION

Through the use of rotational spectroscopy it is possible to determine the molecular structure, including bond lengths and bond angles. This is possible only if the isotopologues of a molecule are detected. This can be done either through detection of an

isotopologue in natural abundance or by using an enriched sample designed at targeting a specific isotope at a specific location in the molecule. Once the rotational constants for an isotopologue have been obtained, then it is possible by a method put forth by Kraitchman [5] to determine the position coordinates for each substituted atom.

The Kraitchman Substitution analysis works by measuring the changes in mass due to isotopic substitution. Rotational spectroscopy measures the rotational constants of a molecule, which are inversely proportional to the moment of inertia, which are proportional to the mass distribution along an axis. The moment of inertia tensor, which is defined in equation (2), is defined by the coordinates of an atom as well as the mass of the atom. This tensor is then effected by these changes in mass from the isotopic substitution. Correlating the changes in these moments of inertia with the location of the substituted isotope in the molecule can yield an exact – to within experimental uncertainty – coordinate system for the molecule. To determine bond lengths this is a matter of then using the three dimensional Pythagorean Theorem to determine bond lengths between atoms. When all the bond lengths are known it requires basic trigonometry to determine the angles between bonds.

2. INSTRUMENTATION THEORY, BACKGROUND, AND TECHNIQUES

2.1. INSTRUMENTATION BACKGROUND

As previously mentioned, the first Microwave Spectroscopy experiment was technically carried out in 1934 by Cleeton [1]. This unique experiment utilized a magnetostatic oscillator as a microwave source, two brass mirrors 3 feet in diameter, an echellete grating, and a pyrite-phosphor-bronze crystal detector. This experiment used a gas cell containing pure ammonia at atmospheric pressure. No other microwave spectroscopy experiments were carried out until post-WWII when Radar technologies developed for the war become commonly available. This type of experiment remains relatively unique to microwave spectroscopy this day.

Post WWII instrumentation was primarily waveguide based. The common method would be to measure the waveguide field strength at multiple frequencies without any sample, introduce sample, and measure the difference. The sample, which would be introduced directly into the waveguide, would absorb the electromagnetic radiation. There were multiple issues with these experiments, however. The waveguides typically had a short path length, which would limit sensitivity of the experiment according to Beer's law. To remedy this it was necessary to run lengths of waveguide around a laboratory. This was, of course, large and expensive, but such large systems were also prone to leaks that would affect the spectra. Additionally, these experiments were typically carried out under high temperature and pressure. The higher temperature would excite multiple rotational states, which would often times require a higher frequency experiment that is harder to decipher due to J dependence of certain terms. At higher J

levels certain things, such as hyperfine splitting, become more pronounced and make the spectra harder to interpret. It would also be possible for a higher temperature experiment to excite a vibrational state that could make the spectra more difficult to interpret. Finally, due to the higher gas pressure inherent with this technique, collision broadening was a common issue that would lead to broader spectral lines that would ultimately decrease resolution.

In 1980 T. J. Balle and W. H. Flygare introduced a Fabry-Perot cavity based microwave spectrometer [6]. This spectrometer led to an increase in both sensitivity and resolution over the previous waveguide based techniques. It utilizes two metallic (conductive) mirrors to create a standing electromagnetic wave, a vacuum, and a supersonic pulse nozzle to introduce and rotationally cool the molecules. The standing wave increases available power, meaning the spectrometer is capable of exciting more rotational transitions. Additionally, the standing wave essentially increases the pathlength as the light passes through the sample on the order of 10,000-20,000 times, making this a very sensitive instrument. The supersonic pulse nozzle does two things: it rotationally cools the molecules to the ground state and it makes the gas collision free. The lack of collision broadening – and other effects that will be explained later – increases overall resolution of the technique. Additionally, this technique no longer detects the absorption of electromagnetic radiation. This technique works by exciting a rotational state through a pulse of electromagnetic radiation, turning the off the light source, and detecting what is called the Free Induction Decay (FID). This is analogous to the FID that is commonly known in Nuclear Magnetic Resonance (NMR). The FID is the decay of the excited rotational states back to the ground state, which can take multiple microseconds to occur.

This is a time domain signal that is Fourier transformed to obtain the molecular spectra. This method is inherently more sensitive than detecting the signal directly. The major drawback of this technique is it is narrowband, typically only scanning 500 KHz at once, which could make detecting the entire molecular spectra very time consuming.

Finally, in 2008, Pate, et al… introduced the Chirped Pulse Fourier Transform Microwave Spectrometer (CP-FTMW) [7]. This is a broadband technique capable of scanning multiple GHz in a single experiment. The original technique requires using two directionalized antennas – one for sending, one for receiving – to excite the rotational states and detect the FID. As opposed to the Balle-Flygare instrument, this technique requires specialized and expensive equipment to generate and receive the broadband signal. This equipment is oftentimes more expensive and can be cost prohibitive. Additionally, because there are no mirrors involved, there is only one pass through the sample (down for 10,000-20,000) making this technique significantly less sensitive. The CP-FTMW is slightly less resolved than the Balle-Flygare cavity, as well.

Despite these drawbacks, however, the CP-FTMW has revolutionized the field of microwave spectroscopy. The technique may be inherently less sensitive due to only one pass of the microwave radiation through the sample, but it is capable of rapidly sampling a broadband spectrum. As will be demonstrated later, it is possible to obtain FIDs of broadband spectra at a rate upwards of 25Hz. This makes it possible to obtain a molecules entire spectra in a matter of days as opposed to weeks.

2.2. INSTRUMENTATION THEORY

The CP-FTMW and Balle-Flygare instruments are made possible due to the fast-passage technique [8] developed by J.C. McGurk et al… in 1974. This technique involves sweeping the frequency of the excitation source through the excitation frequency for a rotational transition and measuring the relaxation of that state. This can be described by the Bloch Equations, which are a set of 3 coupled differential equations, in equation (40) that can also be found in [8].

$$\frac{dP_r}{dt} + \Delta\omega P_i + \frac{P_r}{T_2} = 0 \tag{40}$$

$$\frac{dP_i}{dt} - \Delta\omega P_r + \kappa^2 \delta \left(\frac{\hbar \Delta N}{4}\right) + \frac{P_i}{T_2} = 0$$

$$\frac{d}{dt}\left(\frac{\hbar \Delta N}{4}\right) - \delta P_i + \frac{\frac{\hbar}{4}(\Delta N - \Delta N_0)}{T_1} = 0$$

$$\Delta\omega = \omega_0 - \omega, \kappa = \frac{2}{\hbar}\langle a|\mu|b\rangle$$

In the previous equations ω_0 is transition frequency, ω is the radiation frequency, μ is the dipole moment. The variables a and b are the respective upper and lower levels. T_1 and T_2 are the relaxation times for the population difference and polarization and P_i and P_r are the real and imaginary polarization terms. ΔN and ΔN_0 are the population difference between two states and at given times. Finally, δ is a function of z and t. Solving these equations requires assuming that ΔN remains relatively constant such that $\Delta N = \Delta N_0$ and to neglect any collisional damping terms in (40). Using these assumptions and defining the sweep speed, α, such that $\alpha = \frac{d(\Delta\omega)}{dt}$ the following equations can be obtained.

$$\alpha \frac{dP_r}{d\Delta\omega} + \Delta\omega P_i = 0 \qquad (41)$$

$$\alpha \frac{dP_i}{d\Delta\omega} - \Delta\omega + \frac{\hbar\kappa^2\delta}{4}\Delta N = 0$$

$$\alpha \frac{d}{d\Delta\omega}\left(\frac{\hbar\Delta N}{4}\right) - \delta P_i = 0$$

Solving these equations will yield mathematical expressions for the pulse polarization, signal at the detector, and so on. This is all carried out in detail within [8]. From these equations, however, it is immediately possible to determine that the excitation response of a rotational transition using a fast passage technique will depend on the frequency range, $\Delta\omega$, and time spent sweeping through that frequency range. This is intuitive as more power will inherently excite more transitions. Power can be considered analogous to the inverse of the sweep speed α. A shorter frequency range will elicit more power, as will a longer sweep time.

Physically what is occurring with equations (40) and (41) is that when an electromagnetic wave is swept in frequency through a gas phase sample, it is possible for a molecule containing a permanent electric dipole to interact via the fast passage process. As the frequency of the electromagnetic wave approaches that of a rotational transition for the molecule, the molecule will begin to rotate. When the electromagnetic wave is turned off, or the sweep is sufficiently past the excitation frequency, the molecule will relax from the excited rotational state through a Free Induction Decay (FID). The strength of the free induction decay depends on the dipole strength, polarization power, and population.

In a typical modern experiment, the FID will be collected and Fourier transformed. Typical FIDs exist on the order of 10-100μs, so what is physically being

detected by the experiment is the rotation of the electric dipole of a molecule in an

excited rotational state until that molecule decays back to a lower rotational state. The

oscillating electric field lines, which can be seen for a dipole in Figure 2.1, are detected

by an antenna which transduces this to a voltage. An example of a FID can be seen in

Figure 2.2.
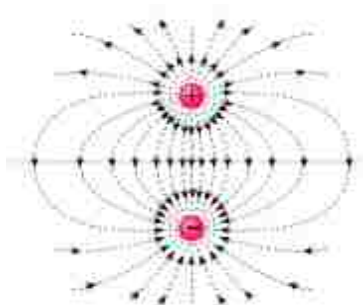
Figure 2.1. The electric field lines of a dipole [9].
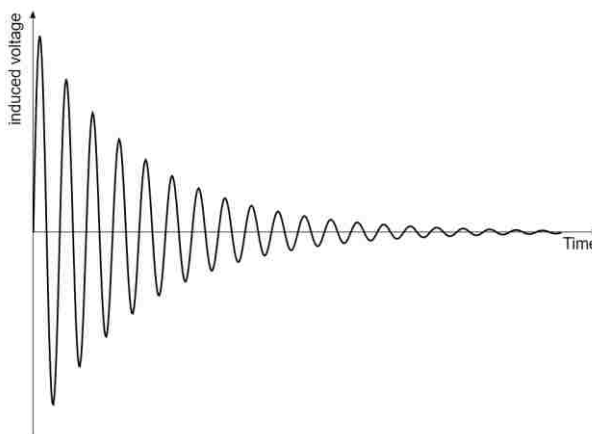
Figure 2.2. An example of a FID [10].

What happens in a Balle-Flygare or CP-FTMW instrument is the FID is Fourier

Transformed. This process transforms the signal from a time domain to a frequency

domain. The resulting signal is composed of the various frequencies and their

corresponding amplitudes. Collecting in the time domain in the time domain and

transforming to the frequency domain has advantages in that it increases resolution and

allows for broadband collection. A Fourier transform is defined as follows

$$F(\omega) = \int_{-\infty}^{\infty} f(t)e^{-i\omega t}dt \tag{22}$$

Oftentimes, however, applying a Fourier transformation requires it to be done

numerically, which equation (42) is not suited for. This requires the use of the Fast

Fourier Transform (FFT) through the Cooley-Tuckey algorithm [11]. Increasing the

resolution of the FFT can be done by increasing the amount of time a FID is collected,

however this can be difficult for the experiment hardware to do. Typical resolution of

these experiments, because of the 10-100µs FID time, is on the order of kHz. Typical

linewidths are on the order of 80-100kHz at their full width-half max (FWHM).

2.3. THE MISSOURI S&T CHIRPED PULSE FOURIER TRANSFORM MICROWAVE SPECTROMETER

Up to this point the theory has focused on around both the Balle-Flygare Fourier

transform microwave spectrometer as well as the CP-FTMW, however most of the works

in the later sections will focus primarily around the use of the CP-FTMW. Most of the

use of the Balle-Flygare instrument will revolve around obtaining more detailed

information on the broadband spectra obtained by the CP-FTMW. Because of this only

the CP-FTMW, specifically the Missouri S&T CP-FTMW, will be discussed beyond this

point.

The CP-FTMW at Missouri S&T was designed to be a low noise, high fidelity

instrument. In order to do this, the number of components had to be minimized. To

accomplish minimizing parts, circuit functionality had to be made up for in other

components. This was done by using a high quality Arbitrary Waveform Generator

(AWG) and oscilloscope. Figure 2.3 contains a detailed circuit diagram of the CP-

FTMW.

The CP-FTMW components are kept in synch by components 1 and 2 in Figure

2.3, which are a 5 and 10 MHz frequency Rubidium standard clock, produced by

Stanford Research Systems, with an amplifier. Component 3 is a Tektronix Arbitrary

Waveform Generator, model AWG70001A, which has a 50 GS/s digitization rate and

capable of produced waveforms up to 20GHz. Linear frequency sweeps, or Chirps, are

generated by MatLab scripts that are imported into a proprietary Tektronix program.

Typical chirps are 4μs in duration and approximately 4.75GHz in bandwidth. Three

overlapping bandwidth ranges from 5.5-10.25 GHz, 9.75-14.5 GHz, and 14-18.75 GHz

are typically used to obtain spectra in the 6-18 GHz region. This is done as the AWG is

typically less effective for the first and last 500 MHz of a chirp, so spectra are overlapped

to minimize this effect. These chirps are fed into component 4, which is a 40 W TTL

controlled Microsemi solid state amplifier for the 6-18 GHz range. For the 2-8 GHz

range, component 4 is a 50 W TLL controlled solid state amplifier, model SPA-060-50-

SMA by Fairview Microwave. The signal is then sent into a custom vacuum chamber,

which is vacuumed down by a Varian VHS-10 diffusion pump, which is backed by an

Edwards 40 rotary pump. The signal is both sent and received by two Qpar 2-18 GHz

high gain ridged horn antennae, which are both component 5. Component 6 is a TTL

controlled, single pole, single throw switch purchased from ATM. This switch exists to

both protect components 7 and 8 from the excitation pulse, which has enough power to

destroy the sensitive electronics, and also the FID signal to pass when the excitation pulse

is turned off. The signal is amplified by an L3 Narda Miteq JS42-06001800-18-8P low

noise amplifier in the 6-18 GHz range. Component 7 for the 2-8 GHz range is a model

AFS44-00101000-20-10P-44 low noise amplifier by L3 Narda Miteq. Component 8 is the

oscilloscope, a Tektronix model DPO72304DX. This oscilloscope is 100GS/s and 23

GHz bandwidth, which helps to eliminate excess circuitry due to the high bandwidth

available. The oscilloscope is responsible for analyzing and saving the data. The

FastFrame software available on this scope allows for multiple data acquisitions per

nozzle pulse. The nozzle, component 10, is a series 9 Parker-Hannifin solenoid valve

with a 0.8 mm orifice. Component 10 is controlled by component 9, which is the Parker-

Hannifin pulse driver.
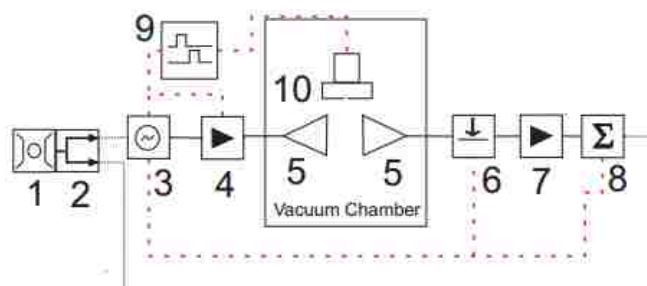
Figure 2.3. The circuit diagram for the Missouri S&T CP-FTMW. The red dotted lines
are TTL control cables, while the solid grey lines are microwave cables, and finally the
dotted grey lines are reference frequencies. The components are as follows: 1,2) 5, 10
MHz Rubidium Frequency Standard by Stanford Research Systems. 3) Tektronix
AWG70001A AWG. 4) 40 W Microsemi solid state amplifier. 5) Qpar 2-18 GHz high
gain ridged horn antenna. 6) Single pole, single throw switch by ATM. 6) L3 Narda
Miteq JS42-06001800-18-8P low noise amplifier. 8) Tektronix DPO72304DX. 9) Parker-
Hannifin nozzle pulse driver. 10) Parker-Hannifin series 9 supersonic pulse valve.

The Tektronix AWG part of the reason the circuit is able to be simplified. It is capable of generating any waveform necessary with a range from DC to 20GHz. Additionally, the AWG has an extremely stable clock that can be used to synch all components if components 1 and 2 are not available. Being able to generate stable, high frequency, broadband signals without having to mix multiple waveforms together effectively reduces the required circuitry, improves signal by removing harmonics from mixing, and reduces noise. The AWG controls logic to multiple switches and amplifiers so that the signal can safely flow through the circuit, without damaging any sensitive equipment.

More important than the AWG is the broadband oscilloscope. Being able to directly digitize the signal, as opposed to having to mix down like in the past, will improve signal quality and strength. Every component introduced into a circuit will lose signal due to things like connectors or cables, which inherently are not efficient in transferring signal. Additionally, each component will introduce noise. What would happen in previous setups is, after the low noise amplifier, the signal would need to be mixed down from a high frequency signal to a lower frequency signal so that an oscilloscope could handle the data. The parts it took to do this would weaken the signal and reduce fidelity before the signal could be analyzed by the oscilloscope. This limits the frequency range of the spectrometer, but with the advent of the new generations of high speed oscilloscopes this is beginning to not be an issue.

In addition to direct digitization, this oscilloscope has an advantages in how quickly it can collect FIDs. Through the use of the aforementioned FastFrame software, it is possible to collect multiple FIDs per second. This allows for conservation of sample,

which leads to more averages, which reduces the noise level and allows for detection of weak transitions. The Missouri S&T CP-FTMW operates with 5 gas pulses per second and 5 FIDs per gas pulse, which yields a theoretical collection of 25 FIDs per second. Due to yet unknown hardware limitations, however, only about 50-60% of the theoretical FIDs per second are *actually* collected. This effect seems to scale with the amount of gas pulses and FIDs per gas pulse, which favors simply increasing the amount of gas pulses and FIDs per gas pulse. Due to restrictions from the vacuum and weakened signal from too many FIDs per gas pulse, however, the best number seems to be 5 gas pulses per second with 5 FIDs.

As previously mentioned, components 1 and 2, as well as the AWG, are used for synchronizing components. This is important for repeatedly adding FIDs together when averaging molecular spectra. Averaging spectra will improve the signal to noise ratio as a function of $\frac{1}{\sqrt{n}}$, where n is the number of averages. What this means is that, because background noise will not come in consistently at a specific frequency, repeatedly adding FIDs together will reduce the background noise. Only the signals that appear at the same frequency in every FID will add together, which will allow even very weak signals to appear out of the noise with enough averaging. If the FIDs are not consistently phase locked, or synchronized, then these signals will not consistently add together. This will mean that averaging will cause even consistent signals to not add together and emerge from the noise.

Components 4 and 7 are both amplifiers. These components exist to take a weak signal and make it significantly stronger, however they do not do this in the same way. Component 4 is a power amplifier. It takes the weak signal from the AWG, which is on

the order of 100mW, and amplifies this to the order of watts. This amplifier will amplify

every signal in the line, though it will potentially not amplify every signal at the same

efficiency. Increasing the power of the AWG signal will lead to a larger molecular signal.

Component 7 is a low noise amplifier. This amplifier exists to amplify signal above a

certain threshold so that it does not amplify and introduce noise in to the spectra. This

exists to take a very weak molecular signal, which may be only ~5μV (but likely much

less) for very strong molecules, and increase that signal strength more than 100 times.

Component 5 are the directionalized horn antennae. These are what allow

broadband transmission. The Balle-Flygare instrument worked by creating a standing

wave between two mirrors, which were positioned with very precise spacing. This

technique would only have around 500 kHz of bandwidth. Moving to broadband antenna

allows for easy transmission and detection of a broadband waveform with an even power

distribution.

Finally, component 10 is the supersonic pulsed nozzle. The benefits of this have

been mentioned previously to an extent. This nozzle is responsible for introducing

collision free, rotationally cooled gas into the vacuum chamber. This nozzle will be the

basis of the various sourcing techniques discussed in the following sections.

2.4. STANDARD PULSE NOZZLE

The series 9 Parker-Hannifin is a spring loaded solenoid valve that is used to

insert gas into the vacuum chamber. The nozzle is composed of a solenoid, armature, two

springs to create tension, and a poppit. A complete diagram can be found in Figure 2.4

below. The poppit is a small, typically Teflon, component that is used to plug a 0.8 mm

orifice in the nozzle head. The poppit rests inside the armature, which is a magnetic

component that can interact with the magnetic pulses generated by the solenoid valve.

The springs exist to create tension that prevent the poppit from leaking gas when the

nozzle is not in operation.
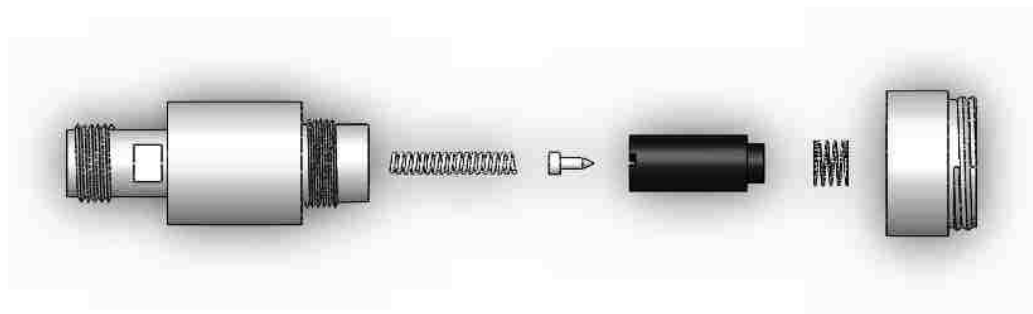
Figure 2.4. The series 9 Parker- Hannefin solenoid valve. From left to right is as follows: the solenoid, a tensioning spring, the poppit, the armature, another tensioning spring, and the nozzle head with a 0.8mm orifice.

The solenoid valve can only operate when current is introduced. The current,

which flows in a circular path in the solenoid, creates a magnetic force that pushes the

armature back. This motion carries with it the poppit, which will allow gas to enter the

vacuum chamber. This duration of this action can be controlled simply by controlling

how long the current is allowed to flow through the solenoid. This enables optimization

of the amount of gas that is allowed to enter the vacuum chamber.

A gas mixture is typically pulsed into the vacuum chamber, which is held at a

pressure on the order of 10^{-6} torr. Compared to that of the vacuum chamber, the gas in the

nozzle is a high pressure. This process creates a molecular beam, which means the

molecules have a narrow speed distribution. This similarity between speeds is what

makes the gas collision free. The speed distribution is controlled by equation (43), which

is known as Maxwell's Speed Distribution.

$$f(v) = 4\pi(\frac{M}{2\pi RT})^{\frac{3}{2}}v^2 e^{-\frac{Mv^2}{2RT}} \tag{43}$$

In which M is the molecular weight of the gas, R is the gas constant, T is the

temperature, and v is the velocity of the gas. The width of the distribution, which defines

the distribution of speeds, is defined solely by M and T. Decreasing the temperature will

yield narrower speed distributions, as will decreasing the molecular mass. This narrow

speed distribution yields a cold translational temperature and a slightly warmer rotational

temperature, but the vibrational temperatures are unaffected. Experimental temperatures

range from 0.3 K translationally and 1-4 K rotationally [6]. Cooling the molecules in such

a manner will force the molecules into a low rotational state to allow for controlled

excitation to higher states.

Additionally, it is for these reasons that typical gas mixtures only constitute, on

average, 3% sample and 97% carrier gas. The carrier gas will contain most of the mass of

the gas pulse, which will control the speed – and therefore the temperature – according to

equation (43). Typical backing gasses are Argon, Helium, Neon, and sometimes Xenon.

Argon, however, is the most common.

Typical backing pressures for experiments can vary dramatically. For regular

species, it has been found for the Missouri S&T CP-FTMW that backing pressures

ranging from -5inHg to -25inHg relative to atmosphere are preferred. For van der Waals

complexes, this may increase from -10inHg to 15psig, where psig denotes pressure

relative to, and above, atmospheric pressure. For various sourcing techniques, such as the

heated nozzle and laser ablation, pressures are typically 30psig and above. This was discovered while studying Ar-HCl, which will be discussed in later chapters.

Examples of the effectiveness of the pulsed solenoid valve in the Missouri S&T CP-FTMW can be found in chapters 3, 4, 5, and 6. Chapters 3 and 4 will cover the molecules *trans*-3-Bromo-1,1,1,2,2-pentafluoropropane and bromoperfluoroacetone, respectively, that will detail the initial function of the CP-FTMW. Chapter 5 will cover the complex of Ar-HCl, which will discuss the effects of signal improvement due to low backing pressures and the specialized regulators used to accomplish this. Chapter 6 will discuss the synthesis and analysis of 1,1-difluorosilacyclapent-2-ene, which will detail the most recent configuration of the CP-FTMW with minimized cable lengths to further improve signal.

2.5. HEATED NOZZLE

As has been mentioned previously, rotational spectroscopy is a gas phase technique. In order to study a liquid or solid sample an apparatus must exist to transform the molecule into the gas phase. For liquids this process is typically rather easy. If the liquid is volatile then typically all that is required is to put 1-2 mL of liquid into the gas line and allow gas to bubble through the liquid, picking up vapor as it goes. An improvement to this method would be connecting a glass "U" shaped tube to the gas line. This allows for sample to be heated to a higher degree without risking the integrity of the line. Chapters 7 and 8 will discuss the molecules Verbenone and Ar-1,3-Difluorobenzene that utilized the glass U-tube for sampling.

This method of putting liquid into the gas line/U-tube is effective, but it has multiple disadvantages. It is reliant on the vapor pressure of the gas. Should the vapor pressure of the molecule be low, then not much sample will be carried with the gas, leading to a weak spectra. Additionally, typically the liquid sample is place a relatively long distance away from the nozzle to avoid directly injecting liquid into the vacuum chamber. This causes an opportunity for the sample vapor to condense, further weakening the molecular spectra. These issues can be addressed by introducing a heating mechanism around the liquid sample, however the sample vapor still has an opportunity to cool down and condense before entering the vacuum chamber.

An alternative to placing the sample directly in the gas line, or in the glass U-tube, would be to design a component with a reservoir that would replace the end cap that can be seen in Figure 2.4. A design for such a component, which can be seen in Figure 2.5, could be coupled with a heater to help increase the vapor of non-volatile samples. This method completely eliminates the chance for liquid to condense before entering the vacuum chamber, which dramatically increases signal.

Figure 2.5 shows a diagram of the heated nozzle head that was inspired by Suenram et al [13]. The changes to the design were two-fold. First, the nozzle head was designed such that it could be taken apart without removing the nozzle. This was important as how tight the nozzle is screwed in is a key-parameter for optimizing the expansion. Removing the nozzle to refill the reservoir, which has to be done frequently, changes this parameter and can lead to a worse overall signal. The tradeoff for this is that it can be difficult to remove/join the two halves of the reservoir, but with practice this becomes easier. The second change was overall reservoir size. This reservoir was design

to hold 3 mL of water at room temperature. The main drawback to this is the increase in size which, as the component is machined out of stainless steel, can make it heavy.
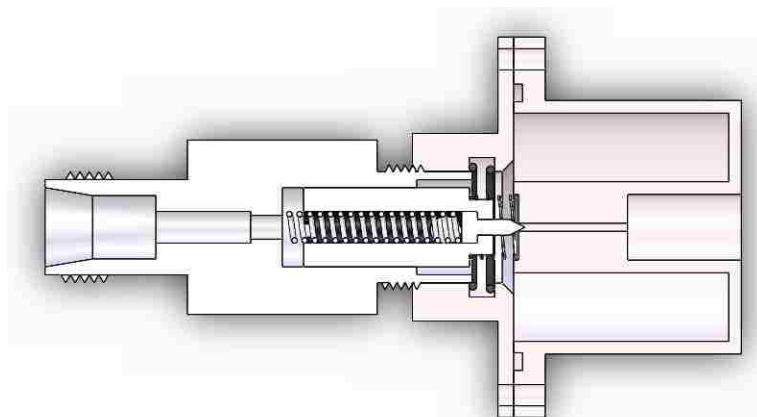
Figure 2.5. CAD image of the heated nozzle modified from Suenram et al.[13]

The heated nozzle is heated by a Chromalox MB1A1A1A1 clam shell heater. This is a 100W heater that wraps around the reservoir to apply heat directly where it is needed. The temperature is controlled by varying the 120V power supply through the use of a VaryAC. The temperature is monitored through the use of a MAX31855 K-type thermocouple that feeds into an AD595 thermocouple interface chip that collects, amplifies, and converts the signal to a voltage. This voltage is then monitored by an Arduino Uno and converted to a temperature.

Though multiple molecules have been run and analyzed through the heated nozzle, the main one that will be talked about is the molecule Myrtenol. This molecule, which is in the same family as Verbenone, was initially run through the U-tube and no signal was obtained. The heated nozzle improved signal enough to observe a strong

Myrtenol signal. Comparing Myrtenol and Verbenone can be used as a basis for how the heated nozzle improves signal.

2.6. LASER ABLATION SOURCE

Section 2.4 talked about the basic sourcing technique for gasses and Section 2.5 talked about the various sourcing techniques for liquids. Solids, however, require a significantly different approach. In order to sublimate a solid it requires a relatively high amount of energy over a short period of time, or high power. To accomplish this it is useful to use a high power pulsed laser. Ablating materials typically requires that the material being ablated has a fresh surface, meaning it recently has not had a laser fired at it. This means achieving a laser ablation source requires the interface of a gas nozzle, a metal, and a laser. The design from the Missouri S&T laser ablation source can be found in Figure 2.6.
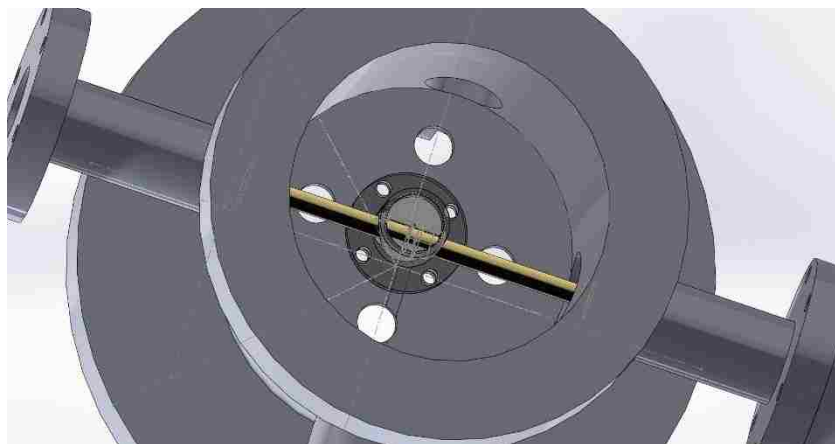
Figure 2.6. The laser ablation set up at Missouri S&T. Pictured is a gold metal rod interacting with the Walker-Gerry nozzle[14], which will interface with the solenoid valve.

The Missouri S&T design incorporates the Walker-Gerry nozzle [14], which includes a small orifice for a laser, a 0.25 in diameter hole for a metal rod, and an entrance/exit hole for gasses. The complete nozzle set up can be seen in Figure 2.7.
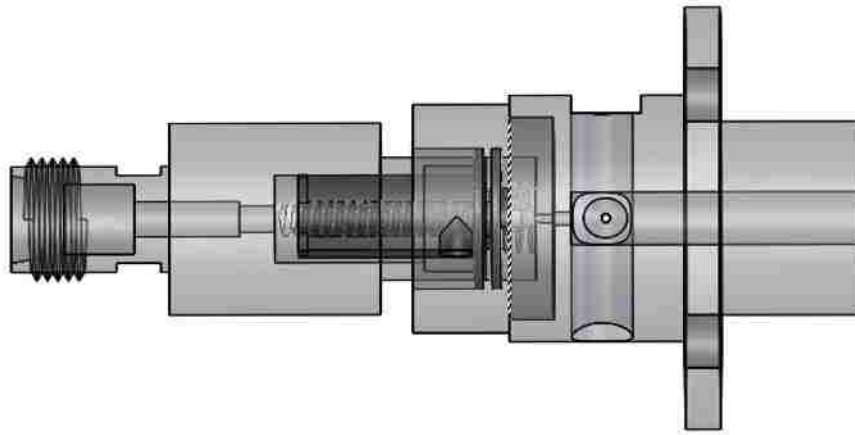
Figure 2.7. The Walker-Gerry nozzle attached to the solenoid valve.

Designing the flange that would interface the Walker-Gerry nozzle, metal rod, and laser was done using SolidWorks 2014. The overall design was tedious as it required that these three points intersect at one point in space within a cylindrical vacuum flange.

Providing a fresh surface for the laser was achieved by designing a special set up, called the "motor mike" that would rotate and translate a 0.25 inch diameter rod of a material. Rotation and translation of the rod were achieved in one action by attach the rod to ace Acme rod. Acme rods are effectively special screws with specialized, low friction threads. The Acme rod was turned by connecting it to a Micromo 1516E012SR motor with 485:1 gearbox. Position and travel length of the rod were controlled through the use of two TT Electronics OPB420BZ trip switches. The position of these trip switches were

adjustable. When it was sensed that a motor had moved within the vicinity of one of the switches a program would tell the motor to reverse direction. A complete diagram of this design can be seen in Figure 2.8.
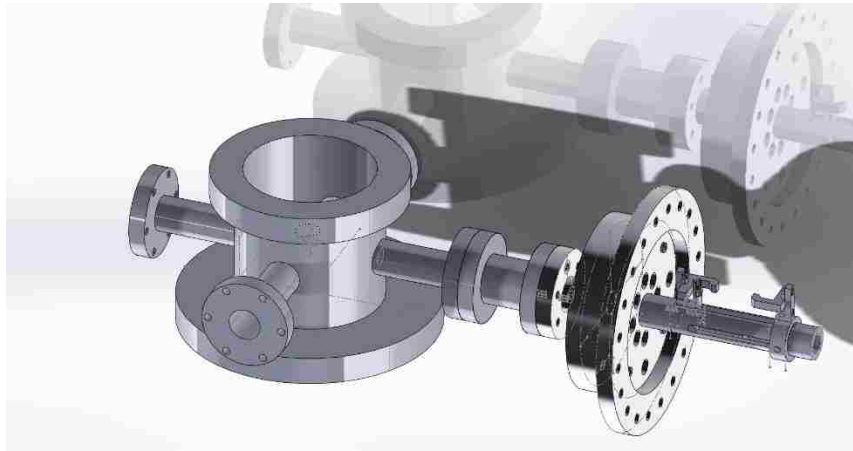
Figure 2.8. The motor mike design.

Controlling the trip switches required specialized circuitry. These switches are effectively an IR light source and an IR detector. When the IR detector senses IR light it will output a current, which means when something "trips" the switch it will output less current. Unfortunately microcontrollers, like the Arduino Uno used to control this set up, do not sense current. This means that the current must be converted to a voltage. Traditional current-to-voltage converters, called Hall Effect sensors, use the Hall Effect, which states that a magnetic field (from a current) produces a voltage in a direction perpendicular to the flow of current. This method, however, was too noisy to detect the small currents put out by the trip switches. Even introduced resistive/capacitive filters could not reliable resolve the difference in currents. The Hall Effect sensors were then switched out for more specialized, more complex sensors called transimpedance

amplifiers. These amplifiers utilize an operational amplifier with a special resistor configuration, as seen in Figure 2.9. It is out of the scope of this document to discuss how transimpedance amplifiers work, hoever it is sufficient to say that carefully constructed transimpedance amplifers are capable of detecting currents as low as 10^{-12} amps.
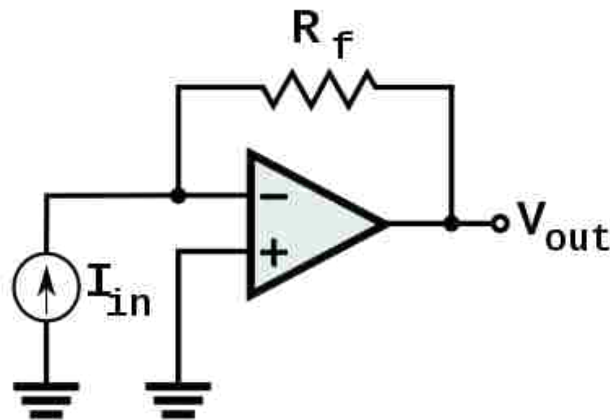
Figure 2.9. A typical transimpedance amplifier design[15].

The difference in signal between the Hall Effect sensor and the transimpedance amplifier can be seen in Figure 2.10. Transimpedance amplifiers will not produce a signal when they sense no current, so when the trip switches are "tripped", the amplifier will send out a near-zero voltage. This leads to a pronounced, reliable difference in signal regardless of the amount of noise.

The transimpedance amplifier yielding a good difference in signals made it possible to control the length and direction at which the rod turned. This was done by feeding the output of the transimpedance amplifier into an Arduino Uno. When the output of the transimpedance amplifer reached a certain threshold, typically 30, the motor would change directions.
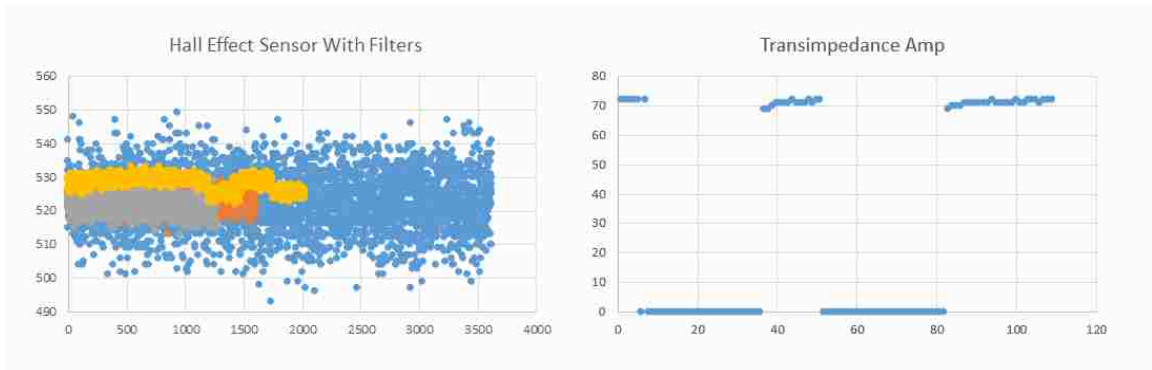
Figure 2.10. Hall effect sensor signal. (Left) the half effect sensor output with various RLC filters. (Right) The output of a transimpedance filter. The dips in signal are caused by an object tripping the trip switch.

Finally, the laser was focused onto the rod through the use of a lens mounting system, which can be found in Figure 2.11. This system allows for the lens, a Thorlabs LB1437-C biconvex lens, to be easily positioned for optimal alignment of the laser, through the aperture of the Walker-Gerry nozzle, and onto the rod.

Figure 2.11. The lens mounting system for the laser ablation source.

PAPER

I. HIGH RESOLUTION SPECTROSCOPY NEAR THE CONTINUUM LIMIT: THE MICROWAVE SPECTRUM OF *TRANS*-3-BROMO-1,1,1,2,2-PENTAFLUOROPROPANE

ABSTRACT

The microwave spectrum of 3-bromo-1,1,1,2,2-pentafluoropropane has been observed using CP-FTMW spectroscopy. Potential energy scans have been performed and confirm the existence of two conformers - trans and gauche - for which further structural optimizations and electric field gradient calculations have been performed in order to get highly accurate nuclear quadrupole coupling constants for assignment purposes. The combination of multiple conformers and large nuclear quadrupole coupling constants produce a very dense spectrum at an estimated 1 transition/MHz, near the continuum limit. This spectral density makes it necessary to have very sophisticated computational approaches in order to get geometric and electronic structures that are very close to experimental observation. Analysis of the spectrum allowed for the assignment of the trans conformer, but the gauche proved to be prohibitive, although it is believed to be present in the current spectrum. Full analysis of the rotational spectroscopic parameters of two isotopologues-the 79Br and 81Br-have been observed and are reported. Geometric analysis of the experimentally observed conformer is also reported using Kraitchman coordinate and second moments arguments. Further analysis of the spectrum reveals the occurrence of dipole-forbidden, nuclear quadrupole allowed transitions with one forbidden transition possessing known x -type forbidden transition linkage pathway.

1. INTRODUCTION

Since the work of Javan [16] on the three-state maser and their discovery by Oka [17], there has been much work on electric dipole-forbidden, perturbation-allowed rotational transitions by multiple groups [18-21]. In many of these instances, the spectra observed and reported leverage some simple spectral caveat or anomaly that provides the necessary framework for such a transition to occur. Since 2009, however, the work of Grubbs and Cooke have built upon these principles by leveraging heavier molecules with large quadrupole coupling nuclei (like Br and I) [22-27]. The combination of large quadrupole coupling constants and small rotational constants mix states of dipole-allowed transitions via off-diagonal quadrupole coupling tensor components and can amass multiple types of dipole-forbidden, quadrupole-facilitated transitions. Their work has been focused on investigating these transition pathways and understanding the breakdown of traditional selection rules. The transitions studied are typically $\Delta J = 2^-$ or $\Delta J = 3^-$ types with significant (i.e. S:N=50:1) intensity. In 2016, experiments performed on bromoperfluoroacetone [28] showed that, given the proper geometry and size of the molecule, a large quadrupole coupling nucleus could supply large values to all off-diagonal nuclear quadrupole coupling tensor components giving rise to the extremely rare x-type transition, providing evidence for the complete breakdown of K-labelling in asymmetric top systems.

A second consequence of increasing both the mass of the molecule in question and the values associated with the nuclear quadrupole coupling tensor, though, is that spectra also start to become very dense. This spectral density is quite interesting because

microwave rotational spectra are already highly resolved (<500 kHz linewidths) which provide for the observation of very small energetic differences or effects (tunneling, various spin couplings, and isotopolically resolved spectra). In order to still acquire these types of information from these spectra, then, it remains of the utmost importance to be able to fully assign spectra using Hamiltonian creation software that utilizes complete diagonalization routines in conjunction with rigorous computational methodologies that quickly and accurately predict geometric and electronic structure for many-electron systems. A few MHz disagreement between theory and experiment can mean disaster in trying to arrive at a correct assignment.

However, the atoms typically responsible for these effects, Br or I, are usually quite difficult to calculate accurately and efficiently, needing large basis sets and proper DFT treatments in order to accurately encapsulate the geometric and electronic structure of the molecules containing them. In this work we present a combined theoretical and experimental approach, analyzing the microwave rotational spectra for the previously unstudied system, *trans*-3-bromo-1,1,1,2,2-pentafluoropropane. Due to its bromine nucleus, mass, and structure, it possesses a rich, dense spectrum which provides the framework necessary for handling such difficult systems as one approaches the microwave spectrum continuum limit.

2. EXPERIMENTAL

3-bromo-1,1,1,2,2-pentafluoropropane was purchased from Synquest Laboratories R and used without further purification. Spectra were observed using a chirped pulse-

Fourier transform microwave (CP-FTMW) spectrometer located at Missouri S\&T. This spectrometer has been detailed elsewhere in the literature [28,29]. Samples of the liquid were inserted into a "U"-shaped tube approximately 40 cm upstream of the solenoid valve and covered with aluminum foil to avoid exposure to light. 6 psig of Ar was bubbled through the sample carrying vapor to the spectrometer. Separate experiments were performed utilizing the 6-12 and 12-18 GHz frequency ranges of the spectrometer's bandwidth. 4 μs chirps were utilized and the experiment was performed at 1 Hz nozzle pulsing with 1, 20 μs free induction decay (FID) being collected per gas pulse. Separate experiments of 10,000 FID averages were coadded externally and Fourier transformed using Kisiel's FFTS program using a Hanning or Bartlett windowing type [30]. 170,000 FIDs were collected for each experiment and an example of the observed spectrum in the 6-12 GHz region is located in Figure 1. Spectral linewidths ranged from 60-300 kHz FWHM with the 250 kHz arising from multiple transitions. 10 kHz uncertainty has been attributed to most line centers except for those with exceptionally large linewidths and/or blended transitions.

3. QUANTUM CHEMICAL CALCULATIONS

With such high density, high resolution spectra, it is imperative that quality quantum chemical calculations are performed at multiple starting configurations in order to achieve a successful assignment. To isolate possible monomer species in the sample, which are the most intense in molecular beam microwave spectra, the approach here was to first isolate and optimize the geometries of the lowest energy conformers of 3-bromo-

1,1,1,2,2-pentafluoropropane. The results of all following methodologies are presented in
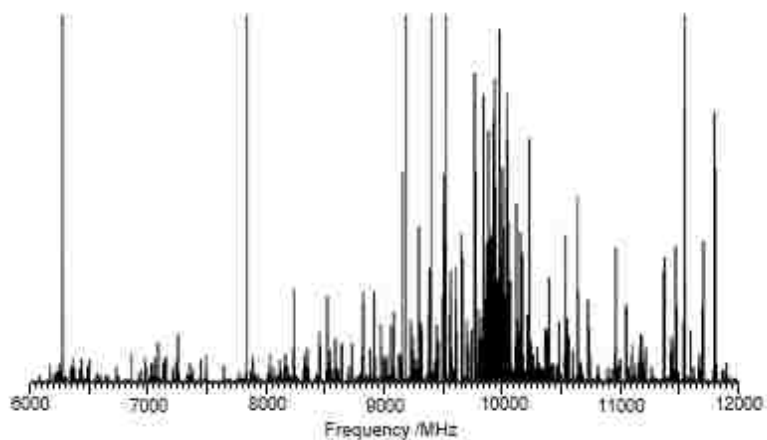
Table 1.

Figure 1**.** The resultant spectrum of the 6-12 GHz experiment of 3-bromo-1,1,1,2,2-pentafluoropropane averaged for 170k FIDs. Details of the experiment can be found in text.

Table 1**.** Quantum chemical parameters for 3-Bromo-1,1,1,2,2-pentafluoropropane for $_{79}$Br.

Parameter	*trans* Conformer	*gauche* Conformer
A / MHz	2541.0	1919.8
B / MHz	566.1	732.6
C / MHz	556.0	659.3
χ_{aa} / MHz	315.42	230.65
χ_{bb} / MHz	-195.26	-58.13
χ_{cc} / MHz	-320.16	-172.52
χ_{ab} / MHz	297.3	371.99
χ_{bc} / MHz	0.00	189.96
χ_{ac} / MHz	0.00	268.63
μ_a / D	-0.16	-0.86
μ_b / D	1.76	0.78
μ_c / D	0.00	1.52
ΔE /cm^{-1}	0	416.8

All calculations were performed using the Gaussian09 program suite [31]. To find the lowest energy conformer starting points, energy scans at the B3LYP/aug-cc-pVQZ level of theory were used. A graphical depiction of this scan is shown in Figure 2. A geometric starting structure for the scan was built using typical bond lengths and bond angles as found in the CRC handbook [32]. Because the –CF_3 group should not have a change in conformation upon rotation about the FCCF dihedral angle, the FCCBr dihedral angle was the only variable tested. Because a calculation like this is very computationally expensive, the geometry of the molecule was leveraged by having the FCCBr angle vary in 4° units starting at the *trans* configuration and ending the calculation at the 180° point. This resulted in two stable conformers, *trans -* and *gauche -* 3-bromo-1,1,1,2,2-pentafluoropropane separated by 416.8 cm^{-1} (1.19 kcal/mol).

Once the possible conformers were identified, the energy scan structures provided the starting points for optimizations performed at the MP2/6-311+G(3df,3pd) level of theory for more reliable geometrical structures. This was needed because the rotational constants for the species are relatively low - ~2500 MHz for *A* and <1000 MHz for *B* and *C* - resulting in the observed spectra having transitions moderately high in *J* even for an experiment starting at 6 GHz, so the better starting geometries result in predicted spectra closer to the experimental result.

The second calculation that was made and was crucial to assigning these spectra was the nuclear electric quadrupole coupling due to the bromine nucleus made on the optimized structure. Having a relatively large quadrupole moment for bromine - reported as 313 mb for ^{79}Br [33] - can mean exceptionally large nuclear quadrupole coupling constants (NQCCs) that will result in large splitting of rotational states (many MHz) and

various amounts of shifting in transitions. The purpose of the calculations made here,

then, are to predict [79]Br and [81]Br nuclear quadrupole coupling constants (NQCCs) of

sufficient accuracy to assist with assignment of the hyperfine structure in the microwave

spectrum of 3-bromo-1,1,1,2,2-pentafluoropropane.

Components of the NQCC tensor, x_{ij}, are related to those of the electric field

gradient tensor, q_{ij}, by

$$x_{ij}(\text{MHZ}) = \frac{eQ}{h} q_{ij}(\text{a. u.})$$ (1)

where e is the fundamental electric charge, Q is the electric quadrupole moment of the

nucleus in question, and h is Planck's constant. The coefficient $\frac{eQ}{h}$ is taken as a best-fit

parameter determined by linear regression analysis of calculated q_{ij} on the experimental

structures of a number of molecules versus experimental x_{ij}. The premise that underlies

this procedure is that errors inherent in the computational model – as well as zero-point

vibrations and relativistic effects – are systematic and can be corrected, at least partially,

by the best-fit coefficient $\frac{eQ}{h}$.

For bromine, the recommended model for calculation of the q_{ij} is

B1LYP/TZV(3df,3p) [34]. Here, B1LYP is Becke's one-parameter method with Lee-

Yang-Parr correlation as implemented by Adamo and Barone [35,36]. TZV are Ahlrichs

bases [37] augmented here with 3 sets of d and one set of f polarization functions on

heavy atoms with 3 sets of p functions on hydrogens. These polarization functions are

those recommended for use with Pople 6-311G bases, and were obtained online from the

EMSL basis set library [38,39]. Thus, for conversion of q_{ij} to x_{ij}, $\frac{eQ}{h}$ ([79]Br) = 77.628(43)

MHz/a.u. and eQ/h ([81]Br) = 64.853(40) MHz/a.u. was used [34,40].

4. RESULTS AND ANALYSIS

The quantum chemical calculations were used as a starting point for quantum number assignment. As the quantum chemical calculations predict, *trans*-3-bromo-1,1,1,2,2-pentafluoropropane is the most stable conformer and generally corresponded to the most intense transitions. Two isotopologues, [79]Br and [81]Br, were observed for the *trans* conformer and are reported in Table 2. Spectra were assigned using Pickett's SPFIT/SPCAT program suite [41] with Kisiel's AABS package [42], available from the PROSPE website [43,44], used as a front-end in order to visually observe predicted transition patterns and expedite transition assignment. In total, over 3100 transitions were assigned with obs-calc residuals less than or equal to 3σ of the line center uncertainty. These transitions primarily consisted of strong P-, Q-, and R-branch, *b*-type transitions and much weaker R-branch, *a*-type transitions, in accordance with the predicted dipole moment values reported in Table 1. The spectra were fit using a Watson S-reduced Hamiltonian [45] in the I^r representation. All quartic centrifugal distortion constants arising from this reduction Hamiltonian were determined. All diagonal components and one off-diagonal component, x_{ab}, of the nuclear quadrupole coupling tensor arising from the bromine nucleus was also determined. A complete list of all assigned transitions and fits can be found in the Supplemental Information.

After this assignment was made, the *gauche* conformer was tried for by subtracting out the assigned transitions of the *trans* conformer utilizing the "blank lines" function of the SVIEW program in the AABS package and using the calculated spectroscopic constants of Table 1 as a starting point, but an adequate fit to

Table 2. Spectroscopic Parameters for *trans*-3-bromo-1,1,1,2,2-pentafluoropropane.

Parameter	$C_3H_2{}^{79}BrF_5$	$C_3H_2{}^{81}BrF_5$
A / MHz	2536.1957(1)[a]	2535.9158(1)
B / MHz	561.65607(3)	555.39358(3)
C / MHz	551.65213(3)	545.59653(3)
D_J / kHz	0.01710(3)	0.01691(3)
D_{JK} / kHz	0.2190(2)	0.2166(2)
D_K / kHz	0.1042(4)	0.1064(4)
d_1 / Hz	-0.121(7)	-0.137(8)
d_2 / Hz	0.028(2)	0.030(2)
χ_{aa} / MHz	510.051(4)	425.762(5)
χ_{bb} / MHz	-191.851(6)	-159.932(6)
χ_{cc} / MHz	-318.199(6)	-265.830(6)
χ_{ab} / MHz	300.06(1)	251.10(1)
χ_{zz} / MHz	620.839(7)	518.675(8)
χ_{xx} / MHz	-302.639(8)	-252.844(8)
χ_{yy} / MHz	-318.199(6)	-265.830(6)
η^b / MHz	0.02506(2)	0.02504(2)
θ_{za} /	20.2651(5)	20.3056(6)
MW $\sigma_{rms}{}^c$ / kHz	12.4	12.4
$\sigma_{rms}{}^a$	1.22	1.23
N^e	1676	1468

spectroscopic parameters could not be reached. Reasons for this impasse can be found the *Discussion* section. In addition, no ^{13}C isotopologue spectra in natural abundance were assigned as the spectral density along with the weakness of these species caused considerable problems with transition observation and assignment.

4.1. NEAR CONTINUUM LIMIT

As shown in Figure 3, the resulting spectrum of 3-bromo-1,1,1,2,2-pentafluoropropane is very dense. The density of the observed species is 1 transition/4 MHz, but there are many remaining unassigned transitions. Overall, the spectral density arising from all transitions is estimated to be on the order of 1 transition/MHz, putting it near the continuum limit, even for such high resolution. The way the authors dealt with this assignment problem is discussed in the next section
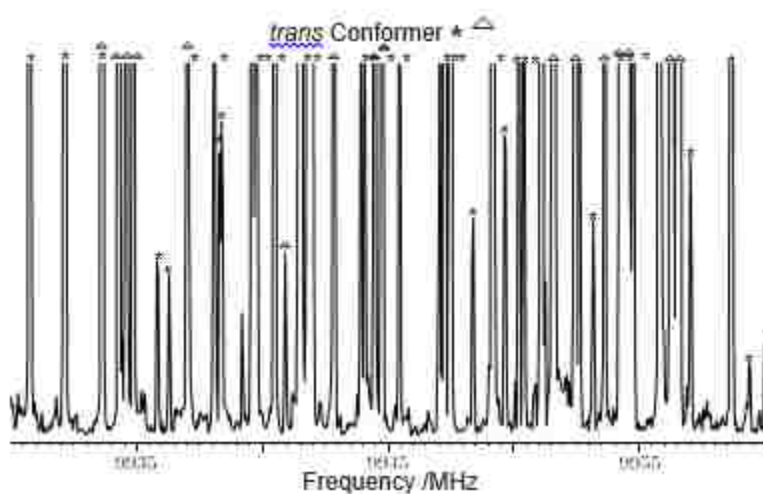
Figure 2. A portion of the observed 3-bromo-1,1,1,2,2-pentafluoropropane spectrum in the range of 9930-9960 MHz. The zoom-in portion illustrates the spectral density observed in many ranges of the spectrum. The ^{79}Br and ^{81}Br of the *trans* conformer have been marked with G and * respectively.

5. DISCUSSION

5.1. ASSIGNING NEAR-CONTINUUM SPECTRA

CP-FTMW spectroscopy has changed the paradigm with respect to how rotational spectra are approached. Instead of identifying a system, using sophisticated computational methods, and searching for a particular spectrum, now one will introduce a sample into the spectrometer and identify systems within the resultant broadband spectrum using known spectral catalogs, quantum chemical methodologies, and assignment routines or personal prowess. This is because fast acquisitioning and deep averaging capabilities of the oscilloscopes allow for many averages of the FIDs produced from each molecular excitation. Since problems of cavity drift and narrowband power regions are eliminated, the deep averaging limit, sample consumption, and time become

the only absolute obstacles of the experiment apart from the required possession of a dipole moment and the species be in the gas phase. This is a huge advantage and has led to new methodologies including, but not limited to custom sourcing techniques [46,47], chiral tagging experiments [48], and coherent light experiments with chiral molecules [49,50].

However, these new possibilities also come with some inherent problems. One problem is that of spectral density. CP-FTMW spectroscopy, being a pure rotational spectroscopy technique, produces spectra that are various combinations of rotational constants based on the dipole moments of the molecular system of study. These rotational constants are inversely proportional to the moments of inertia about each principal axis. Furthermore, the intensities of the resultant spectra are governed by the system's statistical mechanics and dipole moment vector components in the principal axis system. As systems become large, rotational constants become small, creating dense spectra that are generally weaker in intensity, making assignment a challenging process. This is particularly true with chiral tagging experiments where the systems are governed by complexation chemistry, size, and number of produced diastereomers. Furthermore, additional angular momenta (like quadrupole coupling nuclei) can further split and spread spectra out making assignment, even with automated routines, a very difficult task.

This is where truly powerful computational methodologies and assignment tools can be of significant use in CP-FTMW spectroscopic techniques. Grimme has done work in this area using DFT methodologies in order to get very accurate rotational constants [51] which has proven useful for large biomolecules like verbenone [52]. 3-bromo-1,1,1,2,2-pentafluoropropane poses a different challenge, though, because it is a large

system (possesses 100 electrons and has an atomic mass of 212 amu for the ^{79}Br isotope) that has two conformers - *trans* and *gauche* - with very different electronic and geometric structures, producing very different sets of rotational constants, NQCC tensors, and dipole moments. These different values produce very different microwave spectra, but a small change in any single parameter is detrimental to achieving a correct assignment. This proved to be problematic when trying to assign the *gauche* conformer because there was no discernable pattern that manifested itself from the predicted spectroscopic constants, even when using iterative values of the rotational and NQCC parameters near (within 200 MHz above and below) the predicted result. Considering that there are many more variables in assigning the *gauche* conformer, particularly the additional x_{ac} and x_{bc} parameters, and the significant predicted dipole moments along each principal axis giving *a*-type, *b*-type, and *c*-type spectra, every change in parameters significantly changed multiple patterns at the same time and this proved to be significantly difficult to make a proper assignment at the near-continuum limit. As the authors know of no automated fit routines that include nuclear quadrupole coupling parameters in their programming, this led to an impasse for moving forward with the *gauche* conformer, but the *gauche* conformer is believed to be present in the spectrum along with other possible systems (complexes, degradation species).

An example of the need for these computational methods is shown in Figure 5 for the ^{79}Br isotopologue of the *trans* conformer. As pattern recognition schemes are common and have been formulated in the literature for uncoupled rotational spectra, coupled angular momenta pattern schemes are not nearly as obvious or prevalent, making accurate calculations a dire need for accurate spectral assignment. For the *trans* ^{79}Br

isotopologue of 3-bromo-1,1,1,2,2-pentafluoropropane, the theoretically predicted

spectrum has transitions around 9700 MHz with splitting due to the quadrupole coupling

of the bromine nucleus. The corresponding experimental transitions are located about

9630-9640 MHz. Although isolating this pattern in the presence of the other spectra not

belonging to the *trans* [79]Br isotopologue is already challenging, the problem is made

much easier because the intensity of the predicted transitions and the spread are nearly

identical. Figure 5 also shows what the predicted spectra would be if the calculated x_{aa}

value was 100 MHz less. This spectra is much more difficult to identify in the

experimental spectrum showing that if NQCC values are not accurate, which can be a

common problem when calculating bromine and iodine quadrupole coupling constants,

they can greatly affect the success of achieving a successful assignment, particularly in

situations near the continuum limit.

　　　　After the first few assignments, a new prediction can be made by determining

intermediate spectroscopic constants through SPFIT and predicting new transition

patterns with SPCAT. This new prediction can then be used to add in more transitions

and the cycle can be repeated adding in more transitions and appropriate spectroscopic

constants until a suitable fit is reached containing as many transitions as observed.

Caution must be used here, though, because any small change can, as already discussed,

drastically change the predicted spectrum and get the user off track. It is suggested that

when dealing with dense spectra, the user try and assign more isolated spectra first as the

prediction and experiment will more obviously "fit" or not "fit" one another. For *trans*-3-

bromo-1,1,1,2,2-pentafluoropropane, the transitions found in Figure 3 were made first

and, as more and more transitions were added to a working fit, it was recognized that

there existed typical *b*-type, *Q*-branch patterns at approximately 10 GHz which then

greatly increased the speed of assignment and ultimately led to the successful fit

presented in Table 2.
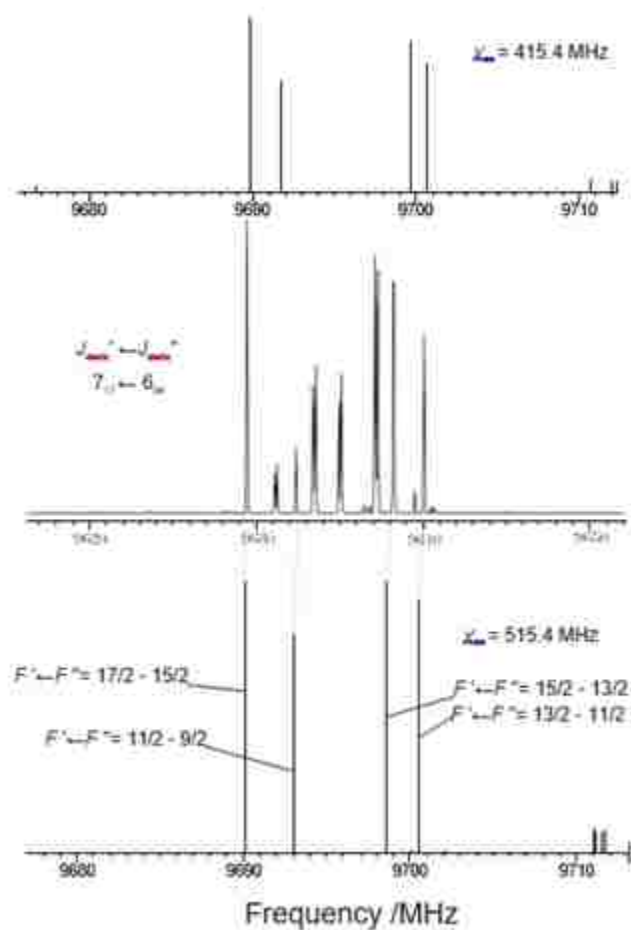
Figure 3. Comparison of predicted spectrum to observed spectrum using the quantum chemically calculated parameters. The pattern is easily picked out and assigned. Top: Reducing only the calculated x_{aa} value by 100 MHz begins to make assignment problematic.

5.2. STRUCTURAL PARAMETERS FOR *TRANS*-3-BROMO-1,1,1,2,2,-PENTAFLUOROPROPANE

As mentioned in the *Results and Analysis*, no ^{13}C isotopologue spectra in natural abundance were assigned. However, some structural insights into the molecule can still be made using the spectra that were collected and the predicted structure.

Table 3 shows a comparison of the calculated coordinates in the principal axis system and second moments to the experimentally determined values. The first piece of evidence showing the calculated structure is close to the experimental one is the fantastic agreement between the calculated coordinates and the experimentally derived Kraitchman substitution coordinates [53]. The values are virtually identical when the sign given by the calculation is assigned to the substitution coordinates and the imaginary value is considered to correspond with a value of 0. Because the bromine is the only atom that we can determine the coordinates of, we can then move to a second moment discussion keeping the placement of the bromine in the principal axis system in mind.

Second moments are a measure of the mass distribution about each axis. They are also referred to as planar moments because they are effectively a measure of the out-of-plane contribution to the mass. This means the out-of-*ab*-plane mass can be measured by P_{cc}. This is determined to be 91.47455(3) uÅ^2 for the ^{79}Br isotopologue. Using the second moment arguments of Bohn [54], the average value for P_{cc} for CF_2/CF_3 groups is approximately 45 uÅ^2. For CH_2/CH_3, the average value is 1.6 uÅ^2. Because the molecule has a CF_2, a CF_3, and a CH_2 group (ignoring the bromine which is in the plane), this gives a predicted value based on average second moments of 91.6 uÅ^2, which is closer to the determined P_{cc} value, but overestimates it, than the quantum chemical calculations, which underestimates the value slightly and produced rotational constants to within 1% of

Table 3. Calculated and experimental structural parameters for *trans*-3-Bromo-1,1,1,2,2-pentafluoropropane[a].

	Kraitchman Coordinates[38]					
	Theory			Experiment		
Atom	a	b	c	a	b	c
Carbon / Å	1.992	0.220	0.000	—	—	—
Carbon / Å	0.549	-0.322	0.000	—	—	—
Carbon / Å	-0.464	0.798	0.000	—	—	—
Fluorine / Å	0.419	-1.100	1.092	—	—	—
Fluorine / Å	0.419	-1.100	-1.092	—	—	—
Fluorine / Å	2.865	-0.775	0.000	—	—	—
Fluorine / Å	2.195	0.971	1.081	—	—	—
Fluorine / Å	2.195	0.971	-1.081	—	—	—
Hydrogen / Å	-0.334	1.403	-0.891	—	—	—
Hydrogen / Å	-0.334	1.403	0.891	—	—	—
Bromine / Å	-2.256	0.107	0.000	-2.26405(66)[b,c]	0.106(14)	0.00(30)[d]

	Second Moments[e]	
Parameter	Theory	Experiment
P_{aa} / uÅ^2	801.4	808.32700(3)[f]
P_{bb} / uÅ^2	107.6	107.79201(3)
P_{cc} / uÅ^2	91.3	91.47455(3)

[a] Values presented are for the ^{79}Br isotopologue.

[b] Numbers in parentheses represent 1σ uncertainty (67% confidence level) and are given in units of the least significant digit.

[c] Kraitchman coordinates do not give sign values, but sign given is from the calculation.

[d] Determined value is imaginary.

[e] Measure of mass distribution about each axis. $P_n = 0.5(I_i + I_k - I_l)$ where each I is a given moment of inertia corresponding to an axis.

[f] Numbers in parentheses are the Costain errors.[40]

experimentally determined values. This is further evidence that the presented calculated structure is close enough to the experimental structure to be considered as a very suitable substitute.

5.3. DIPOLE FORBIDDEN/NUCLEAR ELECTRIC QUADRUPOLE COUPLING ALLOWED TRANSITIONS

The spectra contains multiple dipole forbidden transitions. These are transitions which have $\Delta J > 1$ or transitions where neither K_a nor K_c have a change in parity. An example of an observed transition is given in Figure 6. As mentioned in previous literature, these transitions arise from "large" off-diagonal nuclear quadrupole coupling tensor components when compared to rotational constants. The facilitator of the observed

trans forbidden transitions is completely due to x_{ab}. That is, the value of x_{ab} is large

enough in comparison to the rotational constants in the *trans* conformer in order to create

a mixing of allowed transition states to bring about a dipole-forbidden transition.
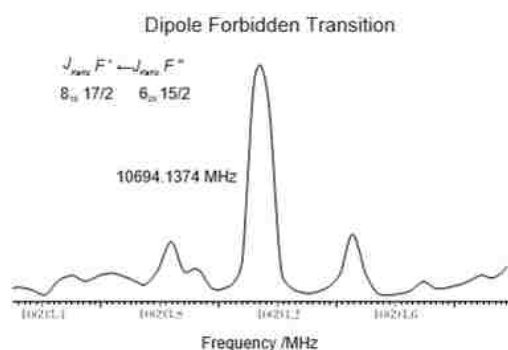
Figure 4. Example of an observed dipole forbidden transition at 10694.1374 MHZ.

This was investigated for the case of the transition observed in Figure 4, $J'_{KaKc} \leftarrow$

$J''_{KaKc}, F' \leftarrow F'' = 8_{18} \leftarrow 6_{25}, \frac{17}{2} \leftarrow \frac{15}{2}$ which occurs at 10694.1374 MHz. A flag can be

enacted in SPFIT/SPCAT that will create a file with the extension .egy. Within the .egy

file, the quantum states with their calculated energy levels are presented along with a

mixing coefficient that can be associated with the "purity" of the state. The further this

value is from unity, the more the state is mixed. It is found that the $6_{25}, \frac{15}{2}$ level has a

mixing coefficient of 0.897 while the $8_{18}, \frac{17}{2}$ level is near unity, indicating the $6_{25}, \frac{15}{2}$

level is the one that is mixing. Upon inspection of the file, there is a state within 30 MHz

of the $6_{25}, \frac{15}{2}$ level with the quantum numbers $7_{07}, \frac{15}{2}$ also with a mixing coefficient of

0.897. When the assigned transitions are looked at, there is an allowed, observed

transition with $J'_{KaKc} \leftarrow J''_{KaKc}, F' \leftarrow F'' = 8_{18} \leftarrow 7_{07}, \frac{17}{2} \leftarrow \frac{15}{2}$ at 10717.7769 MHz,

approximately 23 MHz higher in energy, indicating this is the forbidden transition

pathway. This is unique because this would mean that this forbidden transition is brought

about by a *x*-type change in parity which, to the authors knowledge, has never been

indicated as a mechanistic pathway in the literature. However, there is no evidence

suggesting there is another pathway for the transition to be brought about as the $7_{07}, \frac{15}{2}$

energy level is the only state near the energy of the $6_{25}, \frac{15}{2}$ with a coefficient indicating

mixing, so this must be the formal pathway and the two states must be so close in energy

that they are essentially degenerate. This *x*-type linkage could prove to be a powerful tool

in understanding the necessity of the dipole moment in creating and tuning forbidden

transitions in the future, but this area is unexplored and would need more investigation.

5.4. CONCLUSIONS

The microwave spectrum of *trans*-3-bromo-1,1,1,2,2-pentafluoropropane has

been observed and analyzed for the first time using CP-FTMW spectroscopy. Two

isotopologues, ^{79}Br and ^{81}Br have been observed, assigned, and reported. The spectrum is

quite dense and near the continuum limit with an estimated density of approximately 1

transition/MHz with 1 transition/4 MHz representing the *trans* conformer alone. The

spectra are predominantly *b*-type due to the large predicted *b* dipole moment vector

component. The spectra were assigned using a combination of sophisticated theoretical

and assignment approaches which are greatly needed in order to find any patterns in the

spectra and small differences can lead to an unsuccessful assignment like what is found

with the current state of the *gauche* conformer.

Analysis of the spectrum indicates that the experimental structure is very close to that of the calculated structure as expected since so much care was taken to ensure a suitable starting geometry for assignment, but that this conclusion can be aided with the spectroscopic constants determined even though a full substitution structure is not present. Furthermore, the large determined x_{ab} component for the *trans* conformer does generate forbidden transitions but, uniquely, it has produced the first such transition known to the authors of a *x*-type linkage in the forbidden transition pathway due to a very near-degeneracy which could lead to future study of the necessity of the electric dipole moment with respect to the energy differences.

ACKNOWLEDGEMENTS

REFERENCES

1.   A. Javan, Phys. Rev. **107**, 1579 (1957).

2.   T. Oka, J. Chem. Phys. **45**, 752 (1966).

3.   H.M. Jemson, W. Lewis-Bevan, N. P. C. Westwood and M. C. L. Gerry, J. Mol. Spectrosc. **118**, 481 (1986).

4.   H. S. P. Müller and M. C. L. Gerry, J. Chem. Soc. Faraday Trans. **90**, 3473 (1994).

5.   L. Bizzocchi, C.D. Esposti and F. Tamassia, Chem. Phys. Lett. **293**, 441 (1998).

6.   L. Dore, C. Puzzarini, G. Cazzoli and A. Gambi, J. Mol. Spectrosc. **204**, 262 (2000).

7.   C.T. Dewberry, G. S. Grubbs II and S.A. Cooke, J. Mol. Spectrosc. **257**, 66 (2009).

8.   G. S. Grubbs II, W.C. Bailey and S.A. Cooke, Chem. Phys. Lett. **477**, 37 (2009).

9.   G. S. Grubbs II, W.C. Bailey and S.A. Cooke, Mol. Phys. **107**, 2221 (2009).

10.   G. S. Grubbs II and S.A. Cooke, J. Mol. Struct. **963**, 87 (2010).

11.   G. S. Grubbs II, G. Kadiwar, W.C. Bailey and S.A. Cooke, J. Chem. Phys. **132**, 024310 (2010).

12.   B.E. Long, G. S. Grubbs II, J.D. Langridge and S.A. Cooke, J. Mol. Struct. **1023**, 55 (2012).

13.   F.E. Marshall, D.J. Gillcrist, T.D. Persinger, S. Jaeger, C.C. Hurley, N.E. Shreve, N. Moon and G. S. Grubbs II, J. Mol. Spectrosc. **328**, 59 (2016).

14.   F.E. Marshall, J.L. Neill, M.T. Muckle, B.H. Pate, Z. Kisiel and G. S. Grubbs II, J. Mol. Spectrosc. **344**, 34 (2018).

15.   Z. Kisiel and J. Kosarzewski, Acta Phys. Pol. **131**, 311 (2017).

16.   M.J. Frisch, G.W. Trucks, H.B. Schlegel, G.E. Scuseria, M.A. Robb, J.R. Cheeseman, G. Scalmani, V. Barone, B. Mennucci, G.A. Petersson, H. Nakatsuji, M. Caricato, X. Li, H.P. Hratchian, A.F. Izmaylov, J. Bloino, G. Zheng, J.L. Sonnenberg, M. Hada, M. Ehara, R.F. K. Toyota, J. Hasegawa, M. Ishida, T. Nakajima, Y. Honda, O. Kitao, H. Nakai, T. Vreven, J. A. Montgomery, Jr., J.E. Peralta, F. Ogliaro, M. Bearpark, J.J. Heyd, K.N.K. E. Brothers, V.N. Staroverov, R. Kobayashi, J. Normand, K. Raghavachari, A. Rendell, J.C. Burant, S.S. Iyengar, J. Tomasi, M. Cossi, N. Rega, J.M. Millam, M. Klene, J.E. Knox, J.B. Cross, V. Bakken, C. Adamo, J. Jaramillo, R. Gomperts, R.E. Stratmann, O. Yazyev, A.J. Austin, R. Cammi, C. Pomelli, J.W. Ochterski, R.L. Martin, K. Morokuma, V.G. Zakrzewski, G.A. Voth, P. Salvador, J.J. Dannenberg, S. Dapprich, A.D. Daniels, O. Farkas, J.B. Foresman, J.V. Ortiz, J. Cioslowski and D.J. Fox, *Gaussian 09, Revision D.01* (Gaussian, Inc., 340 Quinnipiac Street, Building 40, Wallingford, CT, 06492, 2009; Copyright @ 1994-2009), Copyright @ 1994-2009.

17.   R. Weast, *CRC Handbook of Chemistry and Physics 67th Edition* (CRC Press, Inc., Boca Raton, FL, 1986), p. 1.

18.   P. Pyykkö, Mol. Phys. **106**, 1965 (2008).

19.   W.C. Bailey and F.M. Gonzalez, J. Mol. Struct. **651-653**, 689 (2002).

20.   A.D. Becke, J. Chem. Phys. **104**, 1040 (1996).

21.   C. Adamo and V. Barone, Chem. Phys. Lett. **274**, 242 (1977).

22.   A. Schäfer, J. Chem. Phys. **100**, 5829 (1994).

23.   D. Feller, J. Comput. Chem. **17**, 1571 (1996).

24.   K.L. Schuchardt, B.T. Didier, T. Elsethagen, L. Sun, V. Gurumoorthi, J. Chase, J. Li and T.L. Windus, J. Chem. Inf. Model. **47**, 1045 (2007).

25.   W.C. Bailey, Calculation of Nuclear Quadrupole Coupling Constants in Gaseous State Molecules **URL: http://web.mac.com/wcbailey/nqcc/** (2018).

26.   H.M. Pickett, J. Mol. Spectrosc. **148**, 371 (1991).

27.   Z. Kisiel, L. Pszczółkowski, I.R. Medvedev, M. Winnewisser, F.C.D. Lucia and C.E. Herbst, J. Mol. Spectrosc. **233**, 231 (2005).

28.   Z. Kisiel, PROSPE–Programs for Rotational SPEctroscopy **URL: http://info.ifpan.edu.pl/ kisiel/prospe.htm** (2018).

29.   Z. Kisiel, *Spectroscopy from Space* (Kluwer Academic Publishers, Dordrecht, 2001), p. 91.

30.   J. K. G. Watson, *Vibrational spectra and structure*, Vol. 6 (Elsevier, Amsterdam, 1977), p. 1.

31.   G.G. Brown, B.C. Dian, K.O. Douglass, S.M. Geyer, S.T. Shipman and B.H. Pate, Rev. Sci. Instrum. **79**, 053103 (2008).

32.   C.T. Dewberry, R.B. Mackenzie, S. Green and K.R. Leopold, Rev. Sci. Instrum. **86**, 065107 (2015).

33.   L. Evangelisti, K.J. Mayer, M.S. Holdren, T. Smart, C. West, B. Pate, G. Sedo, F.E. Marshall and G. S. Grubbs II, 72nd International Symposium on Molecular Spectroscopy at the University of Illinois-Urabana Champaign **Urbana, IL** (2017).

34.   D. Patterson, M. Schnell and J.M. Doyle, Nature **497**, 475 (2013).

35.   S. Lobsiger, C. Perez, L. Evangelisti, K.K. Lehmann and B.H. Pate, J. Phys Chem. Lett. **6**, 196 (2015).

36.   S. Grimme and M. Steinmetz, Phys. Chem. Chem. Phys. **15**, 16031 (2013).

37. F.E. Marshall, G. Sedo, C. West, B.H. Pate, S.A. Allpress, C.J. Evans, P.D. Godfrey, D. McNaughton and G. S. Grubbs II, J. Mol. Spectrosc. **342**, 109 (2017).

38. J. Kraitchman, Am. J. Phys. **21**, 17 (1953).

39. R.K. Bohn, J. A. Montgomery, Jr., H.H. Michels and J.A. Fournier, J. Mol. Spec. **325**, 42 (2016).

40. C.C. Costain, Trans. Am. Crystallogr. Assoc. **2**, 157 (1966).

41. W. Gordy, J.W. Simmons and A. Smith, Phys. Rev. **72**, 344 (1947).

42. J. Dubrulle, J. Burie, D. Boucher, F. Herelemont and J. Demaison, J. Mol. Spectrosc. **88**, 394 (1981).

43. C. Flanagan and L. Pierce, J. Chem. Phys. **38**, 2963 (1963).

44. R.S. Wagner, B.P. Dailey and N. Solimene, J. Chem. Phys. **26**, 1593 (1957).

45. R.H. Schwendeman and F.L. Tobiason, J. Chem. Phys. **43**, 201 (1965).

46. Y. Niide, I. Ohkoshi and M. Takano, J. Mol. Spectrosc. **89**, 3s87 (1981).

47. J. Kim, H. Jang, S. Ka, D.A. Obenchain, R.A. Peebles, S.A. Peebles and J.J. Oh, J. Mol. Spectrosc. **328**, 50 (2016).

48. A. Baldacci, P. Stoppa, A.P. Charmet, S. Giorgianni, G. Cazzoli, C. Puzzarini and R. Larsen, J. Phys. Chem. A **111**, 7090 (2007).

49. G. Cazzoli, L. Cludi, C. Puzzarini, P. Stoppa, A.P. Charmet, N. Tasinato, A. Baldacci, A. Baldan, S. Giorgianni, R.W. Larsen, S. Stopkowicz and J. Gauss, J. Phys. Chem. A **115**, 453 (2011).

50. A.P. Cox, G. Duxbury, J.A. Hardy and Y. Kawashima, J. Chem. Soc., Faraday Trans. 2 **76**, 339 (1980).

II. THE CP-FTMW SPECTRUM OF BROMOPERFLUOROACETONE

ABSTRACT

The microwave spectrum of bromoperfluoroacetone has been observed and reported for the first time on a newly constructed CP-FTMW spectrometer located at Missouri S&T operational in the 6-18 GHz region of the electromagnetic spectrum. Rotational constants, centrifugal distortion constants, and all components of the nuclear quadrupole coupling tensor were determined for both the 79 and 81 isotopologues of bromine and have been reported. The spectrum is densely populated with transitions and the need for the more accurate theory of W. C. Bailey was needed for adequate assignment of >2000 transitions. Included in the spectrum were dipole forbidden $\Delta J = 2$ and x-type transitions. Second moments and Kraitchman position of the bromine have been presented to help identify the experimental structure. Quadrupole coupling tensor analyses were carried out to show that the electric field gradient in bromine changes dramatically upon fluorination when compared to its chlorine counterpart. Also, this change represents an increase in the electric field gradient, suggesting more covalent C-Br bonding. Dipole forbidden transitions have been observed and found to be always linked through a dipole allowed transition, but are not necessarily linked through one singular off-diagonal term. Notably, a select few of the dipole forbidden transitions are facilitated through a third mixing state not previously found in the literature.

1. INTRODUCTION

Recent advancements in chirped-pulse Fourier transform microwave spectroscopy have changed the landscape of rotational spectroscopy [46]. Along with tackling problems of fundamental interest such as bonding, structure, and intermolecular interactions, CP-FTMW is now used to look at complex dynamics problems. The high resolution of the technique coupled with its correct intensity profiles make it a powerful tool for isolating individual species in a fraction of the time needed for narrowband cavity techniques. Different molecular sourcing techniques also allow for the analysis of spectra of a broad range of molecules under different environments (metal containing, room temperature, etc.) [66, 67, 68]. Double resonance [69] and 2-dimensional techniques [70] allow for the understanding of quantum level mixing, coupling, and dynamical structure [71].

Another advantage of CP-FTMW techniques is its ability to take very dense, complex spectra and ease the assignment process. Software packages and assignment routines have been compiled by typical users of this technique for the purposes of automating spectral assignment (AUTOFIT) [72], make assignment rules and pattern recognition algorithms for use in undergraduate teaching (SPECFITTER) [73], and fit spectra to effective Hamiltonians (AABS with SPFIT, PGOPHER, and JB95 and JB64) [74, 75, 76, 77]. These skills and programs have become a very useful addition for using rotational spectroscopy as a chemical analysis tool.

One place where CP-FTMW has been of particular use is in isolating and identifying dipole forbidden transitions [78, 79, 80, 81, 82]. Typically, these transitions

arise when molecules possess quadrupolar nuclei and the rotational constants are of similar value or smaller than the nuclear quadrupole coupling constants. In these transitions, an off-diagonal nuclear quadrupole coupling tensor component provides a way for energy states of different J quantum levels to be nearly degenerate and heavily mixed producing predicted and observed dipole-forbidden transitions.

Bromoperfluoroacetone is an optimal candidate to observe this effect. In addition to possessing predicted rotational constants and quadrupole coupling values with similar size values, predictions show that bromoperfluoroacetone should possess all three experimentally determinable off-diagonal nuclear quadrupole coupling tensor components [83, 84]. The spectra should be dense, having roughly equal [79]Br and [81]Br components, and present many opportunities to observe these types of transitions. Also, previous experimental observations of fluorinated haloacetones have resulted in the observation of one conformation of the molecule in a molecular beam [85, 86, 87, 88]. For all of these reasons, it was important to see how bromoperfluoroacetone compares with other halofluorocarbons and halogenated perfluoroacetones.

The design and function of a new CP-FTMW spectrometer functional in the 6-18 GHz region of the electromagnetic spectrum is presented in this work. This instrument has been implemented on the molecule, bromoperfluoroacetone, and the pure rotational spectrum for this species has been measured and reported for the first time leading to the first structure determination of the molecular beam species. Spectral features such as dipole forbidden transitions have been observed and are discussed. Quantum chemical calculations for bromoperfluoroacetone have been performed and are compared to other literature values.

2. QUANTUM CHEMICAL CALCULATIONS

Geometry optimizations were performed with the Gaussian03 program [89] at the MP2/6-311++G level of theory [90, 91, 92, 93] using the full electron contribution. The resulting equilibrium structure is presented in Figure 1 and the quantitative structural parameters are presented in Table 1. The calculated structure predicts dipole moments of 1.39, 1.14, and 0.34 D along the *a*-, *b*-, and *c*-axes, respectively.
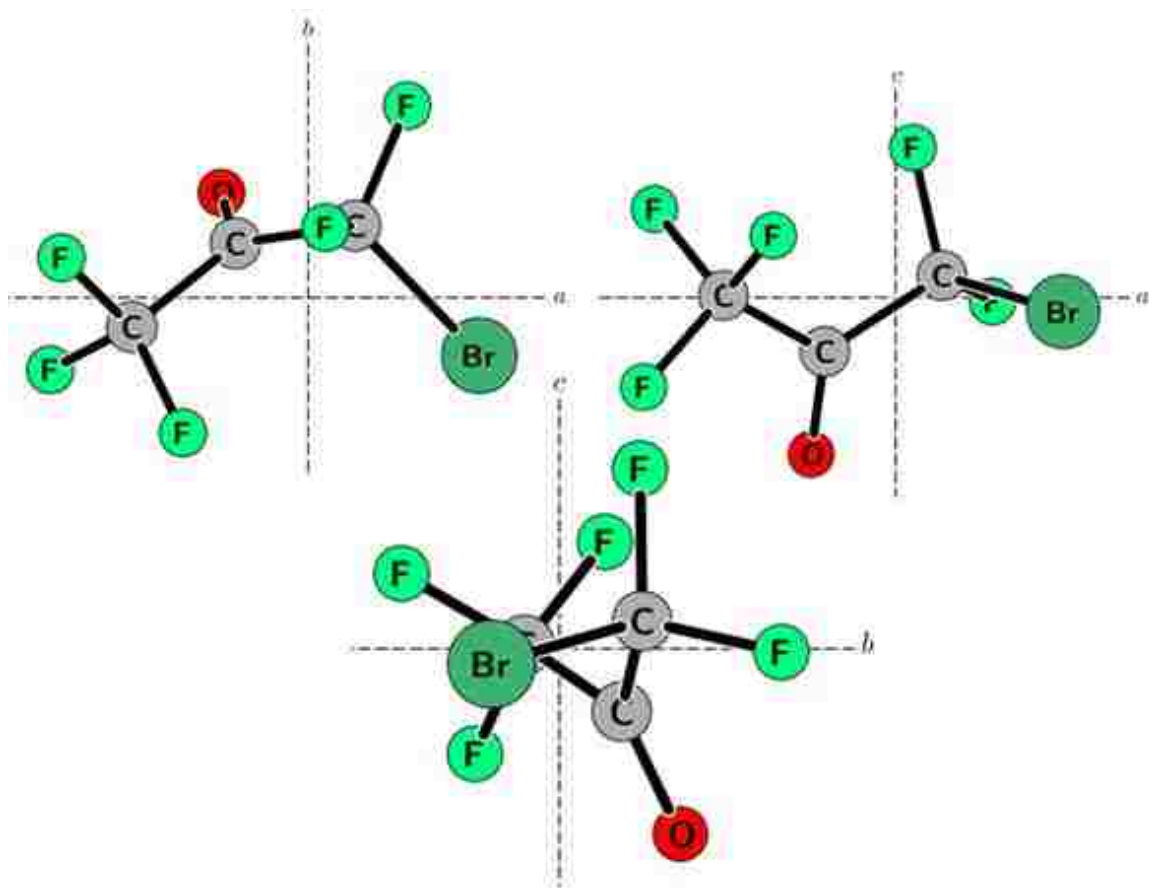
Figure 1. The calculated (see text for details) structure of bromoperfluoroacetone in the *ab-, ac-,* and *bc-* planes.

Table 1. Quantum chemical calculations values for $CF_3COC^{79}BrF_2$ compared to Bailey's r_e values.

Parameter	This Work[a]	Bailey[19][b]
A / MHz	1449.9	1524.5
B / MHz	632.9	659.6
C / MHz	591.0	614.7
χ_{aa} / MHz	369.8	123.13
χ_{bb} / MHz	-58.2	155.61
χ_{cc} / MHz	-311.6	-278.74
χ_{ab} / MHz	-427.7	434.12
χ_{ac} / MHz	-60.7	94.88
χ_{bc} / MHz	41.8	121.37
$|\mu_a|$ /D	1.39	—
$|\mu_b|$ /D	1.14	—
$|\mu_c|$ /D	0.34	—

[a] Optimized using full electron contribution at the MP2/6-311++G level of theory.

[b] Geometry optimization performed at the MP2/6-311+G(3df,3pd) level of theory with empirically corrected bond lengths. Nuclear quadrupole coupling calculations performed using Bailey's B1LYP/TZV(3df,3p) model for bromine

W. C. Bailey reports a similar r_e structure in reference [83], also presented in Table 1 for comparison. Since these calculations are performed slightly differently than a generic geometry optimization with energy calculation, references [83] and [94] detail the processes W. C. Bailey uses to arrive at the geometric structures and nuclear quadrupole coupling tensor values.

Structurally, bromoperfluoroacetone is predicted to be "twisted" to engulf the *a*-axis resulting in a calculated C_1-C_2-C_3-Br dihedral angle of 89.3°. The fluorines and bromine are staggered while the oxygen and bromine are oriented in different directions. This structure has no atom purely lying in any one principal axis plane. This is especially important with the bromine atom as both naturally abundant isotopes of bromine possess a quadrupolar ($I \geq 1$) nucleus providing all three off-diagonal components of the nuclear quadrupole coupling tensor. All calculated quadrupole coupling tensor components are also presented in Table 1 for both the structure calculated in this work and W. C. Bailey's structure.

3. EXPERIMENT

3.1. CP-FTMW SPECTROMETER

Spectral acquisitions were performed at the Missouri University of Science and Technology on a newly constructed chirped pulse Fourier transform microwave (CP-FTMW) spectrometer. A schematic of this instrument can be found in Figure 2. This instrument is based on a combination of the previous instruments described by Pate [46], Cooke [66, 95], and Peebles [96] while implementing technological advances made in the radiofrequency/microwave (RF/MW) electronics industry, specifically those of the company Tektronix. The signals are directly digitized to maximize signal-to-noise capability of the instrument while also reducing the number of components needed, simplifying the circuit.
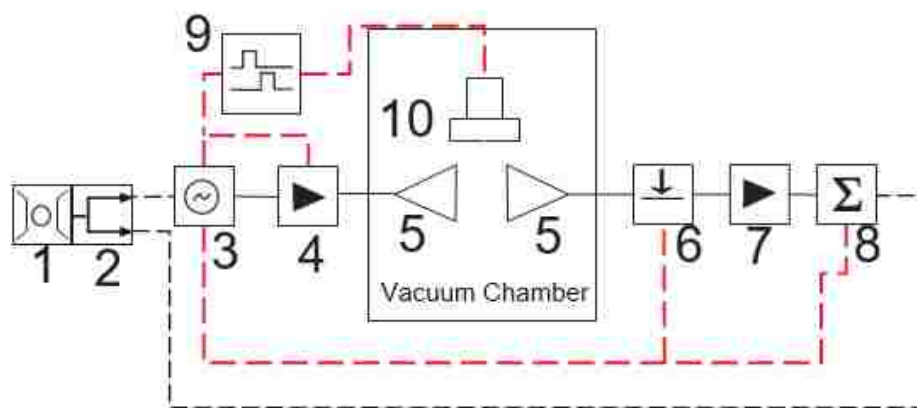
Figure 2. Schematic diagram of the CP-FTMW circuit and experiment. The 10 MHz reference signal is denoted by a gray, dotted line while timing markers are denoted by red, dashed lines. The components of the circuit are: 1 and 2. Stanford Research Systems 5 and 10 MHz Rubidium Standard Clock (Only 10 MHz used) with distribution amplifier; 3. Tektronix Arbitrary Waveform Generator Model AWG70001A (50 GS/s, 20 GHz bandwidth); 4. Microsemi 6-18 GHz High Gain Ridged Horn Antennae, Model QWH-SL-2-18-S-HG-R; 6. ATM 0.5-18 GHz SPST Pin Diode Switch Model S1517D; 7. Miteq 1-18 GHz Low Noise Amplifier (55dB minimum gain, 2.2 dB Noise Figure), Model AMF-7D-01001800-22-10P; 8. Tektronix Digital Phosphorus Oscilloscope (4-channel, 100 GS/s, 23 GHz Bandwidth), Model DPO72304DX; 9. Quantum Composers 4-channel Pulse Delay Generator, Model 9514+T; 10. Parker Hannifin Series 9 Valve with Iota One Drive.

The CP-FTMW spectrometer is currently operational from 6-18 GHz, but can be expanded to 2-18 GHz with the substitution of a power amplifier that is currently unavailable. For phase coherence amongst the instrumentation, the experiment is held to a 10 MHz frequency standard produced by Stanford Research Systems. The experiment begins on a Tektronix Arbitrary Waveform Generator Model AWG70001A (AWG). This instrument has a 50 GS/s digitization rate and 20 GHz bandwidth with some dropoff in microwave intensity after 15 GHz. Using a MatLab code written in-house, the AWG is able to create linear frequency sweeps of DC-20 GHz in under 1 μs, negating the need for a microwave synthesizer and/or mix up stage in the circuit. The clock used for the AWG

is very stable and allows the AWG to also be the master clocking device of the experiment, eliminating any phase-locked oscillators needed for experimental timing purposes. The experiment begins by creating a linear frequency sweep in any desired range from 6-18 GHz for 100 ns to 6 μs. Although timings and lengths are variable, for monomer species of significant concentration ($\geq$ 0.1 %) in a gas mix with significant dipole moments ($\geq$ 0.5 D), it is usually most efficient and effective to use 6 GHz regions with 4 μs pulse durations. The linear frequency sweep, known as a "chirp", is then power amplified by a TTL-controlled, 40 W Microsemi solid state amplifier operational in the 6-18 GHz range. The signal then enters a vacuum chamber held at 10^{-9} atm using a Varian VHS-10 diffusion pump backed by an Edwards 40 rotary pump.

After entering the chamber, the signal is broadcast onto a gas mixture using the first of two Qpar 2-18 GHz high gain, ridged horn attennae. A TTL-controlled, single pole, single throw switch from ATM behind the second antennae protects the rest of the circuit from power overloads due to the 40 W amplifier. Immediately after the molecules and microwaves interact, a molecular signal in the form of a free induction decay (FID) is collected, amplified by a high gain, low noise amplifier by Miteq, and directly digitized in the time domain on a Tektronix 100 GS/s, 23 GHz bandwidth oscilloscope, model DPO72304DX. The FID signals are then saved to an external hard drive where they are taken to a separate computer, added together coherently, and fast Fourier transformed (FFT) into the frequency domain utilizing code written by Stephen Cooke [97]. We have observed that averaging collected spectral acquisitions in this way instead of simply averaging the FIDs or FFTs of individual runs without manipulation, lowers total time of an experiment by not requiring the scope to perform the FFT as well as increases our

signal-to-noise on observed transitions by as much as a factor of 10! This setup may also utilize the Tektronix FastFrame software to do multiple FID collections allowing for even faster experimental acquisition speeds and minimalizing sample consumption. The entire setup is initiated, controlled and manipulated through a separate computer located in the vicinity of the machine running LabView software codes written in-house.

The gas mixture consists of the sample of interest in low concentration with a carrier gas (usually Ar). This mixture is introduced into the experiment via a Parker-Hannifin Series 9 solenoid valve with 0.8 mm orifice and undergoes a supersonic expansion to rotationally cool the sample to temperatures < 10 K. This technique has three main advantages: (i) after a small distance (~10 nozzle diameters) from the nozzle exit, the molecules are collision free and, therefore increase instrument resolution, (ii) provides greater molecular populations in the rotational states most accessible by the excitation frequencies provided by experiment, and (iii) simplifies spectral assignment because population distributions are minimal and, typically, only the lowest energy molecular conformations are allowed. This sampling mechanism, as mentioned earlier, has been coupled with a laser ablation, discharge, or laser ablation/discharge sources. The authors have recently constructed a laser ablation source to add to this setup themselves and have the ability to do crossed molecular beam experiments for possible dynamics investigations.

All timings in the experiment are ultimately controlled by the AWG. However, all components cannot be controlled at the same time on the AWG due to both a lack of physical markers and changing timings *in situ* for this instrument is nearly impossible as it involves creating, updating, and changing the sequencing codes in MatLab and the

AWG on the fly. This involves a large amount of data processing all while the experiment is still being executed, bogging down the experiment and creating a lag. To account for this problem, a Quantum Composers Model 9514+-T Pulse Delay Generator has been implemented. This instrument is referenced to the same 10 MHz signal that the AWG and oscilloscope are referenced and controls the firing time and length for a Parker-Hannifin Series 9 solenoid valve controlled by an Parker-Hannifin Iota One. The AWG sequence only provides the initial signal to operate the delay generator and synchronize the experiment.

3.2. BROMOPERFLUOROACETONE EXPERIMENTAL DETAILS

97% bromoperfluoroacetone was purchased from Synquest Laboratories and used without further purification. The sample was place in a ``U''-shaped tube submerged in an ice water bath where approximately 0.5-1 atm of argon was allowed to pass over the liquid sample approximately 60 cm upstream of the nozzle. Molecules undergoing the expansion were cooled to a rotational temperature of ~2 K as determined from the intensity profile of the spectra and the quantum chemically calculated dipole moments (see above in *Quantum Chemical Calculations* section). As mentioned earlier, the entire 6-18 GHz region can be done in one acquisition, but it was necessary for these experiments to use two 6 GHz acquisition windows to maintain sufficient powering to polarize the molecules. For simplicity purposes, the multi-FID setup was not used so the valve was pulsed at 1 Hz and one FID of 16 μs was collected per nozzle pulse. 30,000 FIDs were collected, averaged, and Fourier transformed. A picture of the resultant spectra from 6-12 GHz is shown in Figure 3. Transitions were attributed an uncertainty of 10

kHz for singular line profiles with 50 or 75 kHz attributed to blends in accordance with

the effect the blend had on changing the usual linewidths. The linewidths for observed

single transitions were 65 kHz.
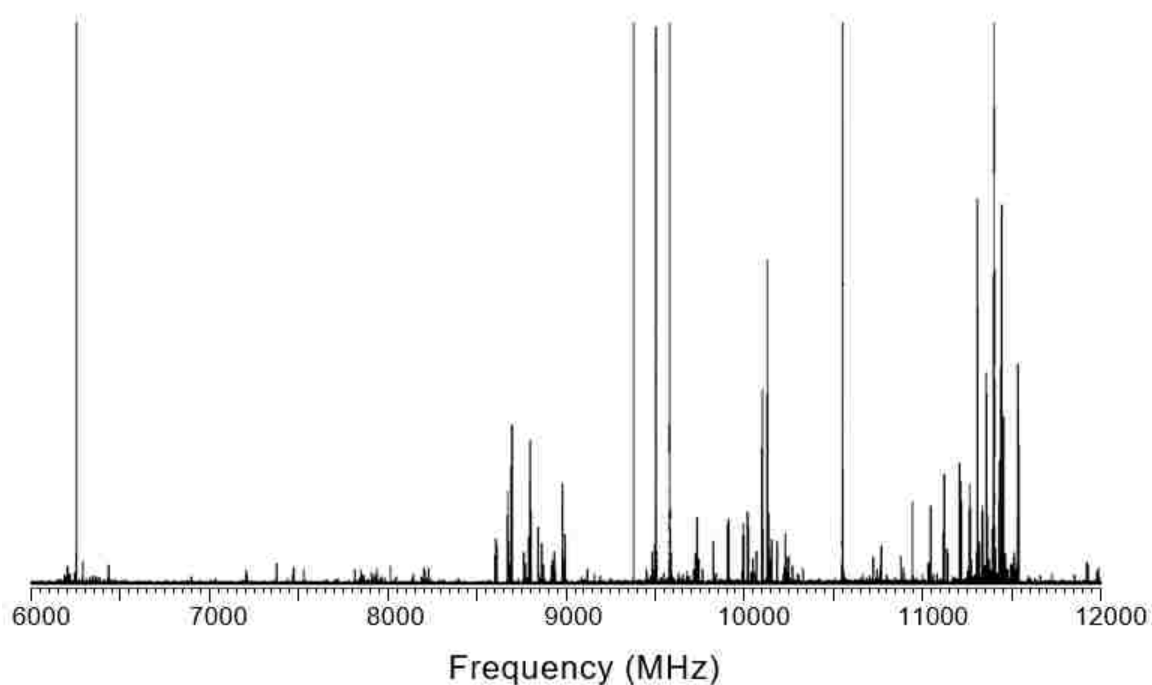
Figure 3. Spectrum of bromoperfluoroacetone from 6-12 GHz.

4. RESULTS AND ANALYSIS

As shown in Figure 3, the spectra were dense. This made assigning transitions

very difficult with the traditional method of using line lists and trying to use the

calculated spectra to understand transition orders and separations. Instead, a graphical

prediction of the spectrum taking into account rotational temperature was needed in order

to take advantage of the correct intensities provided by the technique [66]. For this the

AABS program suite produced by Zbigniew Kisiel [75, 43] was used in conjunction with

Pickett's SPFIT and SPCAT program suite [74]. With this, the authors were able to input

a prediction for the dipole moments, rotational partition coefficient using the rotational

constants, a predicted temperature of the beam using previous experience with similar

molecules in Ar expansions, and visually interpret the spectra using known asymmetric

pattern recognition techniques [73]. Rotational temperatures were adjusted until the

predicted spectra had a similar intensity profile to the experimental intensity profile.

Using this method, however, it became immediately apparent that the calculated

spectroscopic parameters found in this work were not adequate to make appropriate

assignment due to significant splitting from the quadrupole coupling nuclei and similar

intensities for both naturally occurring isotopes of the bromine atom as well as the

density of the experimental spectrum. W. C. Bailey's reported spectroscopic parameters

for bromoperfluoroacetone [83] from Table 1 were input into the program and this

prediction provided the significant improvement needed to move forward with a proper

assignment.

As previously mentioned, spectra were assigned and fit using Pickett's

SPFIT/SPCAT suite of programs [74]. Assignments were made in the I^r representation

and fits were done using a Watson S-reduced Hamiltonian [98]. Spectroscopic parameters

can be found in Table 2. Rotational constants, quartic and sextic centrifugal distortion

constants, and all six quadrupole coupling tensor components were determined for both

isotopologues. The uncertainty of the fits for were 25 and 22.7 kHz for $CF_3COC^{79}BrF_2$

and $CF_3COC^{81}BrF_2$, respectively, in good agreement with the attributed uncertainties

reported in the *Experimental* section. Having determined all three off-diagonal

components of the quadrupole coupling tensor, signs have been reported for each isotopologue. However, differences in the sign of individual off-diagonal quadrupole coupling tensor components between isotopologues can be ignored because the overall off-diagonal sign parity is the same (+) between isotopologues, showing consistency in the fits [99].

Table 2. Spectroscopic parameters of Bromoperfluoroacetone.

Parameter	$CF_3COC^{79}BrF_2$	$CF_3COC^{81}BrF_2$
A / MHz	1516.9240(6)[a]	1513.2513(5)
B / MHz	655.5786(2)	650.2747(2)
C / MHz	609.3570(2)	604.2341(2)
D_J / kHz	0.070(1)	0.066(2)
D_{JK} / kHz	-0.266(5)	-0.261(1)
D_K / kHz	0.64(1)	0.72(1)
d_1 / kHz	-0.0195(3)	-0.0199(1)
d_2 / kHz	-0.00175(7)	-0.00141(7)
H_J / Hz	-0.007(3)	-0.017(5)
H_{JK} / Hz	-0.03(1)	—
H_{KJ} / Hz	0.08(4)	—
H_K / Hz	0.7(1)	3.3(1)
h_3 / Hz	0.0009(2)	—-
χ_{aa} / MHz	105.98(2)	92.33(3)
χ_{bb} / MHz	164.28(2)	134.17(2)
χ_{cc} / MHz	-270.26(2)	-226.51(2)
χ_{ab} / MHz	427.5(4)	359.5(3)
χ_{ac} / MHz	-109(1)	82(1)
χ_{bc} / MHz	-125.2(1)	102.8(1)
N[b]	1068	916
Microwave RMS[c] / kHz	25.0	22.7

[a] Numbers in parentheses give standard errors (1σ, 67% confidence level) in units of the least significant figure.

[b] Number of observed transitions used in the fit

[c] Microwave RMS is defined as $\sqrt{\dfrac{(obs-calc)^2}{N}}$

Inspection of Table 2 shows the significant agreement between the experimentally determined constants and the predicted spectroscopic parameters of Bailey's work. Between the ^{79}Br and ^{81}Br isotopes, 1984 transitions were assigned in the 6-18 GHz region of the electromagnetic spectrum, 1068 for $CF_3COC^{79}BrF_2$ and 916 for $CF_3COC^{81}BrF_2$, giving a spectral density of approximately one assigned transition every 6 MHz. A representation of the densitiy of this spectra and proximity of the two isotopologues is found in Figure 4. The assigned transitions consisted of R-branch, *a*-, *b*-, and *c*-type and Q-branch **b**-type dipole allowed transitions for both isotopologues as well as observed *x*-type and $\Delta J = 2$ dipole forbidden transitions. A comprehensive listing of the assigned transitions for each isotopologue can be found in the Supplemental Data while a listing of all observed dipole forbidden transitions are in Table 3. Although it was expected given the signal-to-noise of the parent isotopologues that transitions for ^{13}C species should be present in the spectra in natural abundance, there wasn't an adequate sampling of transitions that could be detected for proper assignment and have been left out of this work. Furthermore, the discrepancy between the number of measured ^{79}Br transitions and the number of ^{81}Br transitions comes from a region of the spectra just below 8 GHz where, unknown to the authors, approximately 100 ^{81}Br transitions were predicted to be of significant intensity, but not observed in the spectrum.
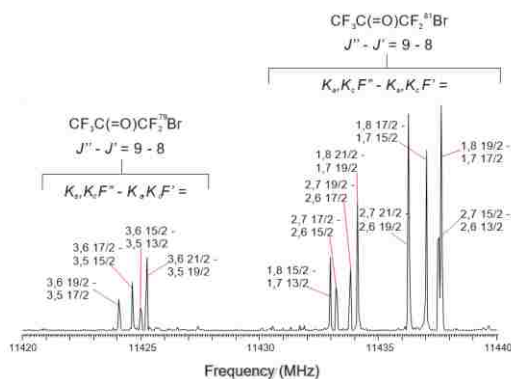
Figure 4. A sampling of the J"-J' = 9 – 8 transitions for both [79]Br and [81]Br from 11420-11440 MHz.

Table 3. Assigned dipole forbidden transitions.

Molecule	Transition Quantum Numbers $J^{\dagger}_{K_a,K_c}, F' - J^{\dagger\dagger}_{K_a,K_c}, F^{\dagger\dagger}$	Frequency / MHz
CF$_3$COC^{79}BrF$_2$	$10_{5,5}, \frac{19}{2} - 9_{5,5}, \frac{17}{2}$	12668.525
	$11_{5,6}, \frac{25}{2} - 10_{5,6}, \frac{23}{2}$	13923.535
	$11_{5,6}, \frac{21}{2} - 10_{5,6}, \frac{19}{2}$	13926.306
	$11_{5,7}, \frac{21}{2} - 10_{5,5}, \frac{19}{2}$	13932.412
	$11_{5,6}, \frac{23}{2} - 10_{5,6}, \frac{21}{2}$	13934.986
	$11_{5,7}, \frac{23}{2} - 10_{5,5}, \frac{21}{2}$	13934.986
	$12_{6,6}, \frac{27}{2} - 11_{6,6}, \frac{25}{2}$	15196.598
	$12_{6,6}, \frac{23}{2} - 11_{6,6}, \frac{21}{2}$	15199.030
	$12_{6,7}, \frac{23}{2} - 11_{6,5}, \frac{21}{2}$	15199.030
	$13_{6,8}, \frac{29}{2} - 12_{6,6}, \frac{27}{2}$	16463.458
	$13_{6,8}, \frac{25}{2} - 12_{6,6}, \frac{23}{2}$	16465.119
CF$_3$COC^{81}BrF$_2$	$5_{3,2}, \frac{13}{2} - 4_{3,2}, \frac{11}{2}$	6281.938
	$5_{3,3}, \frac{9}{2} - 4_{3,1}, \frac{7}{2}$	6282.303
	$5_{3,2}, \frac{9}{2} - 4_{3,2}, \frac{7}{2}$	6285.944
	$6_{3,4}, \frac{11}{2} - 5_{3,2}, \frac{9}{2}$	7532.974
	$7_{4,3}, \frac{11}{2} - 6_{4,3}, \frac{13}{2}$	8788.679
	$7_{4,4}, \frac{11}{2} - 6_{4,2}, \frac{13}{2}$	8788.982
	$7_{4,4}, \frac{13}{2} - 6_{4,2}, \frac{11}{2}$	8793.972
	$8_{4,5}, \frac{13}{2} - 7_{4,3}, \frac{11}{2}$	10046.178
	$8_{4,4}, \frac{13}{2} - 7_{4,4}, \frac{11}{2}$	10046.319
	$8_{4,4}, \frac{13}{2} - 7_{4,4}, \frac{13}{2}$	10049.130

Table 3. Assigned dipole forbidden transitions (cont.).

Molecule	Transition Quantum Numbers $J'_{K_a,K_c}, F' - J''_{K_a,K_c}, F''$	Frequency / MHz
$CF_3COC^{81}BrF_2$	$8_{4,5}, \frac{15}{2} - 7_{4,3}, \frac{13}{2}$	10049.130
	$11_{5,6}, \frac{25}{2} - 10_{5,6}, \frac{23}{2}$	13816.691
	$11_{5,7}, \frac{25}{2} - 10_{5,5}, \frac{23}{2}$	13817.146
	$11_{5,6}, \frac{21}{2} - 10_{5,6}, \frac{19}{2}$	13818.417
	$11_{5,7}, \frac{21}{2} - 10_{5,5}, \frac{19}{2}$	13818.962
	$13_{6,8}, \frac{25}{2} - 12_{6,6}, \frac{23}{2}$	16320.428
	$13_{6,7}, \frac{29}{2} - 12_{6,7}, \frac{27}{2}$	16343.929
	$14_{4,10}, \frac{25}{2} - 12_{6,6}, \frac{23}{2}$	16358.369
	$14_{4,10}, \frac{25}{2} - 12_{6,7}, \frac{23}{2}$	16358.369
	$14_{6,9}, \frac{27}{2} - 13_{6,7}, \frac{25}{2}$	17581.287

5. DISCUSSION

5.1. STRUCTURE

As mentioned previously, Figure 1 shows the calculated equilibrium structure of the molecule. In this structure, the C_1-C_2-C_3-Br backbone is ``twisted" to engulf the *a*-axis resulting in a dihedral angle of 89.3°. This twisting is a product of a staggered arrangement of the fluorine, oxygen, and bromine atoms in the molecule. The significant agreement between the quantum chemical rotational constants of both this work and Bailey [83] with the experimental constants determined suggest that this structure is accurate. However, because no C-13 isotopic substitution spectra were obtained in this work, we cannot isolate experimental carbon positions to get a C-C-C-Br backbone. The excellent agreement of our Kraitchman bromine position with the calculated structures' in Table 4 also gives large validity to the structure.

Table 4. Kraitchman coordinates of bromine compared to quantum chemical calculations.

Axial Coordinate	Kraitchman[a]	Quantum Chemical Calculations	Bailey Calculations[19]
a / Å	1.7756(9)[b]	1.814	1.776
b / Å	-0.630(2)	-0.620	-0.624
c / Å	-0.13(1)	-0.15	-0.13

[a] Negative values signify sign has been changed to reflect the quantum chemical calculation coordinate sign as Kraitchman coordinates only give absolute values

[b] Numbers in parentheses give Costain errors in units of least significant figure

Table 5. Experimental second moments and nuclear quadrupole coupling parameters derived from fitted spectroscopic parameters.

Parameter	$CF_3COC^{79}BrF_2$	$CF_3COC^{81}BrF_2$
P_{aa} /uÅ^2	633.5470(2)[a]	639.8024(2)
P_{bb} /uÅ^2	195.8174(2)	196.5937(2)
P_{cc} /uÅ^2	137.3430(2)	137.3753(2)
Δ / uÅ^{2,b}	-274.6860(4)	-274.7507(4)
κ^c	-0.8981	-0.8987
χ_{zz} / MHz	595.4(5)	497.0(4)
χ_{xx} / MHz	-290.5(7)	-237.7(8)
χ_{yy} / MHz	-304.9(4)	-259.4(6)
θ_{za}	47.969(4)	47.672(3)
η^d	0.0241(1)	0.0437(2)

a Numbers in parentheses give standard errors (1σ, 67% confidence level) in units of the least significant figure.

b Inertial defect. $\Delta = I_c - I_a - I_b$

c Ray's asymmetry parameter: $\frac{2B-A-C}{A-C}$

d η is a measure of cylindrical symmetry: $\frac{x_{xx}-x_{yy}}{x_{zz}}$

Empirically, using second moments and comparing our Kraitchman bromine

position [100] we can make some conclusions about the overall structure of the molecule

[101,102]. For this we will reference Tables 4 and 5. The second moment value of

interest here is P_{cc} at 137.3430(2) $\mu Å^2$ for the ^{79}Br species. P_{cc} is given by the equation

[101, 102]:

$$P_{cc} = \sum m_i c_i^2 \tag{1}$$

where i is the atom in question, m is the mass in amu, and c is the value of the c-

coordinate of the ith atom in Å. Using the mass reported in Ref. [103] for Bromine-79,

this contribution to P_{cc}, therefore, is 1.3337 $\mu Å^2$. Subtracting this P_{cc} value from the total,

then, leaves the remaining contributions from the other atoms in the molecule to be

136.0093 $\mu Å^2$. According to Ref. [103], -CF$_2$ and –CF$_3$ group contributions with the

central carbon atom adding in (or near) the ab plane contribute approximately 45 $\mu Å^2$.

Making this assumption, we arrive at a contribution of 46 $\mu Å^2$ for the carbonyl group. If

we assume a C-C-C bond angle of 109.5° and typical C-C and C-O bond lengths of 1.6 Å

and 1.3 Å, respectively, the P_{cc} value contribution can range from 0 to ~80 $\mu Å^2$ for the

carbonyl group. In order to arrive at 46 $\mu Å^2$, the carbonyl must be tilted approximately

35° off the c-axis with these measurements. This is in good agreement with the presented

equilibrium structure in Figure 1.

5.2. QUADRUPOLE COUPLING COMPONENTS AND THE ELECTRIC FIELD GRADIENT

Because bromine also possesses a quadrupolar nucleus, it is useful to also

understand what is happening with the electric field gradient at the nucleus, particularly

along the C-Br bond as that will give an indication of the electron sharing (i.e. covalency)

amongst the atoms. This, in turn, is a direct indicator of bond strength. To do this,

QDIAG from the PROSPE website [43] was used to diagonalize the tensor into its x_{xx},

x_{yy}, and x_{zz} components. The results for both isotopologues are found in Table 5 along with the θ_{za} and asymmetry parameter, $\eta = \frac{x_{xx} - x_{yy}}{x_{zz}}$ values. η is a measure of cylindrical symmetry of the bond.

Using the calculated position of carbon from reference [83], the C-Br bond is 49.3° from the a-axis. From Table 5, the z-axis in bromoperfluoroacetone is shown to lie very close to the C-Br bond (within 1.5°). Therefore, for comparisons we will assume the z-axis lies along the bond. In this case, the π-character, π_c of the bromine bond may be calculated from the asymmetry in the coupling. This can be achieved if we assume that one axis orthogonal to the bond has zero π_c. Making this assumption gives [102]:

$$\pi_c = (\frac{2x_{zz}}{3eQq_{410}})\eta \tag{2}$$

where eQq_{410} is -769.76 MHz for the ^{79}Br atom [102]. For bromoperfluoroacetone, the π_c is 0.012, where only the absolute value has been given. This is significant compared to that found for iodine in 1-iodoperfluoropropane ($\pi_c = 0.0063$) [78], but still negligibly small.

Diagonalizing the nuclear quadrupole coupling tensor also allows for comparisons of x_{zz} amongst similar brominated molecules. This has been done in Table 6. Because the value of the nuclear quadrupole moment, Q, for ^{79}Br is quite large, 313(3) mb [104], the value of x_{zz} is quite sensitive to small changes in the electric field gradient along the z-axis, making comparisons strictly of value somewhat difficult. In order to make a more apt comparison, the electric field gradient, q_{zz}, has been calculated for each molecule chosen using Equation 3 [105]. These values are reported in Table 6. If we assume that the z-axis and the C-Br bond are aligned or very close in these molecules, some conclusions can be drawn on the effect of the C-Br bond by perfluorination in the series.

The first conclusion that can be made is that fluorination greatly increases the electric field gradient in the C-Br bonding by almost 1×10^{22} Vm^{-2}. Assuming a Townes-Dailey interpretation [106] of this, then the bond can be interpreted to be stronger in molecules where fluorine atoms are present. This is probably due to fluorines withdrawing more electron density in their respective bonds than hydrogens meaning the bromine must share more electron density with the carbon for which it is attached to make up for this decrease, increasing the covalency of the bond. Bromoperfluoroacetone, a perfluorinated molecule with an oxygen on the middle carbon, however, does not exhibit as large of an increase as the other molecule's in the table. This may be either due to the hybridization of the carbon atom on the central carbon slightly playing a role on the field gradient or the oxygen's ability to diminish the effect of the electron withdrawing ability of the fluorine atoms in the system, slightly breaking up the continuity in the molecule. Experimental values with different acetone or acetone derivatives containing a bromine would help to establish this trend, however, this information could not be found in the literature by the authors, suggesting future studies.

$$q_{zz}(\text{in V m}^{-2}) = \frac{x_{zz}(\text{in MHz}) * 4.135667663 \times 10^{22}}{Q \ (\text{in mb})} \tag{3}$$

Although bromine-containing acetone derivatives have not been studied, previous studies on chlorinated acetone derivatives have been provided by Cooke and coworkers [85, 86]. x_{zz} values for these molecules have been reported in Table 7 and, since the quadrupolar nuclei amongst the family are now different, electric field gradients were also calculated using Equation 3 and are also reported in the table for direct comparisons amongst the group. The results are quite interesting. Although there was a considerable difference in the electric field gradient when perfluorinating the bromine molecules, the chlorinated

acetone derivatives exhibit very little change between the hydrogenated and fluorinated species as indicated by the small range of $<0.5 \times 10^{22}$ Vm^{-2} amongst the group. Furthermore, all of the chlorinated acetone derivatives possess about half the magnitude of the electric field gradient of the brominated acetone, suggesting a much larger electron sharing in the C-Br bond than in the C-Cl bond. This is further evidence that more studies need to be done on the brominated acetone derivatives to get a clearer picture of what is happening in the electronic and geometric structure of this bond upon fluorination. Work has been started to determine these structural effects.

Table 6. x_{zz} and electric field gradient comparisons for a series of similar bromine molecules.

Molecule	χ_{zz} / MHz	q_{zz} / 10^{22} V m$^{-2,a}$	Reference
1-bromopropane	526.(4) [b]	6.95(9)	[47]
2-bromopropane	514.2(5)	6.79(7)	[48]
Bromofluoroacetonitrile	612.22(6)	8.09(8)	[49]
Bromodifluoroacetonitrile	619.65(6)	8.19(8)	[50]
Bromoperfluoroethane	611.46(6)	8.08(8)	[15]
Bromoperfluoroacetone	595.4(5)	7.87(8)	This work

[a] q_{zz} is the electric field gradient measured for the zz component of the tensor

[b] Numbers in parentheses give standard errors (1σ, 67% confidence level) in units of the least significant figure.

5.3. DIPOLE FORBIDDEN TRANSITIONS

As mentioned previously, multiple dipole forbidden transitions were observed for both isotopologues. All forbidden transitions are located in Table 3. Two types of dipole forbidden transitions were observed in this work. The first are $\Delta J = 2$ transitions. These have been observed when a molecule possesses nuclear quadrupole coupling constant

values similar in magnitude or larger than its rotational constant values [78, 79, 80, 81, 82]. These molecules have linkages between states of the forbidden transition and allowed transition due to an off-diagonal quadrupole coupling tensor component. The link must be of the type not represented by the tensor component. For instance, two states linked by x_{ab} are connected via a c-type relationship. At least one linking state is usually of little purity and both states are usually very close in energy but different in J.

Table 7. x_{zz} and electric field gradient comparisons for a series of halogen acetones molecules for major isotopes.

Molecule	χ_{zz} / MHz	q_{zz} / 10^{22} V m$^{-2,a}$	Reference
Chloroacetone	-70.(4)[b]	3.5(2)	[21]
1-chloro-3,3,3-trifluoroacetone	-78.0(1)	3.95(4)	[21]
Chloroperfluoroacetone	-75.(6)	3.8(3)	[22]
1,3-Dichlorotetrafluoroacetone[c]	-73.7(8)	3.73(5)	[22]
Bromoperfluoroacetone	595.4(5)	7.87(8)	This work

[a] qzz is the electric field gradient measured for the zz component of the tensor

[b] Numbers in parentheses give standard errors (1σ, 67% confidence level) in units of the least significant figure

[c] Equivalent chlorine nuclear so only one value reported

The other type of dipole forbidden transition that hasn't been observed in previous studies by any of the authors are x-type transitions. These transitions exhibit no change in parity for either K_a or K_c. These types of transitions are so rare that the authors were only able to find one reference to them being observed in the literature [107]. This finding

sparked a small investigation into the mechanism behind the observation of these transitions.

In order to understand what was happening in the dipole forbidden transitions the authors started with the .egy file provided by Pickett's SPCAT program [74]. This file can be activated with a flag variable in the one's digit of the first input of the second line of the .int file with a nonzero number, but a ``1" will give the diagonalized matrix and a ``5" will give the undiagonalized matrix. One unique aspect of this file is it will list two values of great importance in determining the mechanism of the forbidden transition, the P_{mix} coefficient and the state energy level referenced to the $J = 0$ state. The P_{mix} coefficient, with a value between zero and one, is a measure of a specific state's purity. A completely pure state would have a value of one. A listing of some selected states with P_{mix} and energy values is presented in Table 8.

To look for any possible mixing, the authors started with the assigned state quantum numbers for the forbidden transitions in the .egy file and looked at the P_{mix} value. When this value was low, then it was expected that another state in the same F block should also be similar in energy. This was commonly the case with some pairs of states being so close in energy that they were less than 1 MHz apart or being so mixed that their P_{mix} coefficients were less than 0.5.

The next step was to look for the mechanism of the forbidden transition(s). Since previous literature on $\Delta J = 2$ transitions had this happening through an off-diagonal quadrupole coupling tensor component, this is where the authors began their investigations. As the .egy file was searched, it was noticed that most linked states that were highly mixed and close in energy were associated via an a-type parity change. If

Table 8. Selected energy level mixing parameters and state degeneracies from Pickett's .egy file for ^{79}Br[a].

State	P_{mix} coefficient	Energy / cm^{-1}	ΔE^{b} / MHz
$7_{4,4}, \frac{17}{2}$	0.677580	1.654143	0.959
$7_{4,3}, \frac{17}{2}$	0.682386	1.654112	—
$8_{4,4}, \frac{19}{2}$	0.936862	1.991998	0.420
$8_{4,5}, \frac{19}{2}$	0.936862	1.991984	—
$5_{3,2}, \frac{13}{2}$	0.580824	0.898506	6.00
$5_{3,3}, \frac{13}{2}$	0.675897	0.898706	—
$5_{3,2}, \frac{11}{2}$	0.451900	0.899081	1.92
$5_{3,3}, \frac{11}{2}$	0.539062	0.899145	—
$6_{1,6}, \frac{13}{2}$	0.872980	0.900462	58.6
$5_{3,2}, \frac{13}{2}$	0.580824	0.898506	—
$6_{1,6}, \frac{11}{2}$	0.871521	0.898506	17.2
$5_{3,2}, \frac{11}{2}$	0.451900	0.899081	—

[a] See text for explanation of mixing mechanisms. States considered to be mixing are in paired groups in the table

[b] ΔE represents the energy difference between the two states in the mixing group

this is to happen according to the previous accounts, then x_{bc} must be responsible for this mixing [82]. To test this, the .egy file was flagged to give the undiagonalized matrix. The .egy files and all Pickett files for both isotopologues can be found in the Supplemental Data. It was noticed that states in the undiagonalized file contained nonzero matrix elements that were the same in each state considered to be mixing just like those reported in reference [78]. However, unlike reference [78] there was not just one value that was exactly the same between pairing states and only one value would scale linearly with a

changing of off-diagonal component usually thought to be mixing the two states (for this work this was x_{bc}), suggesting more is going on linking these states than purely the one off-diagonal contribution of the quadrupole [108]. Each forbidden transition is accompanied by a dipole allowed, observed transition consisting of one of the mixing states facilitating the connection.

Table 8 presents six selected pairs of mixing states for forbidden transitions observed in the bromine-79 isotopologue. Clearly (as mentioned earlier), there is near-degenerate behavior exhibited for many of these state pairings and the P_{mix} coefficient suggest very impure states. Furthermore, a look at the nonzero matrix elements in these examples give multiple matching elements ranging from a few MHz to 10^4 MHz! In the first couple of cases, there are clear linkages between the states, but not a clear answer as to what is the direct cause of the mixing. In the cases of the listed $6_{1,6}$, F$ and $5_{3,2}$, F levels, it seems that these states are even further linked through a third, intermediate state, $5_{3,3}$, F, that facilitates the necessary change in one of the K parameters, giving a x-type linkage facilitated through an a-type change in parity. The authors are unaware of any literature reporting this or even noticing this before. This may be rationalized by the fact that, due to the coupling and the asymmetric rotor, K quantum numbers have lost all quantum meaning and now simply act as a labelling mechanism, but this, again, is unclear. What is known, however, is that these transitions are being accurately predicted by the effective Hamiltonian being utilized insisting that the fitting procedure for these molecules is correct and no additional terms need to be added to the Hamiltonian for an adequate description of the transitions.

6. CONCLUSIONS

The microwave spectrum of bromoperfluoroacetone has been observed and reported for the first time on a newly constructed CP-FTMW spectrometer located at Missouri S&T. Rotational constants, centrifugal distortion constants, and the nuclear quadrupole coupling tensor components were determined for the 79 and 81 isotopologues of bromine. The spectra was dense and included the observation of dipole forbidden $\Delta J = 2$ and x-type transitions. Second moments and Kraitchman position of the bromine were used to compare the experimental structure to that of the calculations in this work and of W. C. Bailey [83, 94] and were found to agree. The quadrupole coupling tensor was diagonalized and x_{zz} has been used to arrive at the electric field gradients on the z-axis for a series of other molecules to help analyze the strength of the C-Br bond in the molecule. Dipole forbidden transitions have been observed and found to be always linked through a dipole allowed transition, but are not necessarily linked through one singular off-diagonal term. Furthermore, a select few of the dipole forbidden transitions are facilitated through a third mixing state for which the authors have not found compare in the literature. All transitions, however, are still being predicted accurately with the chosen Hamiltonian suggesting that the spectroscopic constants presented have been correctly reported.

ACKNOWLEDGEMENTS

REFERENCES

1. G.G. Brown, B.C. Dian, K.O. Douglass, S.M. Geyer, S.T. Shipman and B.H. Pate, Rev. Sci. Instrum. **79**, 053103 (2008).

2. G. S. Grubbs II, C. T. Dewberry, K. C. Etchison, K. E. Kerr, S. A.466 Cooke, Rev. Scient. Instrum. 78 (2007)

3. B. Reinhold, I. A. Finneran, S. T. Shipman, J. Mol. Spectrosc. 270468 (2011) 89.

4. K. N. Crabtree, M.-A. Martin-Drumel, G. G. Brown, S. A. Gaster, T. M. Hall, M. C. McCarthy, J. Chem. Phys. 144 (2016)

5. M.-A. Martin-Drumel, M. C. McCarthy, D. Patterson, B. A. McGuire, K. N. Crabtree, J. Chem. Phys. 144 (2016)

6. D. S. Wilcox, K. M. Hotopp, B. C. Dian 115 (2011) 8895.

7. K. Prozument, G. B. Park, R. G. Shaver, A. K. Vasiliou, J. M. Oldham, D. E. David, J. S. Muenter, J. F. Stanton, A. G. Suits, G. B. Ellison, R. W. Field, Phys. Chem. Chem. Phys. 16 (2014)

8. N. A. Seifert, I. A. Finneran, C. Perez, D. P. Zaleski, J. L. Neill, A. L. Steber, R. D. Suenram, A. Lesarri, S. T. Shipman, B. H. Pate, J. Mol. Spectrosc. 312 (2015)

9. S. A. Cooke, P. Ohring, Journal of Spectroscopy 2013 (2013)

10. H. M. Pickett, J. Mol. Spectrosc. 148 (1991)

11. Z. Kisiel, L. Pszczolkowski, I. R. Medvedev, M. Winnewisser, F. C. D. Lucia, C. E. Herbst, J. Mol. Spectrosc. 233 (2005)

12. C. M. WesternIn Press

13. D. Plusquellic, URL: http://www.nist.gov/pml/electromagnetics/grp05/jb95.cfm.

14. C. T. Dewberry, G.S. Grubbs II, S. A. Cooke, J. Mol. Spectrosc. 257 (2009)

15. B. E. Long, G. S. Grubbs II, J. D. Langridge, S. A. Cooke, J. Mol. Struct. 1023 (2012)

16. G. S. Grubbs II, W. C. Bailey, S. A. Cooke, Chem. Phys. Lett. 477 (2009)

17. G. S. Grubbs II, W. C. Bailey, S. A. Cooke, Mol. Phys. 107 (2009)

18. C. T. Dewberry, Z. Kisiel, S. A. Cooke, J. Mol. Spectrosc. 261 (2010)

19. W.C. Bailey, Bromine Nuclear Quadrupole Coupling Constants in Bromoperfluoroacetone URL: http://nqcc.wcbailey.net/CF3COCF2Br.html

20. N. Force, D. J. Gillcrist, C. C. Hurley, F. E. Marshall, N. A. Payton, T. D. Persinger, G. S. Grubbs II, THE CHIRPED PULSE AND CAVITY FOURIER TRANSFORM MICROWAVE (CP-FTMW AND FTMW) SPECTRUM OF BROMOPERFLUOROACETONE, The Ohio State University 69th International Symposium on Molecular Spectroscopy, 2014, WJ08

21. W. C. Bailey, S. A. Cooke, G. S. Grubbs II, J. Mol. Struct. Manuscript in Preparation

22. G. Kadiwar, C. T. Dewberry, G. S. Grubbs II, S. A. Cooke, THE SHAPES OF CHLOROPENTAFLUOROACETONE AND 1,3-DICHLOROTETRAFLUOROACETONE IN THE GAS PHASE, 65th International Symposium on Molecular Spectroscopy, Ohio State University at Columbus, OH, 2010, RH11

23. D. J. Finnigan, C. W. Gillies, R. D. Suenram, E. B. Wilson, H. Karlsson, J. Mol. Spectrosc. 57 (1975)

24. G. S. Grubbs II, J. Mol. Struct. Manuscript Submitted

25. Gaussian 03 Revision E.01, M. J. Frisch, G. W. Trucks, H. B. Schlegel, G. E. Scuseria, M. A. Robb, J. R. Cheeseman, J. A. Montgomery, Jr., T. Vreven, K. N. Kudin, J. C. Burant, J. M. Millam, S. S. Iyengar, J. Tomasi, V. Barone, B. Mennucci, M. Cossi, G. Scalmani, N. Rega, G. A. Petersson, H. Nakatsuji, M. Hada, M. Ehara, K. Toyota, R. Fukuda, J. Hasegawa, M. Ishida, T. Nakajima, Y. Honda, O. Kitao, H. Nakai, M. Klene, X. Li, J. E. Knox, H. P. Hratchian, J. B. Cross, V. Bakken, C. Adamo, J. Jaramillo, R. Gomperts, R. E. Stratmann, O. Yazyev, A. J. Austin, R. Cammi, C. Pomelli, J. W. Ochterski, P. Y. Ayala, K. Morokuma, G. A. Voth, P. Salvador, J. J. Dannenberg, V. G. Zakrzewski, S. Dapprich, A. D. Daniels, M. C. Strain, O. Farkas, D. K. Malick, A. D. Rabuck, K. Raghavachari, J. B. Foresman, J. V. Ortiz, Q. Cui, A. G. Baboul, S. Clifford, J. Cioslowski, B. B. Stefanov, G. Liu, A. Liashenko, P. Piskorz, I. Komaromi, R. L. Martin, D. J. Fox, T. Keith, M. A. Allaham, C. Y. Peng, A. Nanayakkara, M. Challacombe, P. M. W. Gill, B. Johnson, W. Chen, M. W. Wong, C. Gonzalez, J. A. Pople, Gaussian 03, Gaussian, Inc., 340 Quinnipiac Street, Building 40, Wallingford, CT, 06492, 2003, copyright Ⓒ 1994-2003

26. C. Møller, M. Plesset, Phys. Rev. 46 (1934) 618–622

27. R. Krishnan, J. S. Binkley, R. Seeger, J. A. Pople, J. Chem. Phys. 72 (1980)

28. M. N. Glukhovtsev, A. Pross, M. P. McGrath, L. Radom, J. Chem. Phys. 103 (1995)

29. L. A. Curtiss, M. P. McGrath, J.-P. Blandeau, N. E. Davis, R. C. Binning, Jr., L. Radom, J. Chem. Phys. 103 (1995)

30. W. C. Bailey, F. M. Gonzalez, J. Mol. Struct. 651-653 (2003)

31. G. S. Grubbs II, R. A. Powoski, D. Jojola, S. A. Cooke, J. Phys. Chem. A 114 (2010)

32. D. A. Obenchain, A. A. Elliott, A. L. Steber, R. A. Peebles, S. A. Peebles, C. J. Wurrey, G. A. Guirgis, J. Mol. Spectrosc. 261 (2010)

33. S. A. Cooke, SOME SIGNAL PROCESSING TECHNIQUES FOR USE IN BROADBAND TIME DOMAIN MICROWAVE SPECTROSCOPY, 71st International Symposium on Molecular Spectroscopy, University of Illinois-Urbana Champaign, IL, 2016, FD09

34. J. K. G. Watson, Vibrational Spectra and Structure 6 (1977)

35. U. Spoerel, H. Dreizler, W. Stahl, Z. Naturforsch. Teil A 49 (1994)

36. J. Kraitchman, Am. J. Phys. 21 (1953)

37. R. K. Bohn, J. A. Montgomery, Jr., H. H. Michels, J. A. Fournier, J. Mol. Spectrosc. 325 (2016)

38. W. Gordy, R. L. Cook, Microwave Molecular Spectra; Techniques of Chemistry Vol. XVIII, Wiley, New York, 1984

39. G. Audi, A. H. Wapstra, C. Thibault, Nucl. Phys. A 729 (2003)

40. P. Pyykkö, Mol. Phys. 106 (2008) 1965–1974

41. C. T. Dewberry, K. C. Etchison, G. S. Grubbs II, R. A. Powoski, M. M. Serafin, S. A. Peebles, S. A. Cooke, Phys. Chem. Chem. Phys.

42. C. H. Townes, B. P. Dailey, J. Chem. Phys. 17 (1949) 782

43. A. Maeda, I. R. Medvedev, F. C. De Lucia, E. Herbst, P. Groner, Astrophys. J. Supp. Ser. 175 (2008)

44. H. P. Benz, A. Bauder, H. H. Günthard, J. Mol. Spectrosc. 21 (1966)

45. C. C. Costain, Trans. Am. Crystallogr. Assoc. 2 (1966)

46. Y. Niide, I. Ohkoshi, M. Takano, J. Mol. Spectrosc. 89 (1981)

47. R. H. Schwendeman, F. L. Tobiason, J. Chem. Phys. 43 (1965)

48. G. S. Grubbs II, B. E. Long, R. A. Powoski, S. A. Cooke, J. Mol. Spectrosc. 258 (2009)

49. G. S. Grubbs II, W. C. Bailey, S. A. Cooke, J. Mol. Struct. 987 (2011)

III. OBSERVATION OF ^{36}ArH^{37}Cl, ^{38}Ar^{35}HCl, AND ^{38}ArH^{37}Cl IN NATURAL ABUNDANCE USING CP-FTMW SPECTROSCOPY

ABSTRACT

Multiple minor isotopologues of ArHCl have been observed and reported in natural abundance using two CP-FTMW spectrometers. These include the first known microwave observation of 38Ar isotopologues in natural abun- dance. The parameters derived from fits of the spectra have been utilized in calculating multiple molecular parameters for the system which are shown to be the best determined to date. From these new spectra, a mass-dependency of the derived Ar-Cl bond distance has been found as well as the variation of the large amplitude HCl averaging angle.

1. INTRODUCTION

The weakly bound ArHCl system has been of experimental and theoretical interest for over 40 years [114, 115, 116, 117, 118, 119, 120, 121]. Almost 20 years ago, advancements in molecular beam FTMW techniques pioneered by Balle and Flygare [122] and Grabow *et al* [123] allowed for the determination of the ^{36}ArH^{35}Cl spectroscopic constants and new structural determinations for the system that had been, at that time, already 20 years in the making [121].

New advancements made in the field of microwave spectroscopic techniques pioneered by Pate and coworkers in the form of the chirped pulse Fourier transform microwave (CP-FTMW) spectrometer have achieved a new level of sensitivity in

supersonic expansion rotational spectroscopy [124], allowing for the observation of rotational spectra of ^{38}Ar isotopic species in natural abundance reported presently. These experiments serve as a first-step to pave the way for future experiments with the technique to increase the sensitivity to needed levels for the spectrometer's viability as both a physical and analytical chemistry tool. Furthermore, additional isotopologue measurements on the ArHCl system can be used to better determine the overall structure of ArHCl, which can be used in benchmarking theoretical approaches in computing the potential energy surface of the system. With these points in mind, therefore, we report, for the first time, the microwave spectra of ^{36}ArH^{37}Cl, ^{38}ArH^{35}Cl and ^{38}ArH^{37}Cl observed in natural abundance.

2. EXPERIMENT

Experiments were carried out on two CP-FTMW spectrometers. One located at Missouri S&T and operational from 6-18 GHz and one located at the University of Virginia (UVa) and operational from 6-18.5 GHz. Details of these instruments have been discussed in references [124] and [125 or chapter 4 of this document]. For the Missouri S&T spectrometer, minor upgrades have been made to increase the sensitivity and efficiency of the instrument. These include minimizing the total length of cable in the setup to < 2 m, including only $\frac{1}{3}$ m from the receiving horn to the low noise amplifier; moving to a new low noise amplifier from Miteq JS42-06001800-18-8P, which has a lower noise factor of 1.8 dB; and a quick acquisition time from a combination of the 5 free-induction decays (FIDs) per gas pulse and a gas pulse rate of 5 Hz (pumping limit).

For the last addition, it should be noted that 25 Hz acquisition rates are never achieved and the real-time acquisition rate varies from 12-14 Hz. Changing any parameter to align with this true acquisition rate, however, lowers the new acquisition rate and the fastest rates can only be achieved by turning off any excess math functionality of the oscilloscope and doing the FFT after signal acquisition. Experiments were performed from 6-12 GHz and 12-18 GHz utilizing 4 μs chirp widths.

At Missouri S&T, ≥99\% HCl was purchased from Sigma-Aldrich and used without further purification. A 2% mix of HCl in industrial grade Ar was utilized for these experiments. During the initial setup and parameterization, it was noticed that less than atmospheric delivery was needed by the regulator for consistently strong spectra. In addition, this window of strong signal was quite sensitive to small changes in backing pressure so a regulator that could operate below atmospheric pressure with fine control was used. The final working pressures utilized in these experiments were between 12-14 psi (0.82-0.95 atm), consistent with the 0.85 atm reported by Kisiel and coworkers [121]. Because signal strength on the strongest transitions dominated the spectra at the baseline with a rectangular FFT window, a Hanning window was used with 20 μs FIDs. Typical linewidths (FWHM) of the spectra were 100 kHz and uncertainties of 10 kHz were attributed to line centers. 2 million FIDs were collected for 6-12 GHz while 1.5 million were collected for 12-18 GHz. Collection of the 6-12 GHz region took about 2 days while 12-18 took about 1.5 days. The averaged FID and spectra for 6-12 GHz is shown in Figure 1 and an example of weaker transitions are shown in Figure 2.
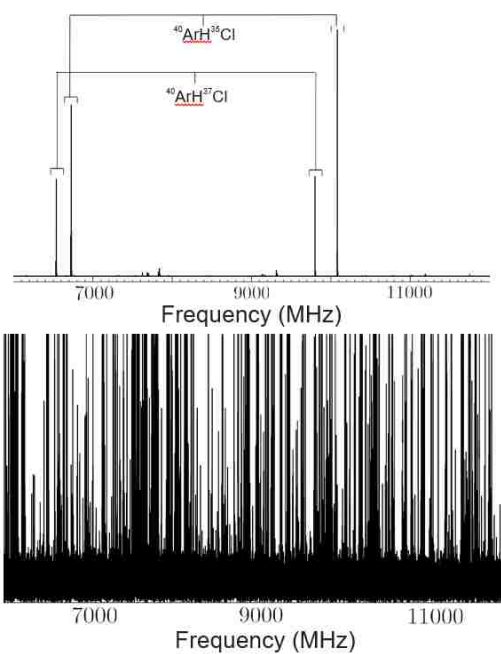
Figure 1. The 6-12 GHz spectrum of the 2% HCl in Ar mixture at the strongest signal (top) and noise floor (bottom) limits measured on the Missouri S&T CP-FTMW spectrometer. The ^{40}ArH^{35}Cl and ^{40}ArH^{37}Cl have been labelled for reference.
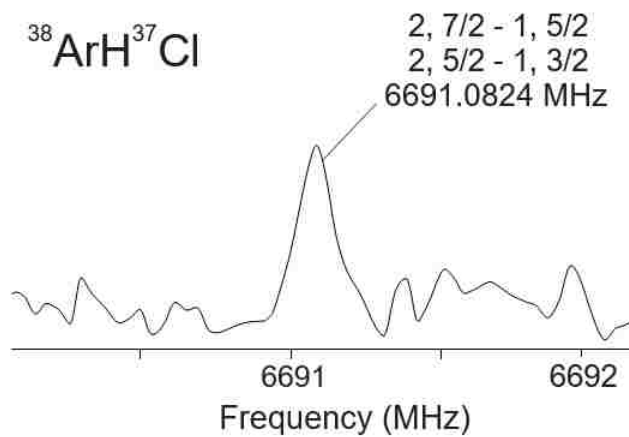
Figure 2. The strongest hyperfine component of the $J = 2$-1 transition of ^{38}ArH^{37}Cl measured at 6691.0824 MHz.

For the UVa data, we used spectra recorded while performing a search for the $(HCl)_2H_2O$ complex [126]. In this experiment, 1% HCl in Ar carrier was bubbled through a sample of liquid water at a stagnation pressure of 0.5 atm (7.35 psi). Three nozzles were utilized in a linear array with 10 FIDs/gas pulse for a total of 300,000 FID averages. As detailed in Ref. [126], signals of the strongest ArHCl species were immediately recognized and post-data collection analyses involved removing all possible transitions of already known clusters. Further analysis of the spectra revealed that unobserved weaker isotopologues of ArHCl were present and analyzed in the spectra. Transition uncertainties for these experiments were also assigned 10 kHz. Examples of weaker transitions observed with this spectrometer are shown in Figure 3.
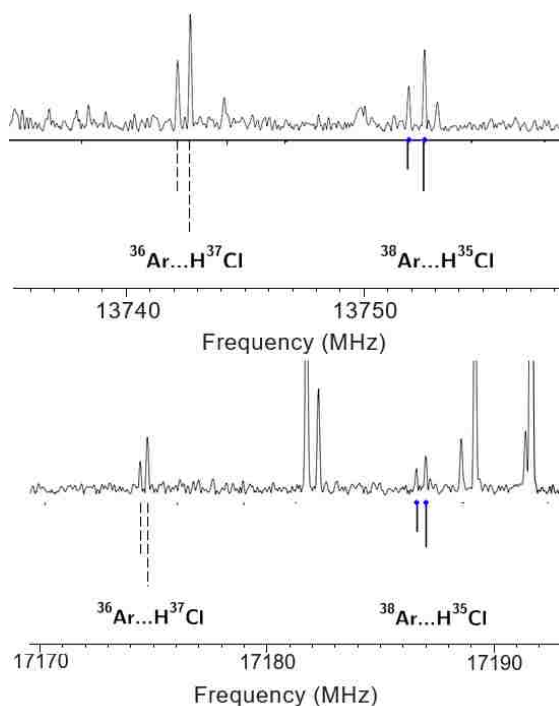
Figure 3. J ” − J I = 4 − 3 and 5 − 4 transitions of $^{36}ArH^{37}Cl$ and $^{38}ArH^{35}Cl$ measured at UVa.

3. RESULTS AND ANALYSIS

As is shown in Figure 1, close to the noise floor there were many transitions to sort out. Easily observable were the Ar_2HCl [127] and Ar_3HCl [128] transitions which easily surpassed signal-to-noise ratios of 1000:1 and 300:1, respectively, on many of their transitions while the strongest $^{38}ArH^{37}Cl$ transitions exhibited <10:1 S:N. Figure 4 shows these relative intensity differences. In addition, the sample contained water vapor as lines from van der Waals complexes H_2O-HCl [129,130], $(H_2O)_2HCl$ [131], and $(HCl)_2H_2O$ [126] were all easily observable in the spectra. Assignment, then, was based on a analysis-first approach. Since complexes of Ar and HCl are some of the most exhaustively studied systems, literature searches for spectroscopic constants, transitions and structures were heavily relied upon to make very accurate educated guesses at the weaker isotopologues. The previous works included in this exercise were Ref. [114, 115, 116, 117, 118, 121]. The method was extremely successful as initial predictions were, at worst, 5 MHz off and, at best, within kHz of the actual transition. Assignments were made utilizing the AABS package [132] made available through the PROSPE website [133, 134]. AABS works as a front-end for fitting spectra in the Pickett SPFIT/SPCAT program suite [135]. A linear rotor Hamiltonian was used in accordance with the previous literature where experiments were sometimes performed at higher resolution. Table 1 reports all measured spectroscopic parameters. All assignments and analyses can be found in the Supplemental Information.
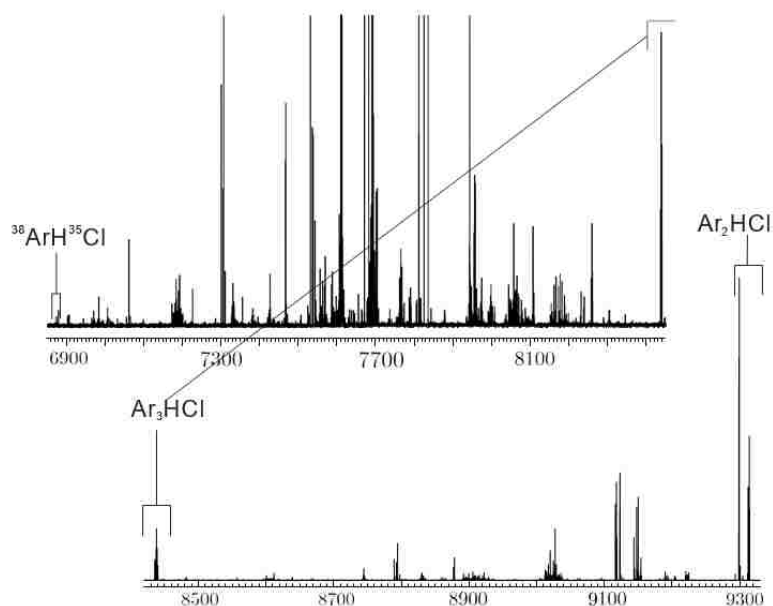
Figure 4. A comparison of relative intensity differences for Ar$_2$HCl to Ar$_3$HCl transitions in the spectra (bottom) compared to the relative intensity difference of the same Ar$_3$HCl transitions to those of ^{38}ArH^{35}Cl (top). The bottom spectra has been normalized to the Ar$_2$HCl transition intensity and the top spectra has been normalized to the Ar$_3$HCl intensity.

As Table 2 reports, a total of 36 transitions were assigned to 3 new isotopologues, ^{36}ArH^{37}Cl (14 transitions, 0.08084(9)% abundant [136]), ^{38}ArH^{35}Cl (14 transitions, 0.04764(9)% abundant [136]), and ^{38}ArH^{37}Cl (8 transitions, 0.01523(3)% abundant [136]). These are listed in Table 2. In addition to these, 15 new transitions were measured for ^{36}ArH^{35}Cl (0.2527(3)% abundant [136]). Due to the very similar mass changes of ^{36}ArH^{37}Cl and ^{38}ArH^{35}Cl relative to the parent species, the locations of the transitions were very similar making these the hardest to assign. In these particular cases, the methods utilized for giving a good estimate were not entirely reliable as the predicted rotational constants were essentially the same. However, the differences due to the quadrupole coupling values of ^{35}Cl and ^{37}Cl used in conjunction with the relative

intensity differences due to the natural abundance of each was used to discern the isotopologues. The general reliability of chirped pulse methods with relative intensity data has been stated previously in the literature [137]. All deviation of fit (RMS) values are very close to or less than the attributed uncertainties of the line centers.

Table 1. Spectroscopic Parameters of ArHCl compared to previous works. Fits contain previously measured transitioned unless otherwise stated.

	^{40}ArH^{35}Cl			^{40}ArH^{37}Cl		
Abundance[a] / %	75.453(4)			24.135(4)		
Parameter	This Work[b]	Ref. [8]	Ref. [1, 2, 3, 4][c]	This Work[b]	Ref. [8]	Ref. [1, 2, 3, 4][c]
B_0 / MHz	1678.5072(3)[d]	1678.50839(4)	1678.5086(25)	1631.5952(3)	1631.59632(5)	1631.59645(88)
D_J / kHz	20.04(1)	20.0636(8)	19.991(13)	18.904(8)	18.9390(13)	18.900(6)
χ_{aa}(Cl) / MHz	−23.041(5)	−23.0289(7)	−23.0297(5)	−18.213(4)	−18.1965(10)	−18.203(34)
χ_{aa}^{J}(Cl) / MHz	−	−1.59(5)	−1.60(5)	−	−1.16(11)	−
M_{bb}(Cl) / kHz	−	0.16(4)	0.132(16)	−	0.16(5)	−
D_{aa} / kHz	−	−6.0(5)	−	−	−4.4(5)	−
N[e]	27	34	−	26	22	−
MW RMS[f] / kHz	5.2	0.43	−	4.4	0.36	−
	^{36}ArH^{35}Cl			^{36}ArH^{37}Cl		
Abundance / %	0.2527(3)			0.08084(9)		
Parameter	This Work		Ref. [8]	This Work		
B_0 / MHz	1765.4328(4)		1765.43270(24)	1718.5230(2)		
D_J / kHz	22.34(1)		22.327(16)	21.139(6)		
χ_{aa}(Cl) / MHz	−22.993(7)		−22.9942(43)	−18.25(3)		
N[e]	23		8	14		
MW RMS[f] / kHz	10.9		1.20	1.3		
	^{38}ArH^{35}Cl			^{38}ArH^{37}Cl		
Abundance / %	0.04764(9)			0.01524(3)		
Parameter	This Work			This Work		
B_0 / MHz	1719.745(1)			1672.833(1)		
D_J / kHz	21.10(3)			19.85(6)		
χ_{aa}(Cl) / MHz	−23.09(2)			−18.39(3)		
N[e]	14			8		
MW RMS[f] / kHz	10.8			5.8		

[a] Calculated from reported values in Ref. [136]

[b] Only includes CP-FTMW transitions

[c] As reported in Ref. [121]

[d] Numbers in parentheses give standard errors (1σ, 67% confidence level) in units of the least significant figure

[e] Number of observed transitions used in the fit

[f] MW RMS is defined as $\sqrt{\dfrac{(obs-calc)^2}{N}}$

Table 2. Newly observed isotopologue transitions.

^{36}ArH^{37}Cl		^{38}ArH^{35}Cl		^{38}ArH^{37}Cl	
$J', 2F' - J'', 2F''$	Frequency / MHz	$J', 2F' - J'', 2F''$	Frequency / MHz	$J', 2F' - J'', 2F''$	Frequency / MHz
2, 5 - 1, 3	6873.8059	2, 5 - 1, 5	6873.0119	2, 5 - 1, 3	6691.0824
2, 7 - 1, 5	6873.8059	2, 7 - 1, 5	6878.8008	2, 7 - 1, 5	6691.0824
3, 3 - 2, 1	10307.9419	2, 3 - 1, 3	6882.9092	3, 7 - 2, 7	10030.4716
3, 5 - 2, 3	10307.9419	3, 5 - 2, 3	10315.0530	3, 5 - 2, 3	10033.9391
3, 7 - 2, 5	10309.0725	3, 3 - 2, 1	10315.0530	3, 9 - 2, 7	10035.0774
3, 9 - 2, 7	10309.0725	3, 9 - 2, 7	10316.4681	4, 5 - 3, 3	13377.1914
4, 5 - 3, 3	13742.3822	3, 5 - 2, 5	10319.1709	4, 9 - 3, 7	13377.7140
4, 7 - 3, 5	13742.3822	4, 5 - 3, 3	13752.0750	4, 11 - 3, 9	13377.7140
4, 9 - 3, 7	13742.9106	4, 9 - 3, 7	13752.7391		
4, 11 - 3, 9	13742.9106	4, 11 - 3, 9	13752.7391		
5, 7 - 4, 5	17174.4405	5, 9 - 4, 7	17186.6157		
5, 9 - 4, 7	17174.4405	5, 7 - 4, 5	17186.6157		
5, 11 - 4, 9	17174.7581	5, 11 - 4, 9	17187.0271		
5, 13 - 4, 11	17174.7581	5, 13 - 4, 11	17187.0271		

4. DISCUSSION

Measurement of the new isotopologues allowed for a more in-depth look at the structure of the ArHCl complex. These analyses were done using a combination of Kisiel's STRFIT program [138] and other literature methodologies [139,140]. Given that ArHCl is very weakly bound, the simplest analysis of isotopic substitution data by means of Kraitchman substitution (r_s structure) is known to be poorly applicable. When this was attempted, however, different starting points led to different placements of all atomic positions. Further investigation into this showed that the r_m methods of Watson [141] are inherently more reliable for this system and can be performed easily using STRFIT in a model tested on five isotopologues [138]. These structures, including the c_b parameter and the Laurie delta parameters [142], have been updated using all isotopic data currently

available. These are presented in Table 3. Since ^{40}ArH^{35}Cl and ^{40}ArH^{37}Cl were measured

in Ref. [121] at much higher resolution while also featuring more transitions than in this

work, the fits utilized the B_0 values reported in that work. The newly determined structure

is in excellent agreement with the previous structure reported in Ref. [138], but now with

better determined values for all floated parameters due to the added number of

isotopologues in the fit. The quality of this fit for each isotopologue is presented in Table

4, with the worst being ^{40}ArD^{35}Cl and ^{40}ArD^{37}Cl with obs-calc values of approximately

30 kHz each. Notably, the uncertainties of the r_m^{1L} and c_b parameters reported in Table 3

have both decreased by about a factor of two while the uncertainty of the entire fit also

decreased from 0.00535 μÅ to 0.00365 μÅ. The authors report the new r_m^{1L} heavy atom

separation for ArHCl to be 4.0252(7) Å.

Table 3. r_m^{1L} structure and Laurie delta parameters determined for ArHCl[a].

Parameter	This Work	Ref. [25]
r_m^{1L} /Å	4.02521(72)^b	4.0253(12)
c_b /u$^{\frac{1}{2}}$Å	0.4327(67)	0.432(11)
δ_H(ArH) /u$^{\frac{1}{2}}$Å	0.254178(81)	0.25418(10)
δ_H(HCl) /u$^{\frac{1}{2}}$Å	[−.320]	[−0.320]
$10^3\sigma$ /uÅ	3.65	5.35
Number of Isotopologues	8	5

[a] Fits utilize ref [121] for ^{40}ArH^{35}Cl values due to precision. See text for details

[b] Numbers in parentheses give standard errors (1σ, 67% confidence level) in units of the least significant digit

In addition, full analyses of the new isotopologue data were made using the

pseudodiatomic method [139], traditional R_0 linear analysis, and the off-axis corrected

ArCl bond distance adjusted value of Bevan and Legon [140]. These are tabulated in

Table 5 and ordered according to decreasing Ar isotope mass for the ^{35}Cl and the ^{37}Cl

isotopologues. Except for a deviation in ^{38}ArH^{37}Cl, the weakest and least accurately

determined isotopologue of this study, there is a systematic decrease in the calculated

force constant as the mass of Ar decreases. This decrease in the force constant of the

complex has a direct effect on the ArCl bond length as it systematically increases using

both bond length analysis equations. This was also found and mentioned in Ref. [121].

The large amplitude averaging angle of the HCl axis in relation to the a-axis of the

complex was found by assuming there was no change in the x_{aa} value of HCl upon

complexation and the only difference in the value is due to the projection of the free

value onto the new a-axis. These values are more difficult to rationalize. ^{35}Cl species

values seem relatively invariant at about 41.5°, but ^{37}Cl values seem to be systematically

increasing from 40.97° for ^{40}ArH^{37}Cl. This seems odd considering that all other trends

seemingly hold fairly consistent across all isotopologues and the authors have no real

explanation for this trend.

Table 4. Observed and observed-calculated rotational constants and moments of inertia[a].

Isotopologue	B_0 / MHz	B_0(obs-calc) / MHz	I / uÅ²	I(obs-calc) / uÅ²
^{40}ArH^{35}Cl	1678.50839(4)[b]	−0.0016	301.088162(7)	0.00029
^{40}ArH^{37}Cl	1631.59632(5)	0.0081	309.745125(9)	−0.00154
^{36}ArH^{35}Cl	1765.4328(4)	−0.0115	286.26352(7)	0.00187
^{36}ArH^{37}Cl	1718.5230(2)	0.0054	294.07753(3)	−0.00093
^{38}ArH^{35}Cl	1719.745(1)	−0.0075	293.86857(17)	0.00128
^{38}ArH^{37}Cl	1672.833(1)	0.0045	302.10966(18)	−0.00082
^{40}ArD^{35}Cl	1657.638(4)	0.0296	304.87899(74)	−0.00544
^{40}ArD^{37}Cl	1611.903(2)	−0.0272	313.52942(39)	0.00529

[a] Fits utilize ref [121] for ^{40}ArH^{35}Cl values due to precision. See text for details

[b] Numbers in parentheses give standard errors (1σ, 67% confidence level) in units of the least significant digit

Table 5. Derived parameters of isotopologues of ArHCl.

Parameter	$^{40}ArH^{35}Cl$[8]	$^{38}ArH^{35}Cl$	$^{36}ArH^{35}Cl$	$^{40}ArH^{37}Cl$[8]	$^{38}ArH^{37}Cl$	$^{36}ArH^{37}Cl$
k^a / N m^{-1}	1.164	1.161	1.155	1.165	1.167	1.157
$\theta_{av}{}^b$ /deg	41.53	41.49	41.55	40.97	41.36	41.46
$R_0(ArCl)^c$ /Å	4.0131	4.0136	4.0142	4.0121	4.0126	4.0131
$R_0^{av,d}$ /Å	4.0065	4.0070	4.0076	4.0060	4.0064	4.0070

[a] Defined from D_J using the pseudodiatomic method of Ref [136]

[b] Defined by x_{aa}(dimer) $= \frac{1}{2} x_{aa}^{free} (3 \cos^2 \theta_{av} - 1)$

[c] Evaluated from B_0 assuming r_0 (HCl in dimer) = r_0 (free HCl) = 1.2839 Å

[d] Evaluated from equations 3 and 4 of Ref. [137]

5. CONCLUSION

This work describes the first observations of an ^{38}Ar-containing van der Waals complex, ArHCl, using microwave rotational techniques. These measurements have been achieved using CP-FTMW spectrometers located at Missouri S&T and UVa, demonstrating the power of the CP-FTMW technique along with the potential sensitivity capabilities. These new measurements have allowed for a more complete determination of the structure and all determined structural parameters have been found to be in good agreement with previous results. The determined rotational and quadrupole parameters have provided a more in-depth look into the quantitative structure of ArHCl. The newly discovered isotopologues have been used to determine the best r_m^{1L} ArCl distance for ArHCl to date, 4.0252(7) Å. In addition, individual isotopologue pseudodiatomic and rotational analysis shows a systematic increase in the ArCl bond distance consistent with

that observed in Ref. [121], but an unexpected variation in the HCl averaging angle was observed.

ACKNOWLEDGEMENTS

REFERENCES

1. S. E. Novick, P. Davies, S. J. Harris, W. Klemperer, J. Chem. Phys. 59 (1973)

2. S. E. Novick, K. Janda, S. L. Holmgren, M. Waldman, W. Klemperer, J. Chem. Phys. 65 (1976)

3. J. M. Hutson, B. J. Howard, J. Chem. Phys. 74 (1981)

4. K. L. Busarow, G. A. Blake, K. B. Laughlin, R. C. Cohen, Y. T. Lee, R. J. Saykally, J. Chem. Phys. 89 (1988)

5. C. Chuang, H. S. Gutowsky, J. Chem. Phys. 94 (1991)

6. J. M. Hutson, J. Chem. Phys. 89 (1988)

7. M. J. Elrod, B. C. Host, D. W. Steyert, R. J. Saykally, Mol. Phys. 79 (1993)

8. Z. Kisiel, L. Pszczółkowski, Chem. Phys. Lett. 291 (1998)

9. T. J. Balle, W. H. Flygare, Rev. Scient. Instrum. 52 (1981)

10. J. U. Grabow, W. Stahl, H. Dreizler, Rev. Scient. Instrum. 67 (1996)

11. G. G. Brown, B. C. Dian, K. O. Douglass, S. M. Geyer, S. T. Shipman, B. H. Pate, Rev. Scient. Instrum. 79 (2008)

12. F. E. Marshall, D. J. Gillcrist, T. D. Persinger, S. Jaeger, C. C. Hurley, N. E. Shreve, N. Moon, G. S. Grubbs II, J. Mol. Spectrosc. 328 (2016)

13. Z. Kisiel, A. Lesarri, J. L. Neill, M. T. Muckle, B. H. Pate, Phys. Chem. Chem. Phys. 13 (2011)

14. T. D. Klots, C. Chuang, R. S. Ruoff, T. Emilsson, H. S. Gutowsky, J. Chem. Phys. 86 (1987)

15. T. D. Klots, R. S. Ruoff, C. Chuang, T. Emilsson, H. S. Gutowsky, J. Chem. Phys. 87 (1987)

16. A. C. Legon, L. C. Willoughby, Chem. Phys. Lett. 95 (1983)

17. Z. Kisiel, B. A. Pietrewicz, P. W. Fowler, A. C. Legon, E. Steiner, J. Phys. Chem. A 104 (2000)

18. Z. Kisiel, E. Białkowska-Jaworska, L. Pszczółkoski, A. Milet, C. Struniewicz, R. Moszynski, J. Sadlej, J. Chem. Phys. 112 (2000)

19. Z. Kisiel, L. Pszczółkowski, I. R. Medvedev, M. Winnewisser, F. C. D. Lucia, C. E. Herbst, J. Mol. Spectrosc. 233 (2005)

20. Z. Kisiel, Assignment and Analysis of Complex Rotational Spectra.

21. Z. Kisiel, PROSPE – Programs for ROtational SPEctroscopy, URL: http://info.ifpan.edu.pl/ kisiel/prospe.htm.

22. H. M. Pickett, J. Mol. Spectrosc. 148 (1991) 371

23. J. Meija, T. B. Coplen, M. Berglund, W. A. Brand, P. De Biévre, M. Gröning, N. E. Holden, J. Irrgeher, R. D. Loss, T. Walczyk, T. Prohaska, Pure Appl. Chem. 88 (2016)

24. G. S. Grubbs II, C. T. Dewberry, K. C. Etchison, K. E. Kerr, S. A. Cooke, Rev. Scient. Instrum. 78 (2007)

25. Z. Kisiel, J. Mol. Spectrosc. 218 (2003)

26. D. Millen, Can. J. Chem. 63 (1985)

27. J. W. Bevan, A. C. Legon, C. A. Rego, J. Roach, Chem. Phys. Lett. 198 (1992)

28. J. K. G. Watson, A. Roytburg, W. Ulrich, J. Mol. Spectrosc. 196` (1999)

29. V. W. Laurie, J. Chem. Phys. 28 (1958) 704

IV. THE CP-FTMW SPECTRUM OF 1,1-DIFLUOROSILACYCLAPENT-2-ENE

ABSTRACT

The rotational spectrum of 1,1-difluorosilacyclopent-2-ene was observed in the 6 to 18 GHz range of the electromagnetic spectrum. The molecular structure for the parent and various isotopically substituted species were obtained from their respective spectra. The differences in structure between these similar molecules will be presented, showing how different functional groups and bond locations affect the overall structure and behavior of each system (ring puckering effects, etc.). Comparisons to similar known cyclopentane and silacyclopentane species will be presented.

1. EXPERIMENT

The experiment was carried out at the Missouri University of Science and Technology using a Chirped Pulse, Fourier Transform Microwave Spectrometer (CP-FTMW). The details of this spectrometer have been outlined previously in references [143], [144], and [145]. The 1,1-difluorosilacylapent-2-ene sample was synthesized at the College of Charleston, while microwave experiments were performed at Missouri S&T. The sample, originally a liquid, was made into a gas mix by utilizing the vapor pressure of the molecule at room temperature. A gas tank was evacuated and attached to the sample, which then allowed the sampled to vaporize. The vapor in the tank was then mixed with industrial grade Argon gas until the sample was 3% in concentration. The 3%

gas tank was then attached to the CP-FTMW and sample was introduced at a sub-atmospheric pressure of -10inHg (about 0.66 atm relative to vacuum).

Spectra of 1,1-difluorosilacyclapent-2-ene were then acquired in the 6-12 and 12-18 GHz regions of the electromagnetic spectrum using 4 µS chirp lengths. A Parker-Hannifin® Series 9 supersonic nozzle pulsed sample into the chamber at a rate of 5 Hz with 5 FIDs acquired per gas pulse. In total 665,000 FIDs, each FID being 20µS in length, were averaged together in each frequency range before the sample was completely depleted. Spectra for the 6-12 GHz and 12-18 GHz range can be seen in Figure 1 and Figure 2, respectively. Typical linewidths for the spectra were 70-80 kHz.
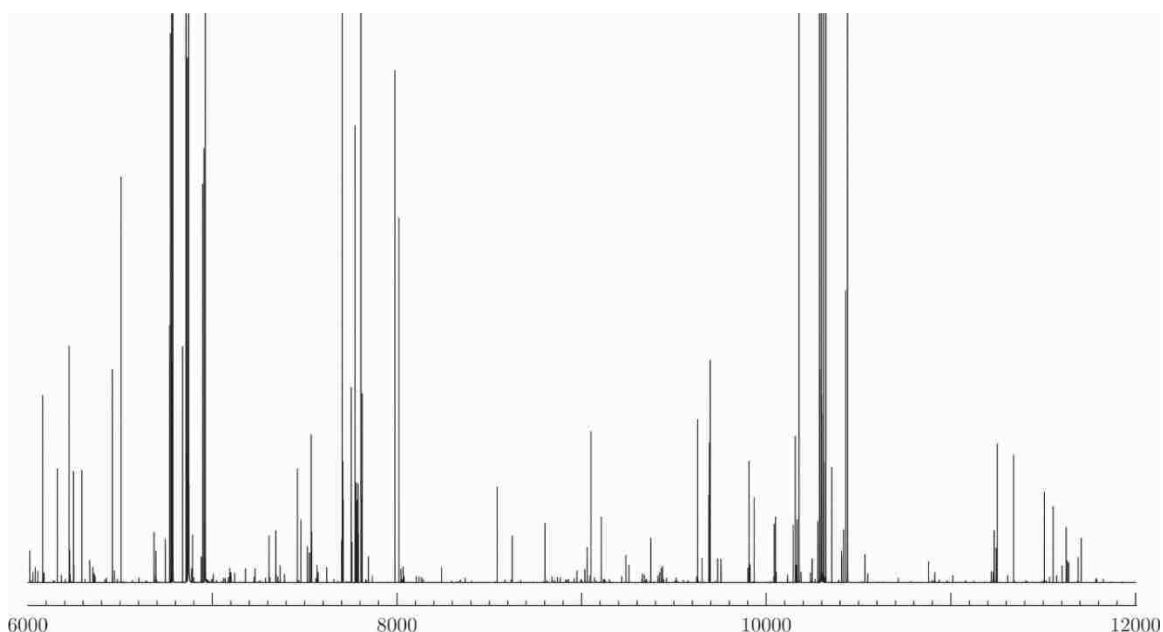
Figure 1. The 6-12 GHz spectra for 1,1-difluorosilacyclapent-2-ene.
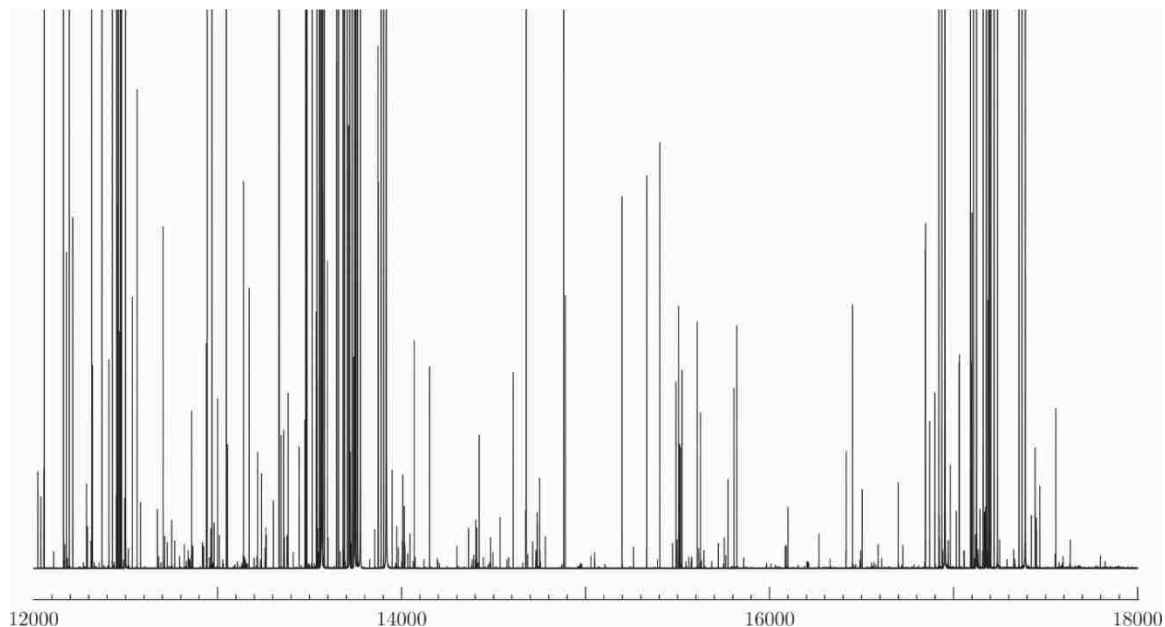
Figure 2. The 12-18 GHz spectra for 1,1-difluorosilacyclapent-2-ene.

2. COMPUTATIONAL METHODS

Calculations for 1,1-difluorosilacyclapent-2-ene were done using Gaussian09 Revision C.01 [146]. The calculations were carried out at the B3LYP/def2TZVP with GD3BJ empirical dispersion correction of Grimme [5]. The predicted rotational constants can be found in Table 1. The calculated structure can be found in Figures 3, 4, and 5.
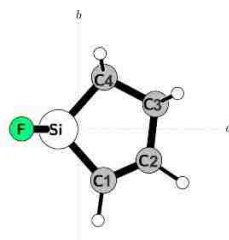
Figure 3. The calculated structure for 1,1-difluorosilacyclapent-2-ene shown in the *ab* plane.

Table 1. The predicted and experimental rotational constants and dipole moments.

Parameter	B3LYP/def2TZVP	c-$C_4H_6^{28}$SiF$_2$	c-$C_4H_6^{29}$SiF$_2$	c-$C_4H_6^{30}$SiF$_2$	$^{13}C_1$	$^{13}C_2$	$^{13}C_3$	$^{13}C_4$
A / MHz	3581.3	3598.8869 (29)	3599.94 (40)	3598.77 (27)	3551.1 (1)	3550.88 (22)	3588.56 (34)	3582.10 (47)
B / MHz	1745.8	1762.27587 (72)	1760.4638 (21)	1758.6831 (14)	1759.637 (1)	1759.4668 (14)	1736.6725 (17)	1740.5871 (25)
C / MHz	1663.6	1674.73167 (79)	1673.0917 (21)	1671.4854 (14)	1661.969 (1)	1661.7869 (14)	1649.2827 (17)	1651.4736 (25)
D_j / MHz	-	0.000144 (13)	0.000183 (35)	0.000156 (24)	0.000017 (2)	.000160 (24)	.000136 (30)	0.000173 (43)
D_{jk} / MHz	-	0.002006 (44)	0.00195 (11)	0.002088 (77)	.00181 (7)	.001815 (79)	.00198 (10)	.00177 (14)
D_k / MHz	-	-0.10382 (36)	-0.10382	-0.10382	-0.10382	-0.10382	-0.10382	-0.10382
μ_a / D	0.701							
μ_b / D	0.933							

Table 1. The predicted and experimental rotational constants and dipole moments (cont.).

μ_c / D	0.139							
N		36	23	23	23	23	22	23
ν_{rms} / kHz		10.6	14.7	9.9	9.2	10.2	12.4	22.0
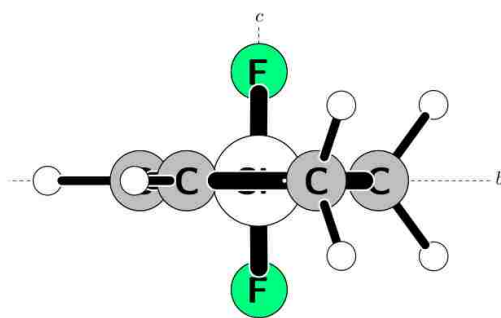
Figure 4. The calculated structure for 1,1-difluorosilacyclapent-2-ene shown in the *bc* plane.
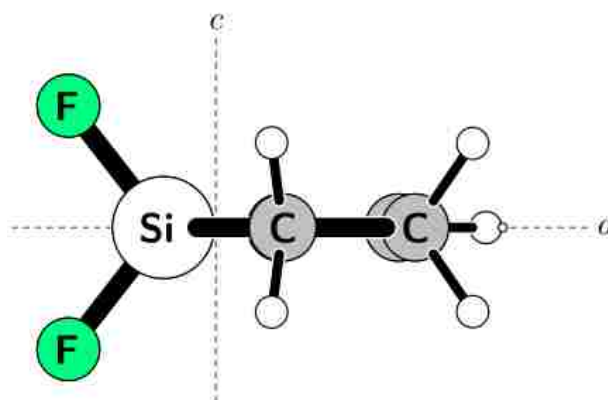
Figure 5. The calculated structure for 1,1-difluorosilacyclapent-2-ene shown in the *ac* plane.

3. RESULTS AND ANALYSIS

Analysis of the spectra was done through the use of SPFIT and SPCAT [148] in combination with Z. Kisiel's AABS package [149]. Using the calculated rotational constants and dipole information, which can be seen in Table 1, a total of 36 lines for the parent species were observed. Additionally, the isotopologues corresponding to each ^{13}C, ^{29}Si, and ^{30}Si were observed and their corresponding rotational constants can also be found in Table 1. Assignments were carried out in the I^r representation. The input files and quantum number assignments can be found in the Supporting Information.

It is important to note that some of the transitions in the spectra were split. These splittings were not predicted by the quantum chemical calculations. This is likely due to some sort of large amplitude motion, however the actual cause is not yet clear. Only 3 split lines were observed in the spectra which makes it impossible to determine the barrier to motion for further analysis. Some transitions had abnormal linewidths on the order of 100-120kHz, approximately 20-50kHz wider than normal, that could be due to unresolved split transitions. Further analysis was not done because the entirety of the sample was depleted.

The majority of the observed lines are b-type transitions. The next most abundant transition type, which were also the most intense, are a-type transitions. No c-type transitions were observed. These observations are in accordance with the predicted dipole values in Table 1. Observing primarily b-type transitions would be expected with μ_b having the largest value at 0.933 D. Because μ_a has a value of 0.701 D, which is similar in magnitude to μ_b, it follows that a-type transitions would also be prevalent. Finally,

because μ_c only has a magnitude of 0.139 D, which is more than 5 times smaller than μ_a, it is reasonable that no c-type spectra were observed.

Identifying the ^{13}C, [29]Si, and [30]Si isotopes was done by comparing the ratio of the calculated rotational constants of the parent and those determined by the experiment with the calculated rotational constants of the isotopes. This yielded a prediction of the isotopic rotational constants accurate to within a few MHz. After successfully finding and identifying each of these isotopes, a Kraitchman [150] heavy atom substitution structure was derived and can be found in Table 2. This process was carried out using Kisiel's KRA program [151] to determine the Kraitchman structure and then the EVAL program [152] to determine the corresponding bond angles and bond lengths. These values can be seen in Tables 3 and 4 respectively.

Table 2. Kraitchman heavy atom substitution coordinates in Å.

Isotope	a	da	b	db	c	dc
[13]C(1)	0.6523	0.0154	-1.3797	0.0075	0	0
[13]C(2)	1.8933	0.0026	-0.8291	0.0060	0.0569	0.0513
[13]C(3)	2.061	0.0018	0.6564	0.0057	0	0
[13]C(4)	0.6718	0.0040	1.3823	0.0020	0	0
[29]Si	-0.5647	0.0075	0	0	0	0
[30]Si	-0.5452	0.0037	0.0350	0.0576	0.0333	0.0606

Table 3. Experimental bond lengths.

Bond	Bond Length (Å)
Si-C(1)	1.840 (13)
Si-C(4)	1.855 (16)
C(1)=C(2)	1.358 (15)
C(2)-C(3)	1.495 (8)
C(3)-C(4)	1.569 (5)

Table 4. Experimental bond angles.

Bond	Bond Angle (°)
∠C(1)SiC(4)	96.77 (53)
∠SiC(1)C(2)	107.49 (54)
∠C(1)C(2)C(3)	120.38 (49)
∠C(2)C(3)C(4)	111.11 (23)
∠C(3)C(4)Si	104.15 (31)

It should be noted that the coordinates supplied in Table 2 have negative values, which are not obtained in a Kraitchman analysis. These negative values were obtained by correlating the substitution structure with the quantum chemical calculations. If an atom was found to have negative coordinates in the optimization calculation, then negatives were assigned to the corresponding atom in the substitution structure.

When inspecting the bond lengths and angles derived from the Kraitchman structure it is useful to compare against predicted values. The calculated Si-C bond lengths are approximately 1.83 Å and 1.86 Å. This is in close agreement with the experimental Si-C bond lengths, which are approximately 1.837 Å and 1.855 Å. Common values for Si-C bond lengths, according to the CRC Handbook [153] are approximately

1.81 Å, which is in close agreement as well. C-C bond lengths for this molecule are predicted to be 1.55 Å and 1.51 Å while the experimental values are 1.569 Å and 1.495 Å, respectively. Typical CRC values for C-C bonds are 1.53 Å, which are, again, in relatively close agreement. Finally, the C=C bond is predicted to be approximately 1.34 Å while the experimental value, which is close agreement, is 1.358 Å.

4. DISCUSSION

In the previous section it discussed that the a-type transitions were the most intense despite μ_a having a smaller value than μ_b ($\mu_a = 0.701$ D $< \mu_b = 0.933$ D). Though the values are similar in magnitude, it would seem that b-type transitions should have the greater intensity. It is possible that planar motion is affecting the axis system, and therefore the dipole moments. The suspected planar motion involves the movement of Carbons 2 and 3 in and out of the ab plane, however further computation is required to confirm this. This kind of movement will likely affect the dipole moments, which will affect experimental spectral intensity.

In comparing the calculated structure to the experimental structure, as done in the previous section, it can be seen that the calculations are in relatively good agreement with the experiment. The bond lengths and bond angles are within close agreement between both the calculation and experiment. It can be concluded from this that the use of a B3LYP/def2TZVP method with GD3BJ empirical dispersion correction is a good calculation to use for this family of molecules. Such a calculation should yield rotational

constants that are only a few hundred kHz off of actual values, which will expedite assigning the spectra.

Visual inspection of the fit shows that one parameter – the D_k centrifugal distortion constant – is unusually large. D_j has a value of .000144 MHz, meaning that this is a relatively rigid molecule with minimal centrifugal distortion. D_k, with a value of 0.10382MHz, is significantly large, which is typically a sign that this constant is accounting for some other phenomenon in the spectra. In this case, it is likely that D_k is accounting for the increased linewidth due to not being able to resolve the splittings from the out of plane motion. Further experimenting and analysis will likely be required to verify this, however. It should be noted that all the isotopologues had to be fit with D_k being held constant to the value of the parent parameter.

It is useful to compare the structure from this molecule to the structure for similar molecules. A similar molecule, 1-fluoro-1-silacyclopentane, was synthesized and analyzed by Durig, et al. . . and studied using Microwave, Infrared, and Raman measurements [154]. In this study, the complete heavy atom substitution structure was also observed and a Kraitchman analysis was also performed. Direct comparison of the rotational and centrifugal distortion constants can be found in Table 5. In general, the rotational constants for 1,1-difluorosilacyclapentane were smaller. This is to be expected as the molecules are the same composition - save for the substitution of a fluorine atom over a hydrogen atom and the addition of a C-C double bond in the title molecule- and rotational constants are inversely proportional to the mass. It is interesting to note, however, that magnitude of both of the centrifugal distortion constants D_j and D_{jk} are similarly small between the molecules (0.144 kHz and 2.006 kHz respectively for 1,1-

difluorosilacyclapent-2-ene and .727kHz and 2.77kHz respectively for 1-fluoro-1-

silacyclaclapentane), but the magnitude of D_k is very different. For 1,1-

difluorosilacyclapent-2-ene D_k is -103.8kHz while D_k is 6.1kHz for 1-fluro-1-

silacyclapentane. There were no split transitions reported for 1-fluoro-1-silacyclapentane.

This provides support for the idea that the large D_k vale is accounting for the unresolved

split transitions found in the spectra.

Table 5. Comparison of rotational and centrifugal distortion constants, in MHz, between 1,1-difluorosilacyclapent-2-ene and 1-fluoro-1-silacyclapentane for the parent species.

Constant	1,1-difluorosilacyclapent-2-ene	1-fluoro-1-silacyclapentane
A	3598.8869 (29)	4700.2018(6)
B	1762.2759 (72)	2368.4634(7)
C	1674.7317 (79)	1903.5467(5)
D_j	0.000144 (13)	0.000727(11)
D_{jk}	0.00201 (44)	-0.002770(37)
D_k	-0.10382 (36)	0.006121(57)
d_j	-	0.000023(8)
d_k	-	0.000146(126)

Further comparison between 1,1-difluorosilacyclapent-2-ene and 1-fluoro-1-

silacyclopentane can be performed by comparing the heavy atom substitution structure.

The Si – C bond lengths observed for 1-fluoro-1-silacyclapentane were 1.875Å and

1.841Å, while the respective analogous bonds for 1,1-difluorosilacyclapent-2-ene were

1.855Å and 1.840Å. It is likely that the additional fluorine on the silicon is responsible

for shortening these bonds. Comparing the C-C bond lengths for 1-fluoro-1-

silacyclopentane were 1.568Å and 1.535Å long while the respective analogous bonds for 1,1-difluorosilacyclapent-2-ene were 1.495Å and 1.569Å long. The difference in these bond lengths is likely due to the additional double bond in 1,1-difluorosilacyclapent-2-ene.

Further comparison between structures is possible through the use of second moments [155]. The second moment values for 1,1-difluorosilacyclapent-2-ene and 1-fluro-1-silacyclapentane can be found in tables 6 and 7 respectively. Comparing the P_{aa} and P_{cc} values is not useful as 1,1-difluorosilacyclapent-2-ene will inherently have larger values as it contains an extra fluorine along the a and c axes. P_{bb}, however, is a useful value to compare the planarity between the rings. From Tables 6 and 7 it can be seen that P_{bb} for 1,1-difluorosilacyclapent-2-ene and 1-fluoro-1-silacyclapentane are 77.708648 and 79.818879 respectively. As can be seen in Figure 4, P_{bb}, which is measuring the amount of mass on the b axis, is a measure of how planar the molecule is. Because the molecules have similar values for P_{bb} then it can be concluded that the molecules are of similar planarity. The differences in these values can likely be attributed to the fact that 1-fluoro-1-silacyclapentane has 2 additional hydrogen atoms along this axis.

Table 6. Second moment values for 1,1-Difluorosilacyclapent-2-ene.

Second Moment	Value	Error
P_{aa}	224.058503	0.000094
P_{bb}	77.708648	0.000094
P_{cc}	62.717827	0.000094

Table 7. Second moment values for 1-fluoro-1-silacyclapentane.

Second Moment	Value	Error
P_{aa}	185.674479	0.000048
P_{bb}	79.818879	0.000048
P_{cc}	27.703952	0.000048

5. CONCLUSIONS

The microwave spectrum of 1,1-difluorosilacyclapent-2-ene has been observed and analyzed. Isotopologues for the complete heavy atom substitution structure have been observed, assigned, and reported. The spectra was predominantly b-type with some a-type transitions, where a-type were the most intense. These spectra were successfully assigned using computational predications that utilized B3LYP/def2TZVP basis set with the GD3BJ Grimme dispersion. Spectral analysis yielded a structure in near complete agreement with the predicted structure. There exists a yet unexplained molecular motion causing split transitions and abnormal values in the assignment. Further experiments and quantum chemical calculations are required to further explain these split transitions and their origin.

REFERENCES

1. Marshall, F. E.; Gillcrist, D. J.; Persinger, T. D.; Jaeger, S.; Hurley, C. C.; Shreve, N. E.; Moon, N.; Grubbs, G. S. II. The CP-FTMW Spectrum of Bromoperfluoroacetone. *J. Mol. Spectrosc.*, **2016**, *328*, 59-66

2. Marshall, F. E.; Neill, J. L.; Muckle, M. T.; Pate, B. H.; Kisiel, Z.; Grubbs, G. S. II. Observation of ^{36}ArH^{37}Cl, ^{38}ArH^{35}Cl, and ^{38}ArH^{37}Cl in Natural Abundance Using CP-FTMW Spectroscopy. *J. Mol. Spectrosc.*, **2018**, *344*, 34-38

3. Frank E. Marshall; Rachel Dorris; Sean A. Peebles; Rebecca A. Peebles; G. S. Grubbs II. Microwave spectra and structure of Ar-1,3-difluorobenzene. *Journal of Physical Chemistry A*. **122** (2018) 7385. DOI: 10.1021/acs.jpca.8b05282

4. Frisch, M. J.; Trucks, G. W.; Schlegel, H. B.; Scuseria, G. E.; Robb, M. A.; Cheeseman, J. R.; Scalmani, G.; Barone, V.; Mennucci, B.; Petersson, G. A., et al.; Gaussian 09, Revision C.01; Gaussian, Inc.: Wallingford, CT, **2010**

5. Grimme, S; Steinmetz, M. Effects of London dispersion correction in density functional theory on the structure of organic molecules in the gas phase. *Phys.Chem. Chem. Phys.,* 2013, **15**, 16031

6. Pickett, H. M. The Fitting and Prediction of Vibration-Rotation Spectra with Spin Interactions. *J. Mol. Spectrosc.*, **1991**, *148*, 371-377

7. Kisiel, Z.; Pszczołkowski, L.; Medvedev, I. R.; Winnewisser, M.; De Lucia, F. C.; Herbst, E. Rotational Spectrum of Trans-Trans Diethyl Ether in the Ground and Three Excited Vibrational States. *J. Mol. Spectrosc.*, **2005**, *233*, 231-243

8. Costain, C. C. Further Comments on the Accuracy of r_s Substitution Structures. *Trans. Am. Crystallogr. Assoc.*, **1966**, *2*, 157

9. Institute of Physics, Polish Academy of Sciences Al.Lotnikow 32/46, Warszawa, POLAND, kisiel@ifpan.edu.pl, http://info.ifpan.edu.pl/~kisiel/prospe.htm

10. Z.Kisiel, in: J.Demaison et al. (Eds.), Spectroscopy from Space, Kluwer Academic Publishers, Dordrecht, 2001, pp.91-106

11. Haynes, W. M. (2009). *CRC handbook of chemistry and physics: A ready-reference book of chemical and physical data*. Boca Raton: CRC Press.

12. James R. Durig; Savitha S. Panikar; Daniel A. Obenchain; Brandon J. Bills; Patrick M. Lohan; Rebecca A. Peebles; Sean A. Peebles; Peter Groner; Gamil A. Guirgis; Michael D. Johnston. J Chem. Phys. 136, 044306 (2012); https://doi.org/10.1063/1.3673889 Submitted: 03 September 2011

13. R. K. Bohn, J. A. Montgomery, Jr., H. H. Michels, J. A. Fournier, J. Mol. Spectrosc. 325, June 2016

V. THE ROTATIONAL SPECTRUM AND COMPLETE HEAVY ATOM STRUCTURE OF THE CHIRAL MOLECULE VERBENONE

ABSTRACT

As the first step of a two-part chiral tagging experiment, the spectrum and subsequent isotopologue analysis on the heavy atoms of (1S)-(-)-Verbenone is presented. The spectrum has been recorded up to 69 GHz on three spectrom- eters, one CP-FTMW spectrometer from the University of Virginia functional from 2-8 GHz, a CP-FTMW spectrometer operational in the 6-18 GHz range located at the Missouri University of Science and Technology, and a Stark- modulated spectrometer operational from 48-72 GHz. 1250 transitions have been assigned to the parent and isotopologues for the predominantly b-type spectrum. Rotational constants and quartic centrifugal distortion constants have been determined for the parent species while for the 11 isotopologues only rotational constants have been determined. A Kraitchman analysis has been performed and the resulting coordinates are reported. The experimental heavy-atom structure has been compared to previously studied bicyclic terpenes and the computational structure and is found to be in excellent agreement with both, showing reliability of the theoretical approaches needed for the future chiral tagging work.

1. INTRODUCTION

Chirality is one of the most fundamental aspects of geometric molecular structure, yet one of the hardest aspects of the structure to accurately measure. Recent work in broadband rotational spectroscopy techniques, however, has shown that chirped pulse methods can be harnessed for the qualitative and quantitative distinction of chiral species in racemic mixtures [156, 157, 158, 159]. These, furthermore, can lend some insight into one of the most difficult of chirality measurements, enantiomeric excess (EE).

One recent advancement in accurately determining EE is the process of chiral tagging [160, 161]. Chiral tagging involves using a quantitatively known chiral molecule, binding that molecule through a van der Waals interaction to an unspecified chiral species, and utilizing the conformational differences in the diastereomer complexes. The resulting broadband microwave spectrum can then be used as a way of quantifying EE in both the purely racemic and enantioselective limits. This takes advantage of the high resolution and correct intensity functionality of the technique [162, 163] while avoiding the need for 3-wave mixing techniques and has the potential to be completely theory driven. Proof of principle for this technique, however, involves a thorough structural understanding of the system in question. For these experiments, verbenone was chosen as the structure of unspecified chirality because there had not been a full substitution structure study performed on the molecule.

In addition to being a chiral molecule, verbenone is also a monoterpene. Several similar terpenoids have been studied recently by rotational spectroscopic techniques with splitting in the spectra arising from various motions within the molecules [156, 164, 165,

166, 167, 168, 169, 170, 171, 172]. Our work on verbenone also set out to further understand if any of these internal motions were present in verbenone as well as determine the heavy atom structure of the molecule.

In this work, therefore, we present the first experimental heavy atom structure determination of verbenone using rotational spectroscopy. This structure is compared to the theoretical structure predicted by specialized DFT calculations intended for use in chiral tagging measurements in order to determine the reliability of these methodologies. Furthermore, this structure will lay the groundwork for chiral tagging experiments to be performed with verbenone.

2. QUANTUM CHEMICAL CALCULATIONS

Geometry optimizations were performed with Gaussian09, Revision E.01 [173] at the B3LYP D3BJ level with a def2-TZVP basis set [174, 175, 176]. This particular method and basis set were chosen for reasons that we will briefly highlight, but is based on the work of Grimme and coworkers [177]. First of all, since this molecule was studied as a precursor to complexation with a second chiral molecule as explained above, it is extremely important to have a highly accurate structure while also preserving computational expense. As shown by Grimme and coworkers [177], the typical methods of MP2 and DFT (B3LYP here) have pitfalls in the medium and long-range effects where the structures provided are either too compact (MP2) or too overly repulsive (DFT methods). Grimme's work shows that B2PLYP D3 has the most accurate results but has about the same computational expense as MP2. To get the structure quickly and

accurately, the authors have found that B3LYP D3BJ gives a quality structure for approximately the same computational expense as B3LYP, so this method was chosen. For basis set selection, the best performance in monomers comes with 6-311++G(d,p) [178, 179, 180], but the def2-TZVP [176] basis set gives better complex structures so def2-TZVP was chosen for comparison before and after complexation (chiral tagging). The resulting equilibrium structure is presented in Figure 1 with atomic labels and the quantitative structural parameters are presented in Table 1. The calculated structure predicts dipole moments of 1.00, 4.26, and 0.57 D along the *a*-, *b*-, and *c*-axes, respectively.
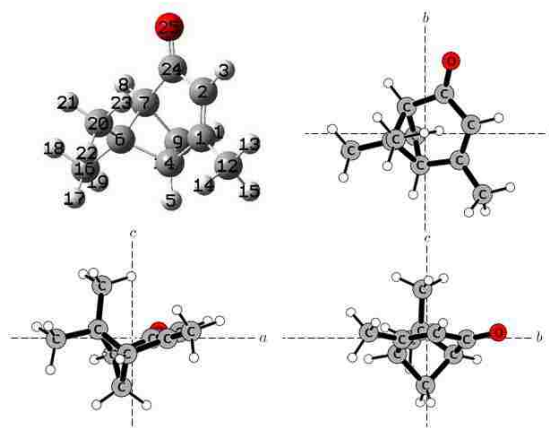
Figure 1. The calculated (see text for details) structure of verbenone showing all heavy-atom labeling and the structure in the *ab-, ac-,* and *bc-* planes.

Structurally, verbenone is calculated to be a double-ring structure with two methyl groups coming off the carbon labelled atom 6 and one methyl group coming off the carbon labelled atom 1 (see Figure 1). Off of the carbon labelled atom 24, there is an oxygen atom which completes the heavy atom structure. This structure has been

quantified in the principal axis system and is presented in Table 2. Verifying the

experimental accuracy of this structure is the focus of this work.

Table 1. Structural parameters and dipole moments from the quantum chemical
calculations of verbenone performed at the B3LYP D3Bj / def2-TZVP level.

Parameter	Value
A / MHz	1344
B / MHz	1216
C / MHz	899
D_J / kHz	0.060
D_{JK} / kHz	0.0046
D_K / kHz	-0.042
d_1 / kHz	0.00099
d_2 / kHz	-0.00032
P_{aa} / uÅ^2	301.0
P_{bb} / uÅ^2	261.4
P_{cc} / uÅ^2	114.7
Δ^c / uÅ^2	-229.3
κ^d	0.425
$|\mu_a|$ /D	1.00
$|\mu_b|$ /D	4.26
$|\mu_c|$ /D	0.57

3. EXPERIMENT

Three spectrometers were used for the acquisition of spectra, a 6-18 GHz CP-

FTMW spectrometer located at the Missouri University of Science and Technology

(MST), a 2-8 GHz CP-FTMW spectrometer located at the University of Virginia (UVa),

and a free jet Stark-modulated spectrometer operational from 48-72 GHz at Monash

University. The details of each of these spectrometers have been reported elsewhere

[181,182,183,184]. The CP-FTMW setups utilize fast linear frequency sweeps created on

an arbitrary waveform generator to create chirped pulses of microwaves on scales <10 µs.

These signals are power amplified and broadcast onto the molecules undergoing

supersonic expansion in a molecular beam. The instrument at UVa utilized four such

beams in one acquisition while the experiment at Missouri S&T used only one. In the

Monash setup, solid-state sweep oscillators rather than klystron sources were used to

provide improved frequency agility. The radiation source is a YIG-tuned microwave

oscillator which produces frequencies in the range of 12-18 GHz, with a frequency

quadrupler used to generate the 48-72 GHz frequency range accessible with the

spectrometer. The oscillator is phase-locked to a synthesiser that is referenced to a 5 MHz

laboratory frequency standard, allowing frequency measurements accurate to within 1

part in 10^8.The Stark modulation was then provided at 33 kHz between parallel-plate

electrodes separated by ~3.5 cm. Up to 1500 V cm^{-1} electric fields were used to

maximize the degree of Stark modulation.

(1S)-(-)-Verbenone (≥93%) was purchased from Sigma-Aldrich and was used

without further purification. All techniques implemented heating the sample to increase

volatility, but did so in different manners. At MST, the sample was heated to 80°C (353

K) approximately 1 m in front of the nozzle in a glass ``U"-shaped tube using a Variac

and heating tape. Argon gas was bubbled through the heated verbenone at pressures of 6-

10 psi and introduced to the instrument through a Parker-Hannifin Series 9 solenoid valve

with 0.8 mm orifice. At UVa, the sample was heated to 65°C (338 K) inside each of the

nozzles with a heating apparatus similar to that used in reference [185]. The setup at UVa

utilized a neon carrier gas held at approximately 10 psig. 1 million FID averages were

collected for each setup. Typical linewidths were ~60 kHz for the CP-FTMW

spectrometers. The Monash setup heated the sample to 80°C (353 K) into a stream of Ar

at a pressure of 30 kPa. Sample was introduced through a 350 μm diameter nozzle held at

10°C above the vaporization temperature producing rotational temperatures ~10 K. The typical linewidths for these spectra were 300-400 kHz. In some instances, linewidths for the Stark-modulated spectrometer were very large to give accurate line centers. In those instances, the attributed uncertainty was set to a value greater than 1 MHz, effectively weighting those transitions in the fit less than the more certain ones

Table 2. Optimized structure of verbenone in principal axis system.

Atom-Label Number	a-coordinate / Å	b-coordinate / Å	c-coordinate / Å
Carbon-1	1.201	-0.935	-0.030
Carbon-2	1.618	0.321	0.195
Hydrogen-3	2.602	0.565	0.573
Carbon-4	-0.201	-1.111	-0.559
Hydrogen-5	-0.451	-2.157	-0.741
Carbon-6	-1.217	-0.250	0.288
Carbon-7	-0.682	0.952	-0.575
Hydrogen-8	-1.337	1.801	-0.759
Carbon-9	-0.393	-0.076	-1.704
Hydrogen-10	-1.262	-0.272	-2.325
Hydrogen-11	0.473	0.110	-2.336
Carbon-12	2.027	-2.150	0.222
Hydrogen-13	3.023	-1.898	0.584
Hydrogen-14	1.538	-2.793	0.960
Hydrogen-15	2.124	-2.746	-0.691
Carbon-16	-2.669	-0.590	-0.042
Hydrogen-17	-2.940	-1.551	0.403
Hydrogen-18	-3.334	0.167	0.378
Hydrogen-19	-2.867	-0.651	-1.110
Carbon-20	-1.071	-0.190	1.802
Hydrogen-21	-1.728	0.584	2.206
Hydrogen-22	-1.371	-1.141	2.249
Hydrogen-23	-0.058	0.033	2.126
Carbon-24	0.657	1.420	-0.024
Oxygen-25	0.899	2.585	0.225

[a] Optimized structure performed at the B3LYP D3BJ/def2-TZVP level of theory. See text for details

4. RESULTS AND ANALYSIS

The resulting spectra from the CP-FTMW spectrometers are located in Figure 2. Due to the predicted large value of the *b*-component of the dipole moment, assignment was started with *b*-type, R-branch transitions. *a*-type and *c*-type, R-branch transitions were also observed, but with much weaker signal intensity. This was in accordance to their predicted dipole moment values. In addition, a number of *b*-type, Q-branch spectra were observed. Transitions were given an attributed uncertainty of 10 kHz for the CP-FTMW transitions and 10% of the transition linewidth was the attributed uncertainty for the Stark-modulated spectrometer. In total, 633 transitions were assigned to the parent isotopologue between 2-69 GHz. Signal intensity arising from UVa data ($\geq$5000 S:N ratio on some transitions) allowed for the observation of isotopologues consisting of one atom substitution at each heavy atom position in natural abundance, including ^{18}O species. A typical signal intensity profile for these transitions are presented in Figure 3. No splitting arising from internal motion or spin-spin hyperfine due to hydrogen atoms were observed in the spectra, different from other known monoterpenes. This is supported by the CP-FTMW spectral linewidths being on the order of unsplit spectra and only a semi-rigid Hamiltonian being needed for an adequate fit (see below). Assignments were made for these minor isotopologues by using a simple mass substitution into the calculated structure, predicting the rotational constants, and multiplying these constants by the ratio of the experimental parent values to those of the calculated structure.

Spectral fits were performed using Pickett's SPFIT/SPCAT program suite [186] in conjunction with Kisiel's AABS package [187]. The fitted parameters can be found in

Table 3. Spectra were fit using a Watson-S Hamiltonian [188] in the I^r representation. In total, 1250 transitions were assigned to 12 different isotopologues with a minimum of 25 transitions assigned for each species. Rotational constants *A*, *B*, and *C* were determined for each isotopologue while all quartic centrifugal distortion constants were determined for the parent. Centrifugal distortion constants for the minor isotopologues were held to the parent values. All microwave RMS values were in good agreement with the attributed measurement uncertainty as evidenced by pure fit RMS values at or below 1.0 for all species. All transition quantum number assignments can be found in the Supplemental Material along with the Pickett input files for the parent species.
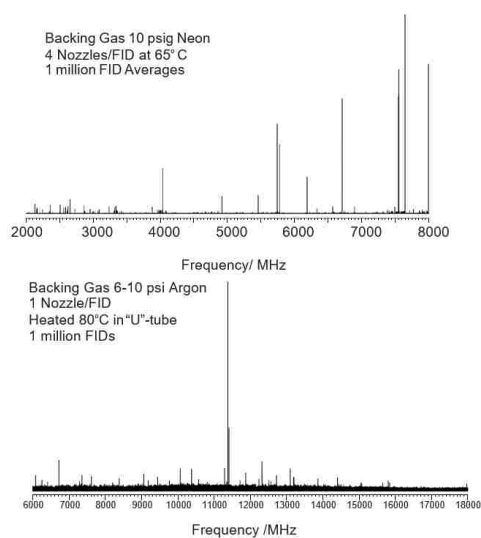
Figure 2. Spectrum of verbenone taken from 2-8 GHz taken at UVa (top) and 6-18 GHz at MST (bottom). Signal-to-noise of the 2-8 GHz spectrum allowed for the observation of all singly-substituted heavy atom isotopologues.
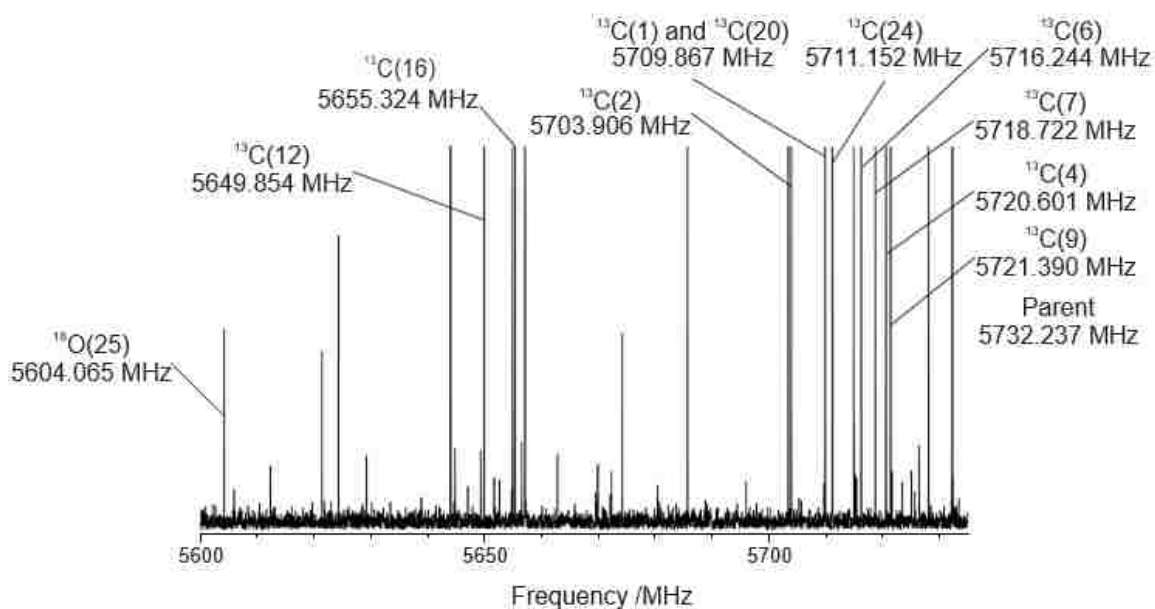
Figure 3. A zoom-in of the UVa spectra from 5600-5735 MHz. The $J'_{Ka,Kc} - J''_{KaKc} = 3_{03} - 2_{12}$ transitions are labeled to show the intensity of the minor isotopologues in natural abundance. Numbers in parentheses represent atomic number labeling from Figure 1. The 18O isotopologue has at least a 10:1 S:N ratio and the 13C species are all too intense at this level to observe their profile maximums.

Holding the centrifugal distortion constants for the minor isotopologues to the parent value should be addressed. While performing the fits, it was noticed that the size of the centrifugal constants were all very small (especially D_j) as they typically are with heavy monomer species. This created problems when fitting the minor isotopologues where some fits would cause D_j to be a negative value. Although there is precedent for negative values in D_j, they are rare and inconsistent with the fitted parent value containing over 600 transitions. Although this did not happen with all of the minor isotopologues, for consistency in making accurate structural arguments using these parameters, it was deemed best to hold all centrifugal distortion constants to the values determined for the parent. This, in all cases, had little-to-no effect on the fit RMS which

provided more evidence that the other fits with negative D_j values were probably

anomalies and that holding the centrifugal distortion terms was the right choice.

Table 3. Spectroscopic parameters of all observed isotopologues of verbenone.

Parameter	Parent	^{13}C(1)[a]	^{13}C(2)	^{13}C(4)	^{13}C(6)	^{13}C(7)
A / MHz	1338.4458(1)[b]	1335.6326(4)	1337.9376(3)	1332.9562(3)	1337.9400(3)	1334.2553(2)
B / MHz	1212.0286(1)	1207.6719(3)	1204.3764(3)	1211.1104(3)	1207.6192(3)	1209.6121(2)
C / MHz	895.8775(1)	892.2416(3)	891.5788(3)	893.8687(3)	893.4694(3)	893.7174(2)
D_J / kHz	0.04897(9)	[0.04897][c]	[0.04897]	[0.04897]	[0.04897]	[0.04897]
D_{JK} / kHz	0.0470(1)	[0.0470]	[0.0470]	[0.0470]	[0.0470]	[0.0470]
D_K / kHz	-0.0454(2)	[-0.0454]	[-0.0454]	[-0.0454]	[-0.0454]	[-0.0454]
d_1 / kHz	-0.00893(3)	[-0.00893]	[-0.00893]	[-0.00893]	[-0.00893]	[-0.00893]
d_2 / kHz	0.00368(2)	[0.00368]	[0.00368]	[0.00368]	[0.00368]	[0.00368]
N[d]	633	57	71	73	83	51
RMS[e] / kHz	25.4[f]	10.6	9.3	10.8	8.9	5.5
Parameter	^{13}C(9)	^{13}C(12)	^{13}C(16)	^{13}C(20)	^{13}C(24)	^{18}O(25)
A / MHz	1328.2245(2)	1324.3619(2)	1337.1963(1)	1326.9746(2)	1331.3406(2)	1294.4149(3)
B / MHz	1203.2157(2)	1198.1496(2)	1191.7363(1)	1199.4878(2)	1210.8618(2)	1205.7917(4)
C / MHz	895.6290(1)	882.1853(2)	884.1932(1)	894.0249(1)	892.0564(2)	872.9259(3)
D_J / kHz	[0.04897]	[0.04897]	[0.04897]	[0.04897]	[0.04897]	[0.04897]
D_{JK} / kHz	[0.0470]	[0.0470]	[0.0470]	[0.0470]	[0.0470]	[0.0470]
D_K / kHz	[-0.0454]	[-0.0454]	[-0.0454]	[-0.0454]	[-0.0454]	[-0.0454]
d_1 / kHz	[-0.00893]	[-0.00893]	[-0.00893]	[-0.00893]	[-0.00893]	[-0.00893]
d_2 / kHz	[0.00368]	[0.00368]	[0.00368]	[0.00368]	[0.00368]	[0.00368]
N	44	54	59	50	50	25
RMS / kHz	5.3	6.7	5.1	5.7	5.3	7.2

[a] Number in parentheses in name represents atomic label from Figure 1.

[b] Numbers in parentheses give standard errors (1σ, 67% confidence level) in units of the least significant figure.

[c] Number in brackets have been held to the parent value. See text for details.

[d] Number of observed transitions used in the fit.

[e] RMS is the microwave RMS defined as $\sqrt{\dfrac{(obs-calc)^2}{N}}$.

[f] Using line center accuracy and weighting described in the text, pure RMS was 0.93.

5. DISCUSSION

5.1. EXPERIMENTAL STRUCTURE AND COMPARISON TO THEORY

As mentioned in the Introduction, verbenone's chiral structure and strong monomer signal makes it a good candidate for chiral tagging measurements. Because of this, verbenone has also been used in subsequent chiral tagging studies with 3-butyn-2-ol to determine an experimental EE of the sample [161]. Typically, chiral information is lost in the Fourier transformation step of the broadband experiment. It has been shown, however, that broadband rotational spectroscopy can be used in a 3-wave mixing scheme to determine EEs utilizing the observed molecular time-domain FID (before Fourier transformation) [156, 157, 158, 159]. The problem is that this setup calls for an adjustment to the typical broadband setup. The chiral tagging process eliminates this by taking advantage of the information naturally generated from all Fourier transform microwave techniques, structure. Since these species are structurally different, their rotational spectra are different. Instead of FID information, this technique takes advantage of the correct intensity profiles of Fourier transformed frequency data to be quantitative [162, 163]. The percentages determined have no theoretical enantiopurity limit because, again, the spectra are a consequence of structural isomers. However, there is a practical limit due to instrument sensitivity from detecting the van der Waals-created diastereomers as the signal must be above the noise floor.

For these initial experiments, a complete experimental structure was needed to further calibrate the tagging procedure and provide a reference point for minor isotopologue species of the monomer. Table 4 presents the experimentally determined

Kraitchman [189] coordinates of the heavy-atoms reported with Costain errors [190]. Comparing these values to those provided by theory (Tables 2 and 6) shows that most of the optimized heavy-atom positions are within the uncertainty of the experimental measurement.

In addition to the r_s structure, second moments, inertial defects, and Ray's asymmetry parameter [191] for each isotopologue were determined as both an extra validation of the structure and transition assignments. These are presented in Table 5. Since there was only one substitution structure at each heavy-atom position, these parameters provide a better quantitative structural comparison between isotopologues than rotational constant determination as these structural parameters should be, within reason, relatively invariant to these mass substitutions and can be, if needed, strong evidence of molecular structure where there is no isotopic substitution information [192]. If one of these values, therefore, happened to be well outside agreement with the others, then the outlier fit could be looked at and edited to give a more credible result. Furthermore, second moment values, in conjunction with a quality calculation, can be used as a double-check of atomic labeling of the fits as isotopic substitution of the atoms furthest predicted out-of-planes will have the largest effect on their respective P_{ii} value. The largest changes in these parameters lie with ^{13}C-9, ^{13}C-16, ^{13}C-20, and ^{18}O-25 and are shown by the calculation to be the farthest from the center of mass.

The last thing considered was the accuracy of the quantum chemical calculations from a quantitative perspective. Again, this work utilized a B3LYP D3BJ/def2-TZVP level of theory due to previous success it has had with quickly and accurately determining

Table 4. Experimentally determined Kraitchman coordinates of each heavy atom in verbenone.

Atom-Label Number	a-coordinate / Å	b-coordinate / Å	c-coordinate / Å
Carbon-1	1.216(1)[a]	-0.910(2)[b]	-0.02(8)
Carbon-2	1.6168(9)	0.338(4)	0.193(8)
Carbon-4	-0.12(1)	-1.120(1)	-0.553(3)
Carbon-6	-1.205(1)	-0.270(6)	0.271(6)
Carbon-7	-0.704(2)	0.933(2)	-0.576(3)
Carbon-9	-0.388(4)	-0.06(2)	-1.7070(9)
Carbon-12	2.0775(7)	-2.1134(7)	0.218(7)
Carbon-16	-2.6572(6)	-0.647(2)	0.00(5)[c]
Carbon-20	-1.056(1)	-0.193(8)	1.8051(8)
Carbon-24	0.618(2)	1.429(1)	-0.02(9)
Oxygen-25	0.841(2)	2.6052(6)	0.216(7)

[a] Number in parentheses represent Costain errors[190] in units of the least significant figure.

[b] Negative sign on coordinates taken from the calculate atom locations.

[c] Kraitchman analysis rendered an imaginary number which has been reported as a value of 0 to the precision of the uncertainty.

Table 5. Second moments, inertial defects, and Ray's asymmetry parameters of all observed isotopologues of verbenone.

Parameter	Parent	$^{13}C(1)$[a]	$^{13}C(2)$	$^{13}C(4)$	$^{13}C(6)$	$^{13}C(7)$
P_{aa} / u$Å^2$	301.74964(4)[b]	303.2535(1)	304.3625(1)	301.7641(1)	303.1997(1)	302.25493(8)
P_{bb} / u$Å^2$	262.36656(4)	263.1615(1)	262.4736(1)	263.6199(1)	262.4369(1)	263.22473(8)
P_{cc} / u$Å^2$	115.21990(4)	115.2203(1)	115.2563(1)	115.5216(1)	115.2923(1)	115.54761(8)
Δ^c / u$Å^2$	-230.43980(8)	-230.4405(2)	-230.5126(2)	-231.0432(2)	-230.5846(2)	-231.0952(2)
κ^d	0.428711	0.422809	0.401552	0.445004	0.413591	0.434132
Parameter	$^{13}C(9)$	$^{13}C(12)$	$^{13}C(16)$	$^{13}C(20)$	$^{13}C(24)$	$^{18}O(25)$
P_{aa} / u$Å^2$	301.90208(6)	306.53471(8)	308.85050(4)	302.88181(6)	302.15116(8)	303.8221(1)
P_{bb} / u$Å^2$	262.37063(6)	266.33701(8)	262.72029(4)	262.40335(6)	264.38141(8)	275.1263(1)
P_{cc} / u$Å^2$	118.12153(6)	115.26488(8)	115.21899(4)	118.44720(6)	115.22018(8)	115.3042(1)
Δ^c / u$Å^2$	-236.2431(1)	-230.5298(2)	-230.43798(8)	-236.8944(1)	-230.4404(2)	-230.6084(3)
κ^d	0.422052	0.429132	0.357797	0.411078	0.451477	0.579476

[a] Number in parentheses in name represents atomic label from Figure 1.

[b] Numbers in parentheses give standard errors (1σ, 67% confidence level) in units of the least significant figure.

[c] Inertial defect defined as $I_c - I_a - I_b$.

[d] Ray's asymmetry parameter. This value is unitless and is defined as $\kappa = \frac{(2B-A-C)}{A-C}$

optimized monomer and dimer structures. It has already been shown in this work that the

calculated dipole moments were an accurate reflection of the distribution of observed

transitions and there is excellent agreement between the heavy atom positions and the

calculated heavy-atom positions. However this work could not, unfortunately, determine

substitution at every position in natural abundance. For this, we looked at the percent

differences between the calculated and experimental values on the rotational constants.

These values were -0.41%, -0.32%, and -0.31% for A, B, and C, respectively, reiterating

the excellent agreement between theory and experiment.

In light of all of this evidence, the authors conclude that the r_s experimental

structure is so close to the optimized r_e that the two are virtually identical with regards to

the heavy-atom positions in the molecule and Figure 1 can be taken as the experimental

structure. Being able to calculate structures this accurately at least for the monomer lays

some of the groundwork for the theoretically-driven chiral tagging experiments.

5.2 STRUCTURAL COMPARISON TO OTHER BICYCLIC MONOTERPENES

All bond lengths and bond angles for verbenone have been determined and are

compared to the calculated structure and similar bicyclic monoterpenes nopinone [164],

camphor [171], and fenchone [165] in Table 6. Due to possible problems with the r_s

structure presented in these previous studies, a r_0 structure of verbenone was undertaken

using Kisiel's STRFIT program [193] in order to make direct comparisons. All systems

were also put in a similar heavy-atom labelling system. The closest species studied to

date is nopinone with the only difference being a missing methyl group and verbenone

possessing a double bond between the carbons labelled 3 and 4. This is very apparent

with the C_4-C_3 bond length being 1.343(47) Å for verbenone and 1.546(6) Å for nopinone. This double bond is also apparent in the $C_5\$C_4\$C_3$ and $C_4C_3C_2$ bond angles which are 117.1(19)° and 118.0(18)°, respectively, very close to the expected 120° from a C-C sp^2 hybridized orbital. This is compared to the same angles in nopinone being 111.3(3)° and 114.1(2)° much closer to the expected 109.5° from a C-C sp^3 hybridized orbital.

One noticeable difference amongst the family of bicyclic monoterpenes presented is the ring strain upon going from a 1-4 linkage in camphor and fenchone to a 1-5 linkage in verbenone and nopinone. This is very apparent in the $C_1C_6C_5$ bond angle. This angle in camphor and fenchone is approximately 95°. This is already a strained molecular structure from the ideal 109.5°, but only off by 15°. When the 1-5 linkage is made, this angle tightens considerably to 85-86° for verbenone and nopinone, almost 25° off of ideal. This ring strain seems to be repeated in the $C_5C_7C_1$, $C_7C_1C_6$, and $C_7C_5C_6$ bond angles of verbenone showing that the four membered ring component of the bicyclic monoterpene is even more hindered sterically than those of cyclobutane.

6. CONCLUSIONS

The CP-FTMW spectrum of (1S)-(-)-Verbenone has been reported as a first step in a two-part chiral tagging experiment. The transition intensities of the singularly-substituted minor isotopologues of the heavy atoms in the molecule are easily observed in natural abundance allowing for a fully determined heavy-atom structure to be reported for

the first time. This structure has been compared to theoretical methods that have been

shown to quickly and accurately determine structural parameters, i.e. rotational constants,

Table 6. Comparison of verbenone structural parameters to similar bicyclic terpenes. [a]

	Verbenone			Nopinone[9]	Camphor[16]	Fenchone[10]
	r_z	r_0	B3LYPD3BJ	r_0	r_0	r_0
$r(C_1-C_3)$ /Å	1.454(31)[b]	1.510(41)	1.509	1.542(7)	—	—
$r(C_1-C_{11})$ /Å	1.499(13)	1.496(26)	1.491	—	—	—
$r(C_1-C_2)$ /Å	1.328(14)	1.343(47)	1.342	1.546(6)	—	—
$r(C_2-C_3)$ /Å	1.494(13)	1.480(42)	1.476	1.535(7)	1.530(3)	1.535(31)
$r(C_3-C_4)$ /Å	1.518(33)	1.522(44)	1.522	1.501(11)	1.537(10)	1.526(29)
$r(C_3-C_7)$ /Å	1.538(13)	1.569(50)	1.554	1.561(6)	—	—
$r(C_3-C_4)$ /Å	1.5542(69)	1.565(40)	1.573	1.579(11)	1.522(4)	1.541(25)
$r(C_4-C_5)$ /Å	1.5432(61)	1.528(34)	1.522	1.528(12)	1.542(6)	—
$r(C_4-C_6)$ /Å	1.524(13)	1.538(24)	1.527	1.535(7)	1.534(5)	—
$r(C_4-C_5)$ /Å	1.606(11)	1.574(39)	1.578	1.553(9)	1.555(8)	1.552(8)
$r(C_7-C_5)$ /Å	1.590(14)	1.568(47)	1.555	1.551(10)	—	—
$r(C_1-O)$ /Å	1.220(17)	1.239(21)	1.216	1.214(4)	1.212(4)	1.214(5)
$\angle(C_{11}C_1C_1)$ /°	123.7(19)	124.1(17)	124.2	—	—	—
$\angle(C_1C_2C_3)$ /°	117.5(12)	118.0(18)	118.0	114.1(2)	—	—
$\angle(C_1C_2O)$ /°	123.6(24)	123.8(28)	123.6	121.4(6)	126.8(1)[c]	125.8(31)
$\angle(C_2C_1C_7)$ /°	107.5(22)	106.8(24)	107.6	108.7(5)	—	—
$\angle(C_4C_1C_4)$ /°	109.5(24)	109.8(22)	109.6	107.7(6)	100.6(3)	—
$\angle(C_1C_4C_5)$ /°	118.16(52)	118.3(29)	118.9	117.6(5)	113.2(4)	—
$\angle(C_1C_4C_5)$ /°	84.97(42)	85.3(18)	84.5	85.9(6)	94.5(4)	95.2(6)
$\angle(C_3C_4C_5)$ /°	106.3(19)	108.1(20)	108.4	108.7(6)	107.5(3)	—
$\angle(C_4C_5C_5)$ /°	118.12(59)	120.1(24)	119.6	119.9(8)	113.7(5)	—
$\angle(C_6C_4C_5)$ /°	114.9(13)	111.9(24)	112.0	112.1(6)	113.7(5)	—
$\angle(C_5C_4C_4)$ /°	110.9(22)	110.1(17)	110.3	111.1(5)	102.6(2)	—
$\angle(C_5C_4C_5)$ /°	118.2(12)	117.1(19)	117.2	111.3(3)	—	—
$\angle(C_5C_4C_{11})$ /°	118.1(11)	118.8(18)	117.2	—	—	—
$\angle(OC_2C_3)$ /°	123.0(14)	122.5(24)	123.0	123.6(6)	126.8(1)[c]	—
$\angle(C_5C_4C_5)$ /°	113.3(12)	113.7(19)	113.4	114.9(4)	—	—
$\angle(C_5C_4C_4)$ /°	109.0(21)	107.2(22)	107.2	108.7(5)	—	—
$\angle(C_1C_3C_4)$ /°	84.59(50)	87.2(22)	87.3	88.3(5)	—	—
$\angle(C_4C_4C_7)$ /°	88.12(62)	87.5(24)	87.5	87.1(5)	—	—
$\angle(C_4C_4C_5)$ /°	113.7(14)	111.7(23)	112.0	111.0(8)	114.1(6)	—
$\angle(C_5C_7C_5)$ /°	86.06(16)	85.3(13)	85.9	86.7(6)	—	—

[a] Atomic labels are made in the schematic graphic for each molecule.

[b] Numbers in parentheses give standard errors (1σ, 67% confidence level) in units of the least significant figure.

[c] ∠(C3C2O) =∠(OC2C1) in Ref. [171].

of midsize molecules (<500 amu). The agreement of the experimentally determined heavy atom positions to those of theory is excellent; additionally all theoretical rotational constants are within <0.5% error of the experimentally determined values. The authors have concluded that this excellent agreement between experiment and theory is so close that the calculated structure presented in Figure 1 can essentially be considered the experimental structure. The potential for performing chiral analysis of verbenone by attaching a smaller chiral tag molecule, then, is suggested by the high sensitivity of the verbenone monomer spectrum. In the case of the chiral tag measurement, the molecular size is not increased so significantly because verbenone is already a large molecule. As a result, reduction in the transition strength from an increased rotational partition function for the chiral complex may not prohibit sensitive detection of the tagged verbenone.

Previous studies of other monoterpenes, including verbenone, have been shown to have internal motions exhibited by transition splitting in the molecular spectra. No such splitting was observed for this species in any of the measurements made in this work. The combination of high frequency Stark-modulated spectra and high resolution CP-FTMW spectra allowed for accurate and precise rotational constants and centrifugal distortion constants needed for structure determination. The semirigid Hamiltonian fit used adequately represented the uncertainty attributed to the line centers for all instruments, suggesting no internal rotation unlike that seen in previous monoterpenes.

Structural comparisons to similar bicyclic monoterpenes nopinone, camphor, and fenchone showed that verbenone exhibits very similar characteristics to those systems already studied, but with steric constrictions due to the C-C double bond in the structure.

In addition, the four-membered ring in the molecule, like nopinone, exhibits a steric

hinderance larger than that of cyclobutane.

ACKNOWLEDGEMENTS

REFERENCES

1. V. A. Shubert, D. Schmitz, C. Medcraft, A. Krin, D. Patterson, J. M. Doyle, M. Schnell, J. Chem. Phys. 142 (2015)

2. V. A. Shubert, D. Schmitz, C. Pérez, C. Medcraft, A. Krin, S. R. Domingos, D. Patterson, M. Schnell, J. Phys. Chem. Lett. 7 (2016)

3. S. Lobsinger, C. Perez, L. Evangelisti, K. K. Lehmann, B. H. Pate, J. Phys. Chem. Lett. 6 (2015)

4. D. Patterson, M. Schnell, J. M. Doyle, Nature 497 (2013) 475

5. N. A. Seifert, C. Pérez, J. L. Neill, B. H. Pate, M. Vallejo-López, A. Lesarri, E. J. Cocinero, F. C. no, Phys. Chem. Chem. Phys. 17 (2015)

6. L. Evangelisti, K. J. Mayer, M. S. Holdren, T. Smart, C. West, B. Pate, G. Sedo, F. E. Marshall, G. S. Grubbs II, CHIRAL TAGGING OF VERBENONE WITH 3-BUTYN-2-OL FOR ESTABLISHING ABSOLUTE CONFIGURATION AND DETERMINING ENANTIOMERIC EXCESS, 72nd International Symposium on Molecular Spectroscopy, University of Illinois at Urbana-Champaign, IL, 2017, Accepted, Not Yet Designated a Time.

7. G. S. Grubbs II, C. T. Dewberry, K. C. Etchison, K. E. Kerr, S. A. Cooke, Rev. Scient. Instrum. 78 (2007)

8. G. G. Brown, B. C. Dian, K. O. Douglass, S. M. Geyer, S. T. Shipman, B. H. Pate, Rev. Scient. Instrum. 79 (2008)

9. E. M. Neeman, J.-R. Avilés-Moreno, T. R. Huet, Phys. Chem. Chem. Phys. 19 (2017)

10. D. Loru, M. Bermúdez, M. E. Sanz, J. Chem. Phys. 145 (2016)

11. J. R. A. Moreno, T. R. Huet, J. J. L. González, Struct. Chem. 24 (2013)

12. D. Schmitz, V. A. Shubert, B. M. Giuliano, M. Schnell, J. Chem. Phys. 141 (2014)

13. D. Schmitz, V. A. Shubert, T. Betz, M. Schnell, Front. Chem. 3 (2015)

14. H. V. L. Nguyen, H. Mouhib, S. Klahm, W. Stahl, I. Kleiner, Phys. Chem. Chem. Phys. 15 (2013)

15. J. R. A. Moreno, F. P. U. na, J. J. L. González, T. R. Huet, Chem. Phys. Lett. 473 (2009)

16. Z. Kisiel, O. Desyatnyk, E. Bialkowska-Jaworska, L. Pszczółkoski, Phys. Chem. Chem. Phys. 5 (2003)

17. E. M. Neeman, P. Dréan, T. R. Huet, J. Mol. Spectrosc. 322 (2016)

18. Gaussian 09, Revision E.01, M. J. Frisch, G. W. Trucks, H. B. Schlegel, G. E. Scuseria, M. A. Robb, J. R. Cheeseman, G. Scalmani, V. Barone, B. Mennucci, G. A. Petersson, H. Nakatsuji, M. Caricato, X. Li, H. P. Hratchian, A. F. Izmaylov, J. Bloino, G. Zheng, J. L. Sonnenberg, M. Hada, M. Ehara, K. Toyota, R. Fukuda, J. Hasegawa, M. Ishida, T. Nakajima, Y. Honda, O. Kitao, H. Nakai, T. Vreven, J. A. Montgomery, Jr., J. E. Peralta, F. Ogliaro, M. Bearpark, J. J. Heyd, E. Brothers, K. N. Kudin, V. N. Staroverov, R. Kobayashi, J. Normand, K. Raghavachari, A. Rendell, J. C. Burant, S. S. Iyengar, J. Tomasi, M. Cossi, N. Rega, J. M. Millam, M. Klene, J. E. Knox, J. B. Cross, V. Bakken, C. Adamo, J. Jaramillo, R. Gomperts, R. E. Stratmann, O. Yazyev, A. J. Austin, R. Cammi, C. Pomelli, J. W. Ochterski, R. L. Martin, K. Morokuma, V. G. Zakrzewski, G. A. Voth, P. Salvador, J. J. Dannenberg, S. Dapprich, A. D. Daniels, O¨. Farkas, J. B. Foresman, J. V. Ortiz, J. Cioslowski, and D. J. Fox, Gaussian 09, Gaussian, Inc., 340 Quinnipiac Street, Building 40, Wallingford, CT, 06492, 2015, copyright Qc 1994-2015.

19. P. J. Stephens, F. J. Devlin, C. F. Chabalowski, M. J. Frisch, J. Phys. Chem 98 (1994)

20. S. Grimme, S. Ehrlich, L. Goerigk, J. Comput. Chem. 32 (2011)

21. F. Weigend, R. Ahlrichs, Phys. Chem. Chem. Phys. 7 (2005)

22. S. Grimme, M. Steinmetz, Phys. Chem. Chem. Phys. 15 (2013)

23. R. Krishnan, J. S. Binkley, R. Seeger, J. A. Pople, J. Chem. Phys. 72 (1980)

24. M. N. Glukhovtsev, A. Pross, M. P. McGrath, L. Radom, J. Chem. Phys. 103 (1995)

25. L. A. Curtiss, M. P. McGrath, J.-P. Blandeau, N. E. Davis, R. C. Binning, Jr., L. Radom, J. Chem. Phys. 103 (1995)

26. F. E. Marshall, D. J. Gillcrist, T. D. Persinger, S. Jaeger, C. C. Hurley, N. E. Shreve, N. Moon, G. S. Grubbs II, J. Mol. Spectrosc. 328 (2016)

27. J. L. Neill, S. T. Shipman, L. Alvarez-Valtierra, A. Lesarri, Z. Kisiel, B. H. Pate, J. Mol. Spectrosc. 269 (2011)

28. C. P´erez, S. Lobsinger, N. A. Seifert, D. P. Zaleski, B. Temelso, G. C.Shields, Z. Kisiel, B. H. Pate, Chem. Phys. Lett. 571 (2013)

29. D. McNaughton, P. D. Godfrey, J.-U. Grabow, J. Mol. Spectrosc. 274 (2012)

30. R. D. Suenram, G. Y. Golubiatnikov, I. I. Leonov, J. T. Hougen, J. Ortigoso, I. Kleiner, G. T. Fraser, J. Mol. Spectrosc. 208 (2001)

31. H. M. Pickett, J. Mol. Spectrosc. 148 (1991) 371

32. Z. Kisiel, L. Pszcz´o-lkoski, I. R. Medvedev, M. Winnewisser, F. C. D.Lucia, C. E. Herbst, J. Mol. Spectrosc. 233 (2005) 231.

33. J. K. G. Watson, Vibrational Spectra and Structure 6 (1977)

34. J. Kraitchman, Am. J. Phys. 21 (1953)

35. C. C. Costain, Trans. Am. Crystallogr. Assoc. 2 (1966)

36. W. Gordy, R. L. Cook, Microwave Molecular Spectra; Techniques of Chemistry Vol. XVIII, Wiley, New York, 1984.

37. R. K. Bohn, J. A. Montgomery, Jr., H. H. Michels, J. A. Fournier, J. Mol. Spectrosc. 325 (2016)

38. Z. Kisiel, J. Mol. Spectrosc. 218 (2003) 58

VI. ROTATIONAL SPECTRA OF THE LOW ENERGY CONFORMERS OBSERVED IN THE (1R)-(-)-MYRTENOL MONOMER

ABSTRACT

The microwave spectrum of the chiral monoterpenol molecule, (1R)-(–)-myrtenol, has been observed using CP-FTMW spectroscopy in the 6-18 GHz region of the electromagnetic spectrum. Transitions linked to three conformers of the primary alcohol group were experimentally observed, while no conformers associated with changes to the bicyclic cage were detected. The most numerous and intense transitions correspond with the global minimum structure predicted by both Density Functional Theory (DFT) and ab initio calculations. The second moments of inertia predicted by DFT were found to agree very well with those determined experimentally for all three conformers. However, an empirical correction for dispersion was required for the DFT calculations before the energetic ordering of the conformers matched those predicted by ab initio calculations. This also placed the ordering in agreement with that suggested by the experimental spectrum.

1. INTRODUCTION

Volatile organic compounds (VOCs) are known to have a wide-ranging impact on the environment and public health [194]. Both anthropogenic [195] and, more broadly, biogenic [196] sources are known to play a role in the environmental VOC lifecycle. Among the most common biogenic sources are the volatile bioactive terpenes produced

by plant life [197, 198]. Myrtenol, as a member of this class, is known to be produced by coniferous vegetation, specifically the genus *Taxus* (yew) [199, 200]. As unsaturated hydrocarbons, terpenes can react with ozone and NO_x pollutants in the atmosphere to produce secondary organic aerosols or act as precursors for photochemical smog [201, 202] making the study of their gas phase properties of particular chemical interest.

In terms of their spectroscopy, bicyclic monoterpenes have been an area of rich investigation in the microwave region [203, 204, 205, 206, 207, 208, 209, 210]. Much of this work has focused on the gas phase structures of these molecules, partly due to their large and unique cage-like ring systems. More recently, however, the chiral centers of monoterpenes [203, 211] have been proposed as prototypical systems for advancing spectroscopic chiral tagging [212, 213] methods. As this interest extends into ever larger and more complex molecules, including those with multiple chiral centers, the methodology will need to incorporate conformational diversity to fully and accurately represent the systems of interest. To further this goal, the current work takes advantage of the high probability associated with finding low energy conformers in primary alcohols by investigating the pure rotational spectrum of the bicyclic monoterpenol molecule, myrtenol, for the first time.

2. EXPERIMENTAL METHODS AND RESULTS

All spectra were collected using the CP-FTMW spectrometer in operation at Missouri University of Science and Technology. The technical details of this instrument and a description of its operation have been previously reported [214, 215]. In the case of

myrtenol, the spectrum spanning 6 to 18 GHz was collected using 4 μs chirps of 6-12 and 12-18 GHz in two separate experiments. The resulting free induction decays (FIDs) were collected for 20 μs, resulting in typical linewidths (FWHM) between 60-100 kHz. The solenoid valve rate was 5 Hz with five FIDs collected per gas pulse. In total, 240k FIDs were averaged for each region. 95% (1R)-(–)-myrtenol was purchased from Sigma-Aldrich and used without alteration. A small sample of the liquid was placed in a recently constructed heated nozzle (Figure 1) adapted from the design of Suenram et al. [216] and heated to 70 °C. Designs for this nozzle can be supplied by the authors upon request. After heating to the operating temperature, 40 psig (2.8 bar, 275 kPa) of argon was used as a carrier gas to pulse the sample into the spectrometer. The resulting spectrum is shown in Figure 2.
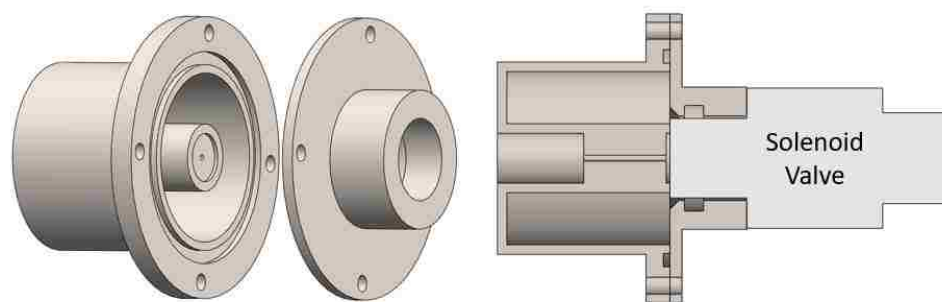
Figure 1. CAD image of the heated nozzle modified from Suenram et al [216].

Transitions of three distinct species, labelled Exp1 – Exp3, were observed in the spectrum. In the cases of Exp1 and Exp3, all three (*a*-, *b*-, and *c*-) types of rotational transitions were assigned. While in Exp2, only *a*- and *b*-type transitions were assigned, as no *c*-type transitions were observed. In all cases, the *a*-type transition intensities were
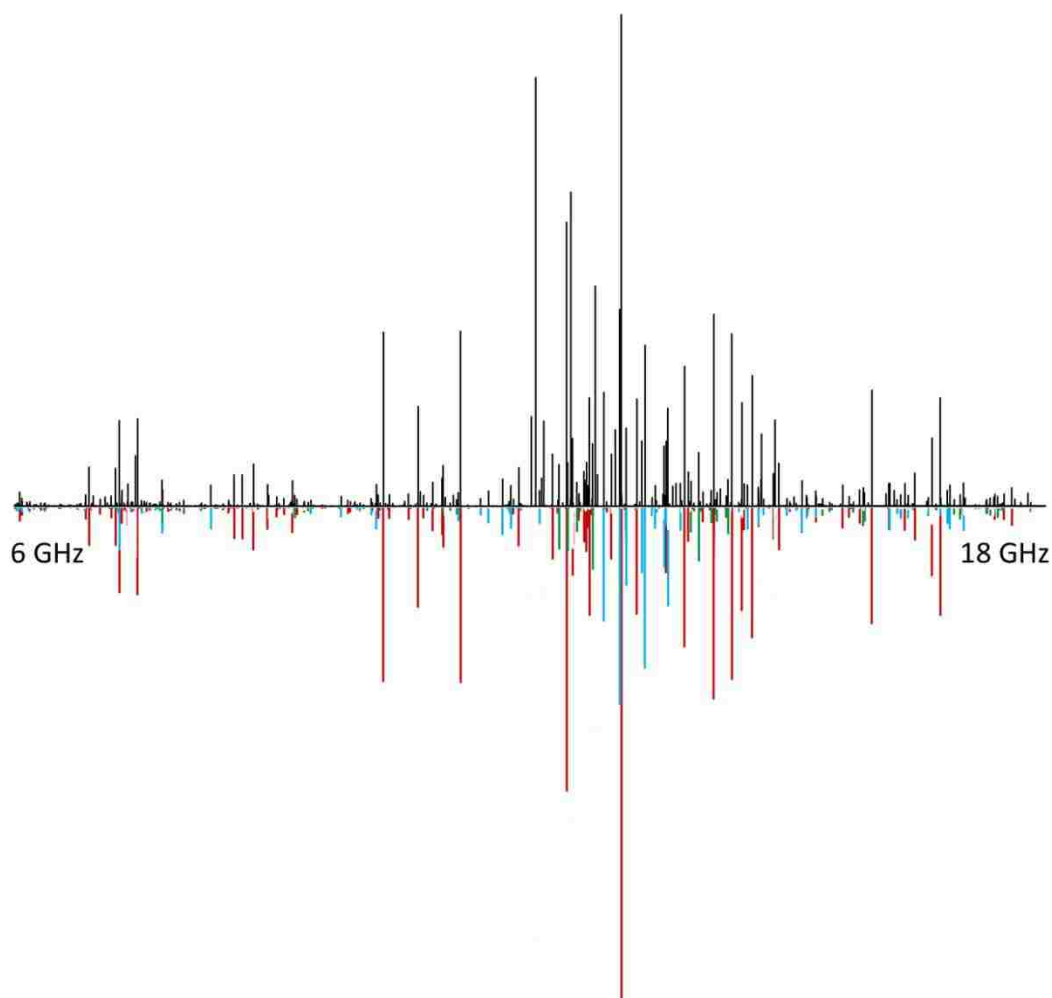
Figure 2. The myrtenol rotational spectrum from 6 – 18 GHz. The upper trace is the full experimental spectrum. The lower trace contains the lines assigned to Exp1(red), Exp2(blue), and Exp3(green).

observed to be dominant. The transition frequencies used in each fit were determined using Kisiel's Assignment and Analysis of Broadband Spectra (AABS) [217] program, with the uncertainty in the frequencies set to 10 kHz. All experimental fits were performed using a Watson S Hamiltonian [218] in the I^r representation in Pickett's SPFIT/SPCAT [219] program package. The final fit of each species was then run through

PIFORM to get the actual errors associated with each parameter. The values of the spectroscopic parameters, number of transitions, and root mean square residuals associated with each observed species can be found in Table 1.

In the case of Exp3, the D_K and d_2 centrifugal distortion constants were not included in the fit, effectively setting their values to zero. Inclusion of these two parameters did not improve the residual of the fit or change the other spectroscopic constants beyond their reported uncertainties. Their inclusion did, however, result in uncertainties in both D_K and d_2 that were of the same order of magnitude as the values themselves. This effectively makes the constants zero within the uncertainty of the fit values, and for this reason, the authors chose not to include the D_K and d_2 parameters in the final analysis of Exp3. It should, also, be noted that for all observed transitions the obs-calc frequencies were found to be within both 3σ (30 kHz) of the observed frequency and the full width at half maximum intensity of the transition. A complete list of the assignments, frequencies, and obs-calc values can be found in the supplementary material along with a copy of the Pickett input files (.par) for each species.

3. COMPUTATIONAL METHODS AND RESULTS

The structure of the myrtenol monomer has been optimized using both *ab initio* and Density Functional Theory (DFT) methods. The *ab initio* calculations were performed using the second order perturbation terms of Møller and Plesset [220, 221]. The DFT optimizations were completed using Becke 3-parameter exchange along with the correlation interactions of Lee, Yang, and Parr (B3LYP) [222, 223]. In both cases, the

Table 1. Spectroscopic parameters for the three experimentally observed conformers of myrtenol.

Conformer	Exp1	Exp2	Exp3
A [MHz]	1589.3106(1)[a]	1701.5644(2)	1887.5613(5)
B [MHz]	971.9226(1)	871.6497(1)	810.6285(1)
C [MHz]	827.7189(1)	802.1595(1)	760.7041(1)
D_J [kHz]	0.0903(8)	0.0456(6)	0.0282(8)
D_{JK} [kHz]	-0.1130(7)	-0.0050(6)	0.110(2)
D_K [kHz]	0.139(3)	0.244(3)	—
d_1 [kHz]	-0.02437(5)	-0.01016(5)	-0.0050(1)
d_2 [kHz]	0.00045(3)	0.00022(1)	—
S:N [unitless][b]	9800:1	4000:1	1300:1
N [unitless][c]	314	196	118

[a] Numbers in parentheses represent one standard error, a 67% confidence level

[b] S:N is the maximum observed signal to noise rounded to the nearest 100:1

[c] N is the number of transitions included in the fit

[d] σ_{rms} is the root mean square microwave residual

calculations were performed using the Dunning's correlation consistent n-tuple ζ basis set, cc-pVTZ [224]. Given the size of the molecule and the computational cost, the authors chose to forgo the use of the fully augmented basis set (aug-cc-pVTZ) while calculating the minima structures of myrtenol.

A second DFT method, B3LYP-D3BJ|def2-TZVP, was also employed in this study. Previous work on the structurally similar verbenone [203] monomer has shown this methodology to give an optimized structure in good agreement with that produced by rotational spectroscopy with isotopic substitution. In addition, the D3BJ correction uses Grimme's D3 dispersion with Becke-Johnson damping, which is known to give better

geometries and energies than the B3LYP functional alone [225, 226, 227]. Lastly, frequency calculations were performed on the DFT optimized structures to correct for zero-point energy and to determine the thermal free energies used to predict the Boltzmann distributions of the conformers shown in Table 2. Frequency calculations on the optimized structures using the MP2 methodology were initially attempted, but the computational costs in terms of processors and allotted time proved to be prohibitive. All calculations were performed using the Gaussian09® (G09) program package [228]. The Cartesian coordinates of the optimized structures determined for each conformer and method can be found in the supplementary materials.

As expected, all calculations exhibited a consistent structure associated with the bicyclic cage of the molecule. However, the inclusion of the primary alcohol group in myrtenol added a degree of conformational freedom not present in the unfunctionalized bicyclic system, namely the $\angle OC_\alpha C_\beta C_\gamma$ dihedral angle shown in Figure 3. B3LYP|cc-pVTZ calculations where performed over the range of this dihedral angle. The results of these calculations found three minima structures with dihedral angles of approximately ±120° and 0°, labelled Comp1 – Comp3 in Figure 4. Due to the lack of symmetry in the molecule, an asymmetric barrier to rotation between the conformers was predicted. The barrier heights for interconversion of the conformers have, also, been included in Figure 8.4. B3LYP-D3BJ|def2-TZVP and MP2|cc-pVTZ calculations determined similar minima structures with only slight variations in bond lengths and angles. The values of the dihedral angle and the rotational constants associated with each of the methods and conformers can be found in Table 2.
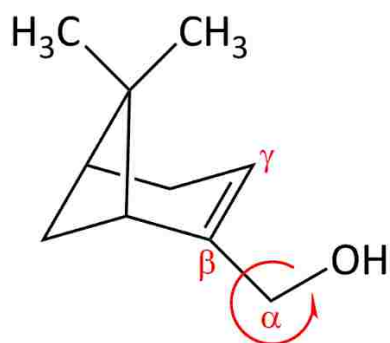
Figure 3. Myrtenol's generic structural formula highlighting the conformational degree of freedom associated with the $\angle OC_\alpha C_\beta C_\gamma$ dihedral angle.
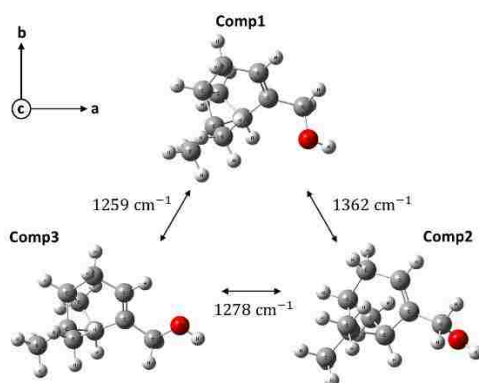
Figure 4. The three low energy conformers of myrtenol. The values in wavenumbers (cm^{-1}) represent the barriers, predicted using B3LYP|cc-pVTZ, for rotation between the conformers. The molecular axis system is shown in the upper corner.

4. DISCUSSION

A direct comparison of the rotational constants of the experimentally observed species can be made to those for the three alcohol conformers predicted by theory. Such an assessment shows differences of <1.1% for the DFT methods and <2.0% for the *ab initio* calculations, making it possible to unambiguously assign the experimentally

observed species to the conformers predicted by theory (Exp1 to Comp1, Exp2 to

Comp2, and

Table 2. Structural parameters and energies predicted for the myrtenol conformers.

Conformer	Comp 1	Comp 2	Comp 3	Comp 1	Comp 2	Comp 3	Comp 1	Comp 2	Comp 3
Dihedral[a]	121.5°	-123.1°	0.2°	120.0°	-122.7°	-0.1°	119.0°	-122.5°	0.3°
A [MHz]	1590	1694	1889	1595	1700	1893	1603	1711	1905
B [MHz]	969	876	812	978	881	818	992	889	824
C [MHz]	823	802	763	830	807	768	841	814	775
E [cm^{-1}]	0	42	23	0	47	87	0	103	152
E$_{zpc}$ [cm^{-1}][b]	0	58	26	0	50	58	-----	-----	-----
N$_i$/N$_1$ (298 K)[c]	1.00	0.71	0.76	1.00	0.77	0.76	-----	-----	-----
E [cm^{-1}]	0	42	23	0	47	87	0	103	152

[a] This angle is the dihedral formed from the carbon/carbon double bond and the carbon/oxygen bond.

[b] This change in energy has been corrected for zero-point energy

[c] This value is the Boltzmann distribution from the predicted thermal free energies, where i = 1, 2, or 3 depending on the conformer

Exp3 to Comp3). However, to verify the conformer assignments and determine which of

the theoretical methods shows the best agreement with the expected experimental

structures, an evaluation of the second moments of inertia (P_{xx}) is more appropriate. In

the case of myrtenol, rotation of the –OH group out of the $\sim 0°$ dihedral position expected for Exp1 shifts mass away from both the a- and b-axis, which is consistent with the increased values of P_{aa} and P_{bb} determined for Exp2 and Exp3. When comparing theoretical second moments to those of experiment, it was found that the second moments predicted by DFT were in slightly better agreement with experiment than those predicted by MP2. The unmodified B3LYP calculations had an average unsigned error of 0.6% when compared to the nine second moments of the three experimental species, while the D3BJ corrected B3LYP and MP2 calculations had average unsigned errors of 0.7% and 1.3%, respectively. The individual second moments of inertia and their percent errors [194] can be found in Table 3. It should be noted that the differences between experimental second moments and those of theory are less than the typically contribution associated with out-of-plane H atoms (3.1 amu·Å^2) in –CH$_3$– and –CH$_2$– groups, making it evident that any differences in the second moments are due to slight variations in the atom positions and not due to the observation of a secondary or unreported conformer.

In terms of the calculated energies of the conformers, the MP2|cc-pVTZ and B3LYP|cc-pVTZ calculations showed a discrepancy. Both methods agreed that the conformer labelled Comp1 was the global minimum structure. However, the progression of Comp2 and Comp3 was inverted between the methods, as can be seen by the ΔE values reported in Table 2. Although this discrepancy is notable, it is not altogether unexpected, as the *ab initio* calculations address dispersion and give true approximate energies while standard B3LYP does not. Inclusion of the empirical dispersion correction (D3BJ) does place the energetic progression predicted by B3LYP-D3BJ|def2-TZVP into qualitative agreement with that of the *ab initio* calculations, although the relative

progression of the DFT conformers is somewhat mitigated upon correcting for zero-point energy.

Assigning the energetic progression of the experimentally observed conformers is slightly more complicated. Although CP-FTMW is known to give good relative intensities over a limited frequency range, using the observed intensities to determine accurate populations of conformers requires a well determined value for the rotational temperature and a thorough knowledge of the transition dipole moments. While the operating temperature of the sample in the nozzle reservoir can be controlled with confidence, the rotational temperature of the pulsed beam is less accurately known, beyond the fact that it was sufficient for the observation of transitions up to $J = 26$. We may, however, reasonably assume that all three conformers were introduced with consistent rotational temperatures. Unfortunately, the experimental dipole moments for the three conformers are, as of yet, unknown, making any truly experimental determination of the populations impossible.

An argument can be made for using a hybrid approach where experimentally observed intensities and theoretically predicted dipole moments are used to determine the relative populations of the conformers. The reliability of such an approach would depend greatly on the accuracy of the predicted dipole moments. Although good agreement is achieved when comparing the experimental heavy atom structures to those of theory using second moments, a comparison of the experimental and theoretical electronic structure that would prove the accuracy of the theoretical dipole moments is less definitive. The lack of a nuclear quadrupole in myrtenol and the current inability of the cp-FTMW spectrometer to collect Stark shifted frequencies, make it impossible to probe

the electronic structure of myrtenol using anything other than the observed spectral

intensities. As was previously mentioned, the spectra of all three experimental species

Table 3. Experimental second moments of inertia and a comparison to those predicted by theory.

Conformer 1	Experimental	B3LYP[a]	B3LYP-D3BJ[b]	MP2[c]
P_{aa} [amu·Å^2]	406.28038(5)[d]	409 [0.7%]	404 [-0.4%]	398 [-2.1%]
P_{bb} [amu·Å^2]	204.28803(5)	205 [0.5%]	204 [0.1%]	203 [-0.4%]
P_{cc} [amu·Å^2]	113.69828(5)	113 [-1.0%]	112 [-1.2%]	112 [-1.7%]
Conformer 2				
P_{aa} [amu·Å^2]	456.40532(5)	454 [-0.5%]	451 [-1.1%]	447 [-2.1%]
P_{bb} [amu·Å^2]	173.61777(5)	176 [1.3%]	175 [0.7%]	174 [0.1%]
P_{cc} [amu·Å^2]	123.39068(5)	122 [-0.7%]	122 [-0.9%]	122 [-1.5%]
Conformer 3				
P_{aa} [amu·Å^2]	510.02804(7)	509 [-0.3%]	504 [-1.1%]	500 [-2.0%]
P_{bb} [amu·Å^2]	154.32885(7)	154 [-0.3%]	154 [-0.3%]	152 [-1.3%]
P_{cc} [amu·Å^2]	113.41292(7)	114 [0.1%]	113 [-0.2%]	113 [-0.4%]

[a] Values [Percent Error from experiment] for B3LYP|cc-Pvtz

[b] Values [Percent Error from experiment] for B3LYP-D3BJ|def2-TZVP

[c] Values [Percent Error from experiment] for MP2|cc-pVTZ

[d] Numbers in parentheses represent one standard error, a 67% confidence level

were dominated by strong a-type transitions and c-type transitions were not observed for Exp2. The dipole moments predicted by theory, shown in Table 4, do not reliably agree with these observations. These discrepancies led the authors to question the use of a hybrid approach in the current case, and as such, no quantitative experimental or semi-empirical relative populations have been presented for the three observed conformers.

Table 4. Theoretical component dipole moments.

dipole	B3LYP|cc-pVTZ			B3LYP-D3BJ|def2-TZVP			MP2|cc-pVTZ		
	Comp 1	Comp 2	Comp 3	Comp 1	Comp 2	Comp 3	Comp 1	Comp 2	Comp 3
μ_a	0.83	0.24	0.15	0.82	0.20	0.12	0.89	0.28	0.15
μ_b	0.59	0.23	1.24	0.58	0.26	1.29	0.57	0.22	1.25
μ_c	0.84	1.25	0.75	0.87	1.30	0.76	0.78	1.28	0.75

That does not mean a general trend in the relative populations can't be inferred from the experimental evidence. As seen from the signal to noise values reported in Table 1 and the spectra of Figure 2, Exp1 was observed to have a maximum signal to noise 2.5 times greater than that of Exp2 and 7.5 times larger than that of Exp3. This, taken with the number and types of transitions observed for the three species, strongly suggests that the molecular beam favored a population distribution where Exp1 > Exp2 > Exp3. This inferred progression agrees with those predicted by the B3LYP-D3BJ\|def2-TZVP and MP2\|cc-pVTZ calculations

5. CONCLUSION

The rotational spectrum of (1R)-(–)-myrtenol has been observed from 6–18 GHz. Three conformers of the monomer have been observed experimentally. The experimental second moments strongly suggest that the three observed conformers are associated with unique positions of the hydroxyl group with respect to the carbon/carbon double bond of the bicyclic cage. When comparing the optimized geometries predicted by theory to the experimental second moments of inertia, it was found that B3LYP methods slightly outperformed those of comparable MP2 calculations. However, the energetic progression of the conformers was found to be better described by MP2 when compared to unmodified B3LYP energies. Inclusion of the D3BJ dispersion correction to the B3LYP calculations put the energetic progression into qualitative agreement with the MP2 calculations, while maintaining the slightly superior structural optimization.

ACKNOWLEDGEMENTS AND FUNDING

REFERENCES

1. Bloemen H.J.T., Burns J. (Eds.) (1993) Chemistry and Analysis of Volatile Organic Compounds in the Environment. Springer, Dordrecht

2. P. Khare, D.R. Gentner, *Atmos. Chem. Phys.* **18** (2018) 5391.

3. J. Kesselmeier, M. Staudt, *J. Atmos. Chem.* **33** (1999) 23.

4. G.G. Habermehl, W. Fliegner, *Stud. Nat. Prod. Chem.* **20** (1997) 3

5. G. Vivaldo, E. Masi, C. Taiti, G. Caldarelli, S. Mancuso, *Sci. Rep.* **7** (2017) 11050

6. V.S. Parmar, A. Jha, *Stud. Nat. Prod. Chem.* **20** (1997) 79

7. V. Varlet, M. Augsburger, *Drug Test Anal.* **5** (2013) 474

8. M. Hallquist, J.C. Wenger, U. Baltensperger, Y. Rudich, D. Simpson, M. Claeys, J. Dommen, N.M. Donahue, C. George, A.H. Goldstein, J.F. Hamilton, H. Herrmann, T. Hoffmann, Y. Iinuma, M. Jang, M.E. Jenkins, J.L. Jimenez, A. Kiendler-Scharr, W. Maenhaut, G. McFiggans, T.F. Mentel, A. Monod, A.S.H. Prevot, J.H. Seinfeld, J.D. Surratt, R. Szmigielski, J. Wildt, *Atmos. Chem. Phys.* **9** (2009) 5155

9. R. Atkinson, S.M. Aschmann, J. Arey, B. Shorees, *J. Geophys. Res.* **97** (1992) 6065

10. F.E. Marshall, G. Sedo, C. West, B.H. Pate, S.M. Allpress, C.J. Evans, P.D. Godfrey, D. McNaughton, G.S. Grubbs II, *J. Mol. Spectrosc.* **342** (2017) 109.

11. E.M. Neeman, J.R.A. Moreno, T.R. Huet, *J. Chem. Phys.* **147** (2017) 214305

12. M. Chrayteh, P. Drean, T. Huet, *J. Mol. Spectrosc.* **336** (2017) 22

13. E.M. Neeman, P. Drean, T.R. Huet, *J. Mol. Spectrosc.* **322** (2016) 50

14. D. Loru, M.A. Bermudez, M.E. Sanz, *J. Chem. Phys.* **145** (2016) 074311

15. Z. Kisiel, O. Desyatnyk, E. Bialkowska-Jaworska, L. Pszczolkowski, *Phys. Chem. Chem. Phys.* **5** (2003) 820.

16. Z. Kisiel, A.C. Legon, *J. Am. Chem. Soc.* **100** (1978) 8166

17. J.F. Chiang, R. Chiang, K.C. Lu, E.M. Sung, M.D. Harmony, *J. Mol. Struct.* **41** (1977) 67

18. K.J. Mayer, L. Evangelisti, M.S. Holdren, T. Smart, C. West, B. Pate, G. Sedo, F.E. Marshall, G.S. Grubbs II, "Chiral Tagging of Verbenone with 3-Butyn-2-ol for Establishing Absolute Configuration and Determining Enantiomeric Excess" 72nd International Symposium on Molecular Spectroscopy, June 21st 2017, Champaign-Urbana, Illinois

19. D. Patterson, M. Schnell, J.M. Doyle, *Nature* **497** (2013) 475

20. N.A. Seifert, C. Perez, J.L. Neill, B.H. Pate, M. Vallejo-Lopez, A. Lesarri, E.J. Cocinero, F. Castano, *Phys. Chem. Chem. Phys.* **17** (2015) 18282

21. F.E. Marshall, D.J. Gillcrist, T.D. Persinger, S. Jaeger, C.C. Hurley, N.E. Shreve, N. Moon, G.S. Grubbs II, *J. Mol. Spectrosc.* **328** (2016) 59

22. F.E. Marshall, R. Dorris, S.A. Peebles, R.A. Peebles, G.S. Grubbs II, "Microwave spectra and structure of Ar-1,3-difluorobenzene." *J. Phys. Chem. A* (2018) Manuscript Submitted

23. R.D. Suenram, G.Y. Golubiatnikov, I.I. Leonov, J.T. Hougen, J. Ortigoso, I. Kleiner, G.T. Fraser, *J. Mol. Spectrosc.* **208** (2001) 188

24. Z. Kisiel, L. Pszczolkowski, B. J. Drouin, C. S. Brauer, S. Yu, J. C. Pearson, I. R. Medvedev, S. Fortman, C. Neese, *J. Mol. Spectrosc.* **270** (2012) 134. The program is freely available through the Programs for ROtational SPEctroscopy (PROSPE) website; http://info.ifpan.edu.pl/~kisiel/prospe.htm

25. J.K.G. Watson, "Vibration Spectra and Structure" (Editor, J. Durig) Elsevier, Amsterdam, Vol. 6 (1977).

26. H. M. Pickett, J. Mol. Spectrosc. 148 (1991) 371.

27. C. Møller, M. S. Plesset, Phys. Rev. 46 (1934) 618

28. R. Krishnan, M. J. Frisch, J. A. Pople, J. Chem. Phys. 72 (1980) 4244.

29. A. D. Becke, J. Chem. Phys. 98 (1993) 5648.

30. P. J. Stephens, F. J. Devlin, C. F. Chabalowski, M. J. Frisch, J. Phys. Chem. 98 (1994) 11623.

31. T. H. Dunning, Jr., J. Chem. Phys. 90 (1989) 1007.

32. S. Grimme, J. Antony, S. Ehrilich, S. Krieg, J. Chem. Phys. 132 (2010) 154104.

33. S. Grimme, S. Ehrlich, L. Goerigk, J. Comput. Chem. 32 (2011) 1456.

34. S. Grimme, M. Steinmetz, Phys. Chem. Chem. Phys. 15 (2013) 16031.

35. Gaussian 09, Revision C.01 (UVa-Wise) and E.01 (MS&T), M. J. Frisch, G. W. Trucks, H. B. Schlegel, G. E. Scuseria, M. A. Robb, J. R. Cheeseman, G. Scalmani, V. Barone, B. Mennucci, G. A. Petersson, H. Nakatsuji, M. Caricato, X. Li, H. P. Hratchian, A. F. Izmaylov, J. Bloino, G. Zheng, J. L. Sonnenberg, M. Hada, M. Ehara, K. Toyota, R. Fukuda, J. Hasegawa, M. Ishida, T. Nakajima, Y. Honda, O. Kitao, H. Nakai, T. Vreven, J. A. Montgomery, Jr., J. E. Peralta, F. Ogliaro, M. Bearpark, J. J. Heyd, E. Brothers, K. N. Kudin, V. N. Staroverov, R. Kobayashi, J. Normand, K. Raghavachari, A. Rendell, J. C. Burant, S. S. Iyengar, J. Tomasi, M. Cossi, N. Rega, J. M. Millam, M. Klene, J. E. Knox, J. B. Cross, V. Bakken, C. Adamo, J. Jaramillo, R. Gomperts, R. E. Stratmann, O. Yazyev, A. J. Austin, R. Cammi, C. Pomelli, J. W. Ochterski, R. L. Martin, K. Morokuma, V. G. Zakrzewski, G. A. Voth, P. Salvador, J. J. Dannenberg, S. Dapprich, A. D. Daniels, Ö. Farkas, J. B. Foresman, J. V. Ortiz, J. Cioslowski, and D. J. Fox, Gaussian, Inc., Wallingford CT, 2009.G. B. Churchill, J. P. Dombrowski, L. Ma, K. Swana, R. K. Bohn, J. A. Montgomery Jr., J. Molec. Structure 978 (2010) 11-13.

SECTION

3. CONCLUSION

In conclusion, the Chirped-Pulse Fourier Transform Microwave spectrometer has successfully been utilized to detect high resolution, broadband spectra across a variety of molecules. This instrument has been shown to be sensitive to only a few hundred in a million molecules. It has demonstrated an ability to rapidly acquire strong spectra across non-volatile, normally weak in intensity molecules. It has successfully identified new isotopes of molecules that have not been identified before, it has observed very rare transitions that are weak in intensity by definition, and it is capable of easily observing weak complexes.

The works presented in this document demonstrate the versatility of the instrument and the available techniques as well. The low noise, high fidelity instrument at Missouri S&T has successfully minimized parts, cable lengths, etc. . . and demonstrated a high level of success through doing so. The development of the heated nozzle source, from the U-tube to the current stainless steel nozzle head, demonstrates an ability to accomplish a task through multiple avenues.

In the future, the instrument will only be enhanced by further developing and perfecting the laser ablation apparatus. This will only serve to enhance the instrument and open up new molecules for study.

New techniques for improving sensitivity, such as multiple horn detection or the cooling of the horn detectors, are due to be implemented. Improving the sensitivity of an

already sensitive instrument could lead to the detection of more isotopes, which can lead to higher accuracy in experimentally derived structures. Additionally this could allow for the determination of other more sensitive effects – such as the differentiation of chiral enantiomers through chiral tagging, which should be implemented by the Grubbs' lab in the next few years.

REFERENCES

1.   C. E. Cleeton and N. H. Williams, *Phys. Rev. 45,* 234 (1934)

2.   Bernath, P. (2006) *Spectra of Atoms and Molecules.* New York, New York: Oxford University Press

3.   C. H. Townes and A. L. Schawlow, Microwave Spectroscopy (Dover Publications, Inc., New York, 1975).

4.   W. Gordy and R. L. Cook, Microwave Molecular Spectra; Techniques of Chemistry Vol. XVIII (Wiley, New York, 1984).

5.   J. Kraitchman, Am. J. Phys. 21, 17 (1953).

6.   T. J. Balle and W. H. Flygare, Rev. Scient. Instrum. 52, 33 (1981)

7.   G. G. Brown, B. C. Dian, K. O. Douglass, S. M. Geyer, S. T. Shipman, and B. H. Pate, Rev. Scient. Instrum. 79, 053103 (2008)

8.   J. C. McGurk, T. G. Schmalz, and W. H. Flygare, J. Chem. Phys. 60, 4181 (1974)

9.   C.R. Nave. Hyperphysics, Georgia State University 2016. http://hyperphysics.phy-astr.gsu.edu/hbase/electric/dipole.html

10.   Nmr_fid_good_shim.svg: GyroMagicianderivative work: Imalipusram [CC BY-SA 3.0 (https://creativecommons.org/licenses/by-sa/3.0)]

11.   Cooley, James W.; Tukey, John W. (1965). "An algorithm for the machine calculation of complex Fourier series". Math. Comput. 19 (90): 297–301. doi:10.2307/2003354. JSTOR 2003354

12.   J. Ekkers and W. H. Flygare, Rev. Scient. Instrum. 47, 448 (1976)

13.   R.D. Suenram, G.Y. Golubiatnikov, I.I. Leonov, J.T. Hougen, J. Ortigoso, I. Kleiner, G.T. Fraser, *J. Mol. Spectrosc.* **208** (2001) 188

14.   K. A. Walker and M. C. L. Gerry, J. Mol. Spectrosc. 182, 178 (1997)

15.   By Zen-in at English Wikipedia, CC BY-SA 3.0, https://commons.wikimedia.org/w/index.php?curid=65454074

VITA

Frank Marshall obtained his undergraduate degrees in both Applied Mathematics and Physics from the Missouri University of Science and Technology in 2015. He received his PhD in Chemistry in December 2019 from Missouri University of Science and Technology.